Master's thesis

2017

Sondre Vik Furuseth

NTNU
Norwegian University of
Science and Technology
Faculty of Natural Sciences
Department of Physics

CERN-THESIS-2017-279
//2017

Sondre Vik Furuseth

Head-On Beam-Beam Interactions in High-Energy Hadron Colliders

GPU-Powered Modelling of Nonlinear Effects

August 2017

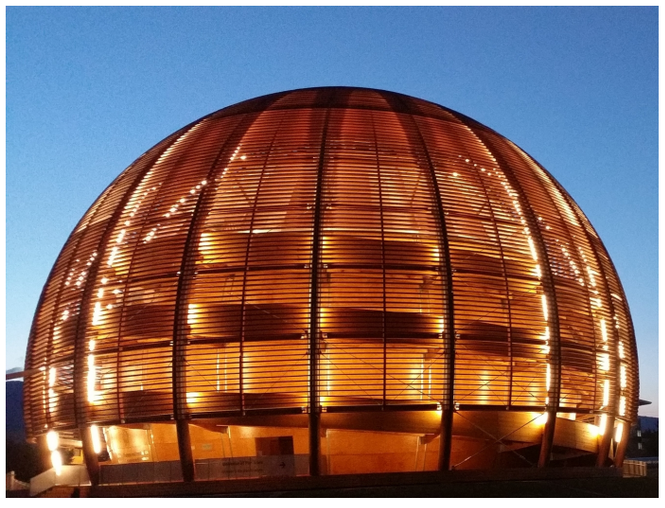

NTNU
Norwegian University of
Science and Technology

NTNU
Norwegian University of
Science and Technology

NTNU
Norwegian University of
Science and Technology

Head-On Beam-Beam Interactions in High-Energy Hadron Colliders

GPU-Powered Modelling of Nonlinear Effects

Sondre Vik Furuseth

Master of Science in Physics and Mathematics
Submission date: August 2017
Supervisor: Jon Andreas Støvneng, IFY
Co-supervisor: Xavier Buffat, CERN

Norwegian University of Science and Technology
Department of Physics

Preface

This Master's thesis is submitted for the degree of Sivilingeniør / Master of Science, at The Norwegian University of Science and Technology, for the Department of Physics. The thesis completes a five year integrated study in the field of Applied Physics and Mathematics, with Applied Physics as the main profile. The Master project was conducted under the supervision of Dr. Xavier Buffat at the European Organization for Nuclear Research, Accelerator and Beam Physics Group.

The thesis has in part aimed at modelling the beam-beam interaction using the weak-strong approach. All simulation results have been achieved using original code, unless explicitly stated otherwise. The thesis is an extension of my specialisation project report, of the same title, written in the autumn semester of 2016 [1]. Sections 2.1-2.3, 3.1-3.2 and 3.5, and Appendixes A and C.1 are based on the specialisation project. The main extensions are the implementation of flat beams and increasing from 4D to 6D phase space, including the longitudinal dimensions. The added dimensions enabled studies of the crossing angle, the hourglass effect and chromaticity, but it also required a study on efficient representation of 6D phase space with a given number of macroparticles.

"If I have seen further, it is by standing on the shoulders of giants."

—Isaac Newton

I want to thank:

- Dr. Xavier Buffat for helpful supervision throughout my work and for introducing me to the field of beam physics.
- Dr. Adrian Oeftiger at the European Organization for Nuclear Research, for valuable advices on the use of PyCUDA.
- Prof. Jon Andreas Støvneng at The Norwegian University of Science and Technology, for enabling and facilitating me in performing this work externally from the University.
- Anders Christensen and Einar Næss Jensen at The Norwegian University of Science and Technology, High-Performance Computing Group, for granting me access to the IDUN cluster and its GPU resources.
- Hanna Vik Furuseth and Andrea Høeg in my family, for helping me proofread parts of this thesis.
- Michael Hofer from my office at the European Organization for Nuclear Research, for help with equation design and always making me laugh when I am trying to work.
- Everyone who said mathematics, physics and programming is too hard, for motivating me in my endeavours.

"Tro på seg selv kan flytte fjell."

—Life motto

Summary

The performance of high-energy circular hadron colliders, as the Large Hadron Collider, is limited by beam-beam interactions. The strength of the beam-beam interactions will be higher after the upgrade to the High-Luminosity Large Hadron Collider, and also in the next generation of machines, as the Future Circular Hadron Collider. The strongly nonlinear force between the two opposing beams causes diverging Hamiltonians and drives resonances, which can lead to a reduction of the lifetime of the beams. The nonlinearity makes the effect of the force difficult to study analytically, even at first order. Numerical models are therefore needed to evaluate the overall effect of different configurations of the machines.

For this thesis, a new code named CABIN (Cuda-Accelerated Beam-beam INteraction) has been developed to study the limitations caused by the impact of strong beam-beam interactions. In particular, the evolution of the beam emittance and beam intensity has been monitored to study the impact quantitatively, while frequency map analysis has been performed to understand the impact qualitatively. The bunches in the beams have been modelled based on a three-dimensional Gaussian distribution. The bunches in the Large Hadron Collider are well approximated by cylindrically symmetric Gaussian bunches, which allows for certain consequences to be derived analytically. The mapping of both round and flat beams have been implemented with the weak-strong model, considering one beam to stay fixed throughout the simulation, while the other beam is changing. The simulations have been run on graphic cards, well adapted for studying this highly parallelisable problem, to reduce the computation time.

The beam-beam driven resonances have been shown both analytically and numerically to be stronger at lower order and further from the design orbit of the beam. Stronger beam-beam interactions cause a wider spread of the betatron frequencies/tunes within a single bunch, making it increasingly difficult to avoid resonances that cause detrimental effects on the beam quality. This has been seen in both simulations and experiments. In such scenarios, the common working point in the Large Hadron Collider, $(Q_x, Q_y) = (0.31, 0.32)$, is found to be suboptimal. Two alternative working points, $(0.315, 0.325)$ and $(0.475, 0.485)$, have been found to give better performance. Without long-range interactions, the beam quality is best preserved for zero crossing angle. Increasing the crossing angle activates odd resonances that can reduce the performance further, but it also reduces the tune spread within the bunch, making the bunch exposed to fewer strong resonances. Mixing between the longitudinal and transverse planes, caused by either a crossing angle, the hourglass effect or chromaticity, drives synchro-betatron resonances that also reduce the performance. However, a nonzero chromaticity is usually necessary to avoid coherent instabilities. A significant hourglass effect, $\sigma_s/\beta_q^* = 2/3$, has been found to reduce the detrimental effects caused by the chromaticity, and vice versa. A scheme designed to cancel beam-beam driven resonances, by applying a specific intermediate phase advance, has been found to have an extremely positive impact on the beam quality for zero crossing angle, but only a marginal impact for a nonzero crossing angle.

A dedicated experiment with strong head-on beam-beam interactions has been performed in the Large Hadron Collider. Simulations run in CABIN for the same configurations show good quantitative agreement. A realistic maximum beam-beam tune shift from the LHC working point has been found to be $\Delta Q_{\mathrm{Tot}} = 0.043$ with zero crossing angle. With a Piwinski angle of $\phi_{\mathrm{PIW}} = 1$, this limit is reduced to $\Delta Q_{\mathrm{Tot}} = 0.028$, smaller than the largest beam-beam tune shift expected in the Future Circular Hadron Collider. These limits are slightly larger for the alternative working point, $(0.315, 0.325)$, raised to $\Delta Q_{\mathrm{Tot}} = 0.067$ and 0.036 for zero and nonzero crossing angle respectively.

Sammendrag

Ytelsesevnen til en høy-energisk sirkulær akselerator, som Large Hadron Collider (LHC), er begrenset av de to strålenes påvirkning på hverandre. Styrken til påvirkningen kommer trolig til å øke ved oppgraderingen til høy-luminositets versjonen av LHC, og også i neste generasjon av maskiner, som Future Circular Hadron Collider. Den særdeles ikkelineære kraften mellom de to motgående strålene forårsaker divergerende Hamilton-funksjoner og driver resonanser, som kan lede til en reduksjon av levetiden til strålene.

I forbindelse med denne masteroppgaven har en ny kode blitt utviklet for å studere begrensningene forårsaket av strålenes påvirkning på hverandre. Strålens emittans og intensitet har blitt overvåket for å studere effekten kvantitativt, mens frekvensanalyse har blitt utført for å forstå effekten kvalitativt. Partiklene i strålen har blitt modellert til å være samlet i tredimensjonale Gaussiske bunter. Buntene i LHC er godt tilnærmet av sylindersymmetriske Gaussiske bunter, noe som gjør det mulig å utlede visse konsekvenser analytisk. Påvirkningen fra både sylindersymmetriske og elliptiske bunter har blitt implementert med svak-sterk modellen, som antar at den ene strålen ikke endrer seg mens den påvirker den andre strålen. Simuleringene kjører på grafikkort for å redusere simuleringstiden, fordi dette er et svært paralleliserbart problem.

Resonanser kan være skadelige for strålens kvalitet. Det har blitt vist både analytisk og numerisk at betatronresonanser drevet av strålenes påvirkning på hverandre, har større negativ effekt hvis resonansene er av lavere orden, og påvirker partikler lenger fra sentrum av strålen. Sterkere påvirkning forårsaker en større spredning av betatronfrekvensene innad i bunten, som igjen gjør det vanskeligere å unngå resonansfrekvenser forårsaket av påvirkningen. Dette har blitt sett både i simuleringer og i dedikerte eksperimenter. I scenarier med sterkere påvirkning mellom strålene, er dagens arbeidspunkt i LHC, $(Q_x, Q_y) = (0.31, 0.32)$, suboptimalt. I stedet har det blitt oppdaget bedre ytelsesevne ved to alternative arbeidspunkt, $(0.315, 0.325)$ og $(0.475, 0.485)$. Uten påvirkning av nabobunter i strålen, er strålen best bevart med null krysningsvinkel. Ved å øke krysningsvinkelen aktiveres odde resonansfrekvenser som kan redusere ytelsesevnen ytterligere, men den økte vinkelen reduserer også spredningen av betatronfrekvensene innad i bunten, noe som kan ha en positiv effekt. Sammensatte bevegelser i de longitudinale og transversale planene, enten grunnet en krysningsvinkel, timeglasseffekt eller kromatisitet, aktiverer synkro-betatronresonanser som kan forverre strålekvaliteten ytterligere. Samtidig er det viktig å ha en viss kromatisitet for å unngå koherente ustabiliteter. Det har blitt vist at en betydelig timeglasseffekt, $\sigma_s/\beta_q^* = 2/3$, kan redusere skadelige effekter forårsaket av sterk kromatisitet, og at en betydelig kromatisitet kan redusere skadelige effekter forårsaket av en sterk timeglasseffekt. En konfigurasjon tiltenkt å undertrykke resonanser drevet av strålenes påvirkning på hverandre, har blitt vist at har en ekstremt positiv effekt på strålekvaliteten når krysningsvinkelen er null. Effekten er eksisterende men lite betydelig dersom krysningsvinkelen ikke er null.

Et dedikert eksperiment med sterke påvirkninger mellom strålene har blitt utført i LHC. Simuleringer gjort med den nye koden for de samme konfigurasjonene har vist god kvantitativ overensstemmelse. En realistisk øvre grense på frekvensspredningen forårsaket av strålenes påvirkning på hverandre, fra det arbeidspunktet som benyttes i LHC, har blitt funnet å være $\Delta Q_{\mathrm{Tot}} = 0.043$ med null krysningsvinkel. Med en krysningsvinkel tilsvarende en Piwinski-vinkel på $\phi_{\mathrm{PIW}} = 1$, har denne grensen blitt redusert til $\Delta Q_{\mathrm{Tot}} = 0.028$. Denne grensen er mindre enn den største frekvensspredningen forventet i framtidige akseleratorer. Disse grensene er litt større ved det alternative arbeidspunktet $(0.315, 0.325)$, hevet til $\Delta Q_{\mathrm{Tot}} = 0.067$ og 0.036 respektivt.

Abbreviations

CERN	=	The European Organization for Nuclear Research
LHC	=	Large Hadron Collider
HL-LHC	=	High-Luminosity Large Hadron Collider
FCC	=	Future Circular Collider
CABIN	=	Cuda Accelerated Beam-Beam Interaction
hh	=	hadron-hadron
pp	=	proton-proton
e^+e^-	=	positron-electron
rms	=	root mean square
dof	=	Degrees of freedom
RF	=	Radio frequency
HO	=	Head-on
LR	=	Long-range
IP	=	Interaction point
IR	=	Interaction region
SBM	=	Synchro-beam mapping
CP	=	Collision point
2D	=	Two dimensional
3D	=	Three dimensional
ND	=	N dimensional
IC	=	Initial conditions
CPU	=	Central processing unit
GPU	=	Graphical processing unit
DA	=	Dynamic aperture
$NADA$	=	Noise affected dynamic aperture
HV	=	Horizontal crossing in one IP, vertical crossing in the other

Notation

The notation as it is applied in this thesis is presented here. Note especially the ambiguity of parentheses and the subscripts q and i.

$\{a, b\}$	The set of the listed values. In example: a and b.
$[a, b]$	Closed interval from a to b, i.e. including the endpoints.
(a, b)	Open interval from a to b, i.e. excluding the endpoints.
$(a, b) = (1, 2)$	Ordered pair or vector. In example: $a = 1$ and $b = 2$.
$f(a, b)$	Function of a and b.
$\langle a \rangle_x$	Average of a with respect to x.
$\exp[a]$	Exponential function. Square brackets used for specific functions.
$[x]$	Unit of enclosed value. In example: $[x] = \mathrm{m}$.
$\dot{x}$	Derivative of dotted value with respect to time or turn number.
a_q	Value of a in direction q, $q = \{x, y\}$.
a_i	Value of a in direction i, $i = \{x, y, s\}$.
$\hat{\mathbf{x}}_i$	Unit vector in direction i, $i = \{x, y, s\}$.
$\hat{x}_i$	Normalised value of x_i with respect to the root mean square (rms) spread.
$\mathbb{N}$	All natural numbers. $1, 2, 3, 4, ...$
$\mathbb{Z}$	All integers. $..., -2, -1, 0, 1, 2, ...$

Coordinates as they are used in this thesis:

x_q	Transverse position.
$\bar{p}_q$	Transverse physical momentum.
x'_q	Transverse canonical momentum, angle of motion with the design orbit.
p_q	Normalised transverse canonical momentum.
J_q	Transverse action.
ϕ_q	Angle in transverse phase space.
A_q	Amplitude in transverse phase space.
z	Longitudinal position along the circular collider.
s	Longitudinal position relative to design orbit.
δ	Energy deviation relative to design energy.
σ_Σ	Transverse beam size of the strong beam in the simulations.
σ_ϵ	Transverse beam size corresponding to the operational beam emittance.

CONTENTS

Chapter 1

INTRODUCTION

The European Organization for Nuclear Research (CERN) has built a large accelerator complex [2], designed to accelerate massive particles towards the speed of light. The goal is to make the particles collide within specialised particle detectors to study high-energy physics. The most powerful accelerator as of today is the Large Hadron Collider (LHC), which currently collides protons at a centre-of-mass energy of 13 TeV. The LHC consists of two synchrotrons, containing and accelerating particles in opposite directions, schematically displayed in Fig. 1.1. It is designed with 8 straight sections. In 4 of these sections, the beam is accelerated, diagnosed, cleaned and extracted. The other 4 host experiments that analyse hard collisions between the particles in the opposing beams. The beams are more tightly focused at the experiments in interaction point (IP) 1 and IP5 than in IP2 and IP8, in order to maximise the rate of collisions between the particles in the two beams. More information can be found in the LHC design report [3].

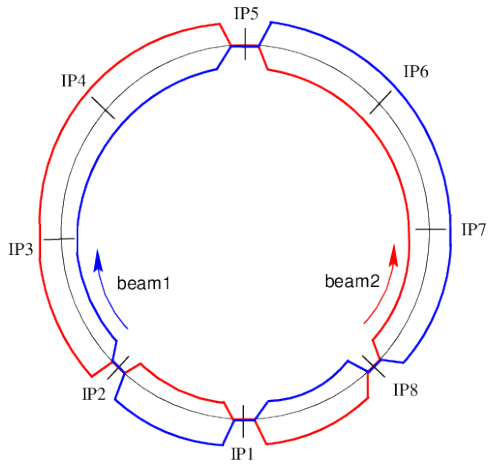

Figure 1.1: Schematic layout of the LHC interaction points and beams. Courtesy of [4].

Concurrently with the hard collisions at the IP, multiple small angle deflections occur. This phenomenon, known as the beam-beam interaction, is caused by the electromagnetic fields from the opposing hadron beam. The interaction force is strongly nonlinear, resulting in a number of consequences for the beam dynamics. The beam-beam interactions have been one of the most

important limits on the performance of circular colliders, and it will possibly become even more important with the envisaged upgrades in the future, including the high-luminosity upgrade of the LHC (HL-LHC) and the larger Future Circular Hadron Collider (FCC-hh) [5]. More densely packed beams are needed to produce the high luminosity required to study rare particle physics processes, resulting in stronger beam-beam forces.

The incoherent particles in the beams perform betatron oscillations as they circulate in the collider. Forces like the beam-beam interaction in the IPs, deflect the particles when they are at specific locations. The deflections are small, but can be accumulated over multiple turns for particles with betatron frequency equal to certain resonance frequencies. These betatron resonances can cause a strong diffusion of the particles, or even make the beam unstable and lost within a short amount of time. The beam-beam interaction drives resonances of multiple frequencies. It also widens the frequency spectrum of the particles in the bunch, making them vulnerable to more resonance frequencies. An earlier study found that destructive resonances driven by the beam-beam interaction, could be suppressed by making the particles perform a certain number of betatron oscillations between the IPs [6]. This method will be revisited in this thesis, testing the required accuracy to achieve the improved performance.

Although some effects of the beam-beam interaction can be derived analytically, numerical tools are necessary to assess the complete impact of the beam-beam interaction on the motion of incoherent particles, in particular their long-term behaviour. The use of simulations has been an important tool in the understanding of the effects that cause instabilities. The strong-strong approach calculates the beam-beam forces self-consistently, and is the most realistic representation of beam-beam interactions [7, 8]. However, the method does require a large amount of computational resources, limiting its practical applicability. There are several implementations of the method, that use different assumptions to make it more efficient. Despite the efforts, the self-consistent approach remains challenging for large scale studies with today's computing resources.

The weak-strong approach assumes that the bunch generating the electromagnetic fields stays rigid [9, 10]. This approach allows to study the nonlinear effects of the beam-beam interaction more efficiently, under the assumption that the charge distribution does not vary significantly when perturbed by the beam-beam interactions. In previous studies, the weak-strong approach has been applied to study single-particle stability, and the impact of the strength of the beam-beam interaction. While already advanced, these studies have not been able to present the full picture. The design of new machines and optimisation of existing ones, requires a detailed knowledge of all mechanisms involved in the deterioration of the beam quality in the presence of strong beam-beam interactions.

This master project will study the beam-beam interaction, based on the weak-strong approach. The goal has been to develop numerical tools that will help us understand the limitations that the head-on beam-beam interaction puts on the design of the next generation of high-energy circular hadron colliders. To achieve this, a main objective has been to quantitatively monitor the long-term evolution of the beam size and beam intensity. These are values of great importance to the performance, and they can be measured in running colliders. A code named CABIN has been developed for this purpose. This thesis will describe the parametric dependence of detrimental mechanisms on several relevant machine and beam parameters. In particular, it will be attempted to set a realistic criterion on the maximum spread of frequencies due to the beam-beam interaction. Using advanced diagnostic tools, also the underlying mechanisms will be explained. The results obtained can be used to provide specifications for an optimal performance of the collider.

Theoretical aspects of circular colliders are detailed in Ch. 2, including a derivation of the beam-beam interaction. How the physics is implemented and analysed is explained in Ch. 3. The results are presented in Ch. 4, along with a discussion of said results. The results will be compared to previous studies and to data from the LHC. The thesis is concluded in Ch. 5.

Chapter 2

THEORY

2.1 Introduction to Circular Particle Colliders

In this section a few important concepts of beam dynamics in circular particle colliders will be explained. Further details and derivations may be found in a text book on beam dynamics [11].

2.1.1 Geometry of a synchrotron

Synchrotrons are modern circular accelerators, appropriate for containing charged particles at high energies. In synchrotrons, particle beams travel in vacuum chambers of varying radius in a loop consisting of alternating straight and curved sections. In the limit of zero length straight sections, it takes the shape of the torus in Fig. 2.1. The average loop radius can be in the order of km, while the minimum radius of the beam can be in the order of $\mu\mathrm{m}$. The machines are designed so that a particle can follow a design orbit approximately in the centre of the vacuum chamber. The longitudinal position along the accelerator ring is z. The transverse plane can either be given as a 2D Cartesian or polar coordinate system, both are relevant in this thesis. The centre of the transverse plane is the design orbit. The x and y directions are also called horizontal and vertical respectively.

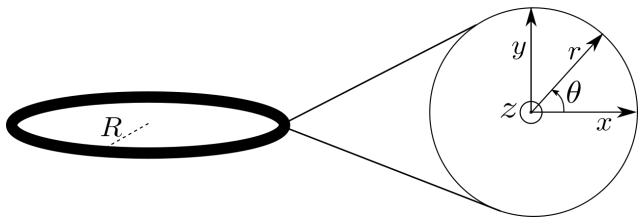

Figure 2.1: Geometry of a large circular collider, in the limit of zero length straight sections and constant beam pipe radius. The transverse plane has its origo in the design orbit, at a radius R from the centre of the collider. Not to scale.

The beta function, $\beta_q(z)$, is an optical function and may differ between the two transverse directions [11]. It characterises the magnetic lattice, not the dynamics of a specific particle. The lattice is the set of magnets and other elements that guide and focus the beam of particles. The rms size of the beam is proportional to the square root of the beta function, $\sigma_q(z) \propto \sqrt{\beta_q(z)}$. The beam size is smallest at the IPs, to increase the possibility of particle collisions (events). To achieve this,

the beta function has a local minimum at the IPs. It is usually signified by an asterisk as β_q^*. Close to any IP, located at z_{IP}, the beta function is approximately a parabola

$$\beta_q(z - z_{\mathrm{IP}}) = \beta_q^* \cdot \left(1 + \left(\frac{z - z_{\mathrm{IP}}}{\beta_q^*}\right)^2\right) \quad , \quad z - z_{\mathrm{IP}} \approx 0 \; . \tag{2.1}$$

Because of the parabolic dependence, this is referred to as the hourglass effect. There are two more optical functions related to the beta function; the alpha and gamma functions. They are given by

$$\alpha_q = -\frac{1}{2}\frac{\mathrm{d}\beta_q}{\mathrm{d}z} \qquad \text{and} \qquad \gamma_q = \frac{1 + \alpha_q^2}{\beta_q} \; . \tag{2.2}$$

These three optical functions are together called the Twiss parameters, with units $[\beta] = \mathrm{m}$, $[\alpha] = \mathrm{rad}$ and $[\gamma] = \mathrm{m}^{-1}$.

A particle in the beam has 6 dynamical degrees of freedom (dof), 3 positional and 3 translational. The position of a particle can be described by (x, y, s), where $s = z - z_0$ and z_0 is the design position of the particle, increasing linearly with time. This set of positional coordinates is a Cartesian coordinate system oriented around the design particle, with the s-axis parallel to the direction of the design particle. The translational dof are described by the momenta. Since both transverse momenta are small compared to the longitudinal momentum, it is convenient and conventional to use the paraxial approximation. The canonical momenta are

$$x' = \frac{\bar{p}_x}{\bar{p}_0} \quad , \quad y' = \frac{\bar{p}_y}{\bar{p}_0} \quad , \quad \delta = \frac{\bar{p}_z - \bar{p}_0}{\bar{p}_0} \; , \tag{2.3}$$

where the bar signifies mechanical momenta and $\bar{p}_0$ is the absolute value of the momentum of the design particle. x' is in the paraxial approximation the angle that a particle's horizontal motion makes with the s-axis. These coordinates are referred to as the accelerator coordinates. This thesis will focus on all 6 dynamical dof.

Each transverse phase space plane (x_q, x_q') can also be described in canonical action-angle coordinates (ϕ_q, J_q) [11]. There is one action and one angle per plane per particle, with equivalent definitions. The generating function for either transverse plane is

$$F_1(q, \phi_q) = -\frac{x_q^2}{2\beta_q}\left(\tan(\phi_q) + \alpha_q\right) \; . \tag{2.4}$$

The action and angle are then given by the Twiss parameters and the accelerator coordinates

$$J_q = \frac{1}{2}\left(\gamma_q x_q^2 + 2\alpha_q x_q x_q' + \beta_q x_q'^2\right) \; , \tag{2.5}$$

$$\tan(\phi_q) = -\alpha_q - \beta_q \frac{x_q'}{x_q} \; . \tag{2.6}$$

Likewise, the accelerator coordinates can be expressed as functions of the action-angle coordinates

$$x_q = \sqrt{2\beta_q J_q}\cos(\phi_q) \; , \tag{2.7}$$

$$x_q' = -\sqrt{\frac{2J_q}{\beta_q}}\left(\sin(\phi_q) + \alpha_q \cos(\phi_q)\right) \; . \tag{2.8}$$

A quantity called the beam emittance, ϵ_q, is related to the action of single particles through the relation

$$\epsilon_q = 2 \cdot \langle J_q \rangle \; , \tag{2.9}$$

where the angle brackets signify the average over all particles. A quantity that is more commonly referred to is the normalised emittance

$$\epsilon_{n,q} = \gamma \frac{v}{c} \epsilon_q \,, \tag{2.10}$$

where γ is the relativistic Lorentz factor. The normalised emittance is independent of the energy [12]. The size of the beam is proportional to the square root of the beam emittance, giving the complete relation

$$\sigma_q = \sqrt{\beta_q \epsilon_q} \,. \tag{2.11}$$

The beam can vary in size along the accelerator as β changes. However, if the beam emittance stays constant, the beam size at a given z will also be constant. The spread in transverse momentum, called the beam divergence, is defined similarly as

$$\sigma_{q'} = \sqrt{\frac{\epsilon_q}{\beta_q}} \,. \tag{2.12}$$

From these two expressions, it is clearly visible that as the beam is focused by reducing β_q at the IPs, the beam divergence increases, keeping the product of the two as constant as the emittance.

2.1.2 Lattice

The lattice that confines the particles inside the accelerator, usually consists of at least dipole and quadrupole magnets. Dipole magnets are needed to turn the beam around in a closed orbit, and quadrupole magnets are needed to focus the beam. Ideally, these are both linear elements, the magnetic fields are at most linear in the transverse coordinates (x, y), as will be demonstrated shortly. There is for stability reasons also need for higher order magnets in practice, but that is beyond the scope of this thesis. The field of an ideal dipole magnet is given by

$$\mathbf{B}_{\text{Dipole}} = B_D \hat{\mathbf{y}} \,, \tag{2.13}$$

where B_D is positive for particles that are going clockwise and negative for particles going counter-clockwise, seen from above. The field of an ideal normal quadrupole magnet is given by

$$\mathbf{B}_{\text{Quadrupole}} = B_0 \frac{y}{r_0} \hat{\mathbf{x}} + B_0 \frac{x}{r_0} \hat{\mathbf{y}} \,, \tag{2.14}$$

where B_0 is a reference magnetic field strength at the reference radius r_0 [11]. This is visualised in Fig. 2.2. There is also need for a quadrupole with fields rotated $\pi/2$ radians. One quadrupole can only focus the beam in either the x- or the y-direction, not both. Quadrupole magnets are therefore grouped together in groups of three, which enables focusing in both transverse directions.

The effects of dipole and quadrupole magnets can be written on matrix form. All elements that particles pass as they traverse the ring once, can be concatenated to produce a linear transfer map, referred to as the one-turn-map. There is ideally no mixing between the horizontal, vertical and longitudinal planes. The one-turn-map describing the evolution in either transverse plane can thus be given as $\mathbf{R}_q$ in

$$\begin{pmatrix} x_q \\ x'_q \end{pmatrix}_{T+1} = \mathbf{R}_q(\mu_q) \begin{pmatrix} x_q \\ x'_q \end{pmatrix}_T \,, \tag{2.15}$$

where T is the turn number and

$$\mathbf{R}_q(\mu_q) = \begin{pmatrix} \cos(\mu_q) + \alpha_q \sin(\mu_q) & \beta_q \sin(\mu_q) \\ -\gamma_q \sin(\mu_q) & \cos(\mu_q) - \alpha_q \sin(\mu_q) \end{pmatrix} , \tag{2.16}$$

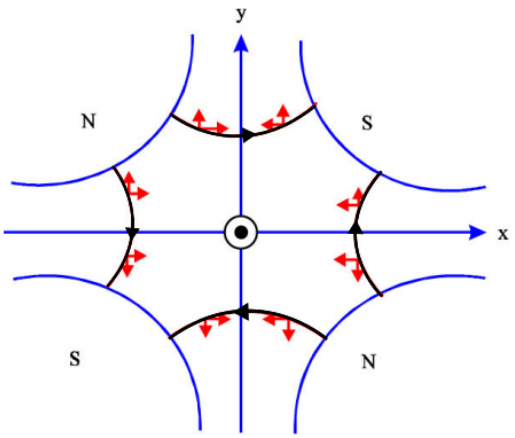

Figure 2.2: Magnetic field in normal quadrupole, as given by Eq. (2.14). The field lines are black. The red arrows point in the direction of the force on a particle of positive charge coming out of the paper. The length of the force arrows is not related to the magnitude of the force. Courtesy of [13].

where μ_q is the phase advance in the transverse plane caused by the lattice. In action-angle coordinates, this corresponds to an addition of μ_q to the angle ϕ_q. These oscillations in phase space are called betatron oscillations.

The particles perform betatron oscillations around the design orbit with separate oscillation frequencies in the two transverse phase space planes. With no other effect included, the number of oscillations per turn around the collider are the machine tunes, Q_q, defined as the fractional tunes in this thesis

$$Q_q = \frac{\mu_q}{2\pi} \in [0, 1) \, . \tag{2.17}$$

The integer part of the tune does not impact the dynamic at a given z, as it appears only in trigonometric functions in the one-turn-map. Therefore, it does not play a role in the dynamic when considering localised effects, such as those of beam-beam interactions. The combined choice of horizontal and vertical tune in a collider, (Q_x, Q_y), is called the working point.

Assume for now that a particle is only affected by the linear transfer map in Eq. (2.15). If this particle was measured at the same spot in the lattice over multiple turns, it would trace out an ellipse in horizontal phase space as shown in Fig. 2.3. This is called a Poincaré section [14]. The shape of the ellipse depends on the Twiss parameters and the action. The area of the ellipse is $A = 2\pi J_x$. Liouville's theorem states that the area of phase space is conserved if external forces are conservative and differentiable [15]. It follows that J_x and therefore also the beam emittance, ϵ_x, and the beam size, $\sigma_x(z)$, are constants of this motion, for a given z. This is in agreement with the results cited above, as there is no change of energy during this simplified motion. The presence of emittance growth at a fixed energy is therefore an indication that other nonlinear effects are acting on the beam.

The particles are accelerated to higher energies in radio frequency (RF) cavities [16]. Beyond an energy threshold, the particles traverse longer paths per loop if they have higher energy, as they bend less in the fixed dipole fields. The particles will therefore gradually move backwards in the bunch, i.e. $\Delta s < 0$, if $\delta > 0$. Due to the sinusoidal RF voltage, each particle is given an energy kick $\Delta\delta$ based on its position. Particles in the front, $s > 0$, gain more energy than the particles in the back, $s < 0$. The two effects combined are able to confine the particles longitudinally in the bunch. If these changes are small per turn, they can be approximated by a continuous oscillating motion.

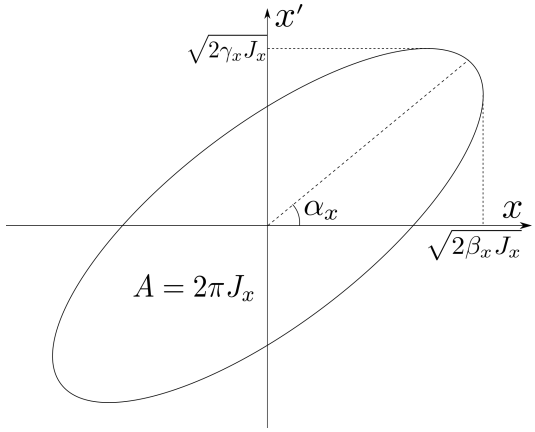

Figure 2.3: Ellipse traced out in horizontal phase space by a particle only affected by a linear lattice. The maximum x and x' depend on the Twiss parameters and the action of the particle.

These oscillations are called synchrotron oscillations. The one-turn-map for the longitudinal phase space plane, (s, δ), can for small longitudinal phase advances μ_s be given as

$$\begin{pmatrix} s \\ \delta \end{pmatrix}_{T+1} = \mathbf{R}_s \begin{pmatrix} s \\ \delta \end{pmatrix}_T \quad , \quad \mathbf{R}_s = \begin{pmatrix} \cos(\mu_s) & -\beta_s \sin(\mu_s) \\ \frac{1}{\beta_s} \sin(\mu_s) & \cos(\mu_s) \end{pmatrix} , \tag{2.18}$$

where μ_s is the longitudinal phase advance, and β_s is a convergence factor between the longitudinal displacement and energy deviation, $\beta_s = \sigma_s / \sigma_\delta$. The synchrotron tune can be defined similarly to the machine tunes as

$$Q_s = \frac{\mu_s}{2\pi} \in [0, 1) . \tag{2.19}$$

The synchrotron tune depends on the RF voltage, energy of the beam and radius of the accelerator. It is commonly quite small compared to the betatron tunes, $Q_s \approx 0.002$ in the LHC.

The focusing strength of the quadrupole magnets depends on the individual energy deviation of the particles. This effect is called chromaticity [17], as in regular light optics. The tunes, Q_q, are not constant but depend on δ as [18]

$$Q_q = Q_{q,0} + Q'_q \delta + Q''_q \frac{\delta^2}{2} , \tag{2.20}$$

where Q'_q and Q''_q are the chromaticity factors to first and second order. This thesis will only focus on chromaticity to first order. The presence of large chromaticity generates a large spread in betatron frequencies, potentially leading to beam losses. Coherent instabilities driven by electromagnetic wakefields can also deteriorate the beam quality for small chromaticities [19]. The optimal chromaticity for operation of a collider is the result of a good balance between these different effects. It is usually controlled with sextupole magnets.

The effect of chromaticity on the position of particles results in a periodic modulation of the betatron frequency. Consider only the effect of the betatron and synchrotron rotations

$$x_q(T) = A_q \cdot \cos(2\pi Q_q T + \phi_{q,0}) , \tag{2.21}$$

$$\delta(T) = A_\delta \cdot \sin(2\pi Q_s T + \phi_{s,0}) , \tag{2.22}$$

where A_i are the position amplitudes, $\phi_{i,0}$ are the phase constants, which for simplicity are set to 0 in the following, and T is the turn number. Including the effect of chromaticity, the evolution becomes

$$x_q(T) = A_q \cdot \cos\left(2\pi\left(Q_{q,0}T + Q'\sum_{T'=0.5}^{T-0.5}\delta(T')\right)\right) , \tag{2.23}$$

where $\delta(T)$ is given in Eq. (2.22), and is evaluated in the middle of each turn. Due to the slow variation, the summation may be exchanged for an integration over the interval $T' \in [0, T]$, giving an analytical expression for the position. The new turn dependent tune can then be calculated as the turn derivative of the phase to be

$$Q_q(T) \approx Q_{q,0} + Q' \cdot A_\delta \cdot \sin(2\pi Q_s(T)) , \tag{2.24}$$

which was already known to first order from Eq. (2.20). The new analytical term for the position can be used to study the frequency components of the motion of $x_q(T, Q_q(T))$. Expanding it to second order in $\Gamma = Q'\delta/Q_s$, gives the expression

$$\begin{aligned} x_q(T) \approx\ & \cos(2\pi Q_{q,0}T) \cdot \left(1 - 0.75 \cdot \Gamma^2\right) - \Gamma \cdot \sin(2\pi Q_{q,0}T) \\ & + \frac{\Gamma}{2} \cdot (\sin(2\pi(Q_{q,0} + Q_s)T) \quad + \sin(2\pi(Q_{q,0} - Q_s)T)) \\ & + \frac{\Gamma^2}{2} \cdot (\cos(2\pi(Q_{q,0} + Q_s)T) \ \ + \cos(2\pi(Q_{q,0} - Q_s)T)) \\ & - \frac{\Gamma^2}{8} \cdot (\cos(2\pi(Q_{q,0} + 2Q_s)T) + \cos(2\pi(Q_{q,0} - 2Q_s)T)) \ , \end{aligned} \tag{2.25}$$

which corresponds well to the actual expression for $\Gamma \ll 1$. This second order expression gives already reasonable agreement for $\Gamma = 0.5$. The knowledge to take from Eq. (2.25) is that in addition to the known betatron frequency, $Q_{q,0}$, the coupled motion with the longitudinal plane due to the chromaticity, produces synchro-betatron side-bands. The side-bands have frequencies $Q_q \pm n \cdot Q_s$ where n is an integer. To leading order, the coefficient of the n-th side-band is proportional to Γ^n, assuming $\Gamma \ll 1$. In the LHC, $\sigma_\delta \approx 1 \times 10^{-4}$ and $Q' \in [0, 15]$, making $\Gamma \in [0, 0.75]$. For particles with large energy deviations in a machine with large chromaticity, many side-band frequencies are important to describe the motion.

2.1.3 Interaction points

The beam in colliders as the Large Hadron Collider (LHC) and the Future Circular Hadron-Hadron Collider (FCC-hh) is not a constant stream of particles. During operation, the particles are grouped longitudinally in bunches, which again are grouped in trains of varying length. The beams are crossing at multiple interaction points (IP) as illustrated in Fig. 2.4, with a nonzero full crossing angle θ_{xing}. Head on (HO) electromagnetic interactions occur between the two beams at the IPs. In an interaction region (IR) around each IP, each bunch experiences multiple additional parasitic long range (LR) interactions with bunches from the opposing beam. The LR interactions are called parasitic because they only cause deterioration of the beam, without producing particle collision events to be studied by the detectors. The crossing angle is nonzero partly to reduce the effect of these LR-interactions on the beam quality.

There are a few possible modifications that significantly alter the interactions in the IR. One can produce a nonzero displacement between the two beams in the direction perpendicular to the crossing plane. When this is done, it is to reduce the frequency of events at that given IP. It also reduces the effect of the beam-beam interactions. Another modification is the use of crab cavities

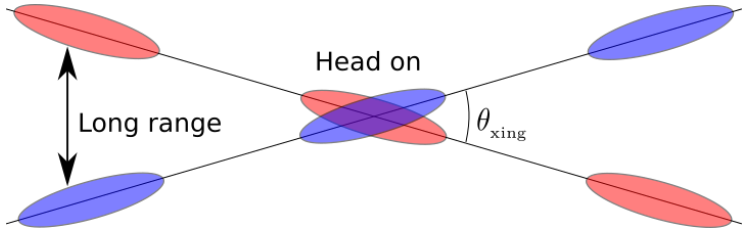

Figure 2.4: Illustration of the crossing of beam 1 and beam 2 at the IPs in circular colliders. Not to scale.

[20], proposed as a method to increase the event frequency without increasing the strongly distorting effects of the LR interactions. They work by tilting each bunch so that the two HO bunches in Fig. 2.4 overlap better, without reducing the crossing angle, ensuring that the LR interactions occur between well separated bunches.

As mentioned multiple times, the goal of a collider is to produce as many events as the physicists can analyse. The luminosity, L, is defined as the ratio of number of events detected per time per cross section, and is therefore an important performance measure of a collider. The frequency of events is

$$f_{\text{event}} = L \cdot \sigma_{\text{event}} \ , \tag{2.26}$$

where the cross section of the event, σ_{event}, is a measure for the probability of it happening. For two beams of equal size, $\sigma_{i,1} = \sigma_{i,2}$, the luminosity is [11]

$$L = \frac{N_1 N_2 f_{\text{rev}} n_{\text{b}}}{4\pi\sigma_x\sigma_y} \cdot S \cdot H \ , \tag{2.27}$$

where

$$S = \frac{1}{\sqrt{1 + \left(\frac{\sigma_s}{\sigma_x}\tan\left(\frac{\theta_{\text{xing},x}}{2}\right)\right)^2}} \ , \tag{2.28}$$

for a crossing in the horizontal plane, and

$$H = \sqrt{\pi} \cdot \frac{\beta^*}{\sigma_s} \cdot \exp\left[\left(\frac{\beta^*}{\sigma_s}\right)^2\right] \cdot \text{erfc}\left(\frac{\beta^*}{\sigma_s}\right) \ . \tag{2.29}$$

S is a correction factor for the crossing angle, being 1 for zero crossing angle, and decreasing towards zero for increasing angles. H is a correction factor for the hourglass effect [21], being 1 for small σ_s/β^*_q, and decreasing towards zero as this ratio increases. N_i is the number of particles per bunch in beam i. f_{rev} is the revolution frequency. n_{b} is the number of bunches in each beam. σ_x is the rms horizontal beam size, and equivalently σ_y is the rms vertical beam size. Both an increase of beam emittance and a loss of particles will reduce the event frequency, assuming that the crossing angle remains fixed.

The dependence of luminosity on the crossing angle is given by Eq. (2.28). From this equation, a more relevant value is the Piwinski angle $\phi_{\text{PIW},q}$ which is defined as

$$\phi_{\text{PIW},q} = \frac{\sigma_s}{\sigma_q} \cdot \frac{\theta_{\text{xing},q}}{2} \ , \tag{2.30}$$

which is equal to the second term in the denominator in Eq. (2.28) for small angles. The crossing angle is typically small, $\theta_{\text{xing}} \sim 300\,\mu\text{rad}$ in the LHC.

2.2 Beam-Beam Interaction in 4D

The focus of this thesis is the effect of the HO beam-beam interaction. This interaction can be studied by considering only one bunch per beam, and will be derived in the weak-strong regime. Beam 1 is taken to be weak and beam 2 is strong, where strong means that it can affect the distribution of the other beam, while the weak cannot. The strong bunch in beam 2 can have various distributions, leading to different electromagnetic forces, and it will remain fixed. It will, in good agreement with real bunches, be taken to be a 3D Gaussian charge distribution

$$\rho(x,y,s) = \frac{NZe}{\left(\sqrt{2\pi}\right)^3 \sigma_x\sigma_y\sigma_s} \exp\left[-\frac{x^2}{2\sigma_x^2} - \frac{y^2}{2\sigma_y^2} - \frac{s^2}{2\sigma_s^2}\right] , \tag{2.31}$$

where σ_i is the standard deviation of the Gaussian distribution in each spatial dimension separately, N is the number of particles in the strong bunch, and Z is the number of elementary charges per particle, $Z = 1$ for protons. The distribution of the weak beam is not considered at the moment, because the interaction modelled in the weak-strong model is independent of it. Effects like synchrotron radiation and damping can make the beam smaller in the vertical plane than in the horizontal plane, $\sigma_y < \sigma_x$ [22]. This effect is more prominent in high energy e^+e^- colliders than in pp colliders, related to the mass ratio between electrons and protons. The bunches are approximately round in the LHC, $\sigma_x = \sigma_y = \sigma_r$. Because the synchrotron radiation is also increasing with energy, the bunches may not be round in the FCC-hh. For nonzero crossing angle, θ_{xing}, the bunches travel on different closed orbits around the IP. Furthermore, the transverse beam sizes σ_q are dependent on $z - z_{\text{IP}}$ due to the hourglass effect discussed in Sec. 2.1.2. These effects change the beam-beam interaction as the bunches pass each other. In such a scenario, a full 6D treatment of the interaction is necessary. For $\theta_{\text{xing}} = 0$ and $\sigma_s/\beta_q^* \ll 1$, the relation between the opposing bunches changes negligibly close to the IP, and the beam-beam interaction can be derived only dependent on the transverse dimensions, as will be done in this section.

2.2.1 Round beams

For round beams, $\sigma_x = \sigma_y = \sigma_r$, the distribution in Eq. (2.31) in the rest frame of beam 2 is cylindrically symmetric as

$$\rho(r_B,\theta_B,s_B) = \frac{NZe}{\left(\sqrt{2\pi}\right)^3 \sigma_{rB}^2\sigma_{sB}} \exp\left[-\frac{r_B^2}{2\sigma_{rB}^2} - \frac{s_B^2}{2\sigma_{sB}^2}\right] , \tag{2.32}$$

where B reflects that the coordinates are in the reference frame of beam 2, $r_B = \sqrt{x_B^2 + y_B^2}$ is the transverse radius, and θ_B is the transverse polar angle, which is unimportant due to the cylindrical symmetry. Assume that the non-negligible motion of the particles in the weak beam is parallel to the s-axis, making all perpendicular lengths equal in the rest frame of beam 2 and in the lab frame, $r_B = r$. Assume that both beams cross $s = 0$ at $t = 0$. The case at hand is displayed in Fig. 2.5.

In the lab frame of IP1 and IP5 in the LHC (design), $\sigma_s = 7.55\,\text{cm}$ and $\sigma_r \approx 10\,\mu\text{m}$. In the rest frame of beam 2, $\sigma_{sB} = 563\,\text{m}$, more than 7 orders of magnitude greater than σ_r. The bunch is approximated by an infinite cylinder, and the electrical field is calculated using Gauss' law. Then the s_B-dependence is reintroduced to give

$$\mathbf{E}_B(r,\theta,s_B) = \frac{Ne}{\epsilon_0\left(\sqrt{2\pi}\right)^3 \sigma_{sB}} \left(1 - \exp\left[-\frac{r^2}{2\sigma_r^2}\right]\right) \exp\left[-\frac{s_B^2}{2\sigma_{sB}^2}\right] \frac{\mathbf{r}}{r^2} , \tag{2.33}$$

where $\mathbf{r} = (x,y)$ is the transverse position and ϵ_0 is the vacuum permittivity.

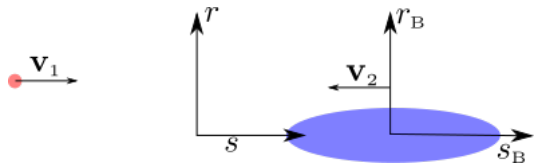

Figure 2.5: Illustration of the HO interaction of a single particle in the weak beam 1 and the Gaussian distribution of the strong beam 2. Not to scale.

The fields in the lab frame can be calculated from Eq. (2.33) using Lorentz transformations [23]

$$\mathbf{E}_\parallel = \mathbf{E}_{\parallel B} \quad , \quad \mathbf{E}_\perp = \gamma \mathbf{E}_{\perp B} \quad \text{and} \quad \mathbf{B}_\theta = \gamma \frac{\mathbf{v}_2 \times \mathbf{E}_{\perp B}}{c^2} \, . \tag{2.34}$$

The electric field parallel to the motion, $E_{\parallel B}$, that was neglected by considering the distribution as an infinite cylinder, is relatively even weaker in the lab frame due to the Lorentz transformation. The Lorentz force on particle 1 of velocity $\mathbf{v}_1 = -\mathbf{v}_2$ in the lab frame is

$$\mathbf{F} = \gamma \left(1 + \frac{v_1 v_2}{c^2}\right) e \mathbf{E}_{\perp B} \, , \tag{2.35}$$

where the second term is due to the magnetic field induced by the current of beam 2.

The force described by Eq. (2.35) acts on particle 1 only while the beams pass each other. Assume for now that the momentum changes during the interaction, but the position does not. Particle 1 is at $s_1 = v_1 t$ in the lab frame. Transforming this to the frame of beam 2, gives $s_{1B} = \gamma(v_1 + v_2)t$. The bunch length is transformed to $\sigma_{sB} = \gamma \sigma_s$. Exploiting that the force is the time derivative of the momentum, an integral expression for the change of mechanical momentum is

$$\Delta \bar{\mathbf{p}}_\mathrm{mech} = \frac{\left(1 + \frac{v_1 v_2}{c^2}\right) N e^2}{\epsilon_0 \left(\sqrt{2\pi}\right)^3 \sigma_s} \left(1 - \exp\left[-\frac{r^2}{2\sigma_r^2}\right]\right) \frac{\mathbf{r}}{r^2} \int_{-\infty}^{\infty} \mathrm{d}t \exp\left[-\frac{(v_1 + v_2)^2 t^2}{2\sigma_s^2}\right] \, . \tag{2.36}$$

In the regime at hand, both velocities approach the speed of light $v_1 = v_2 \approxeq c$. Carrying out the integral and normalising with the relativistic mechanical momentum of the design particle, $\bar{p}_0 = \gamma m_\mathrm{p} c$, one reaches the incoherent beam-beam kick for round beams

$$\Delta \mathbf{r}' = \frac{\Delta \bar{\mathbf{p}}_\mathrm{mech}}{\bar{p}_0} = \frac{2 N r_0}{\gamma} \left(1 - \exp\left[-\frac{r^2}{2\sigma_r^2}\right]\right) \frac{\mathbf{r}}{r^2} \, , \tag{2.37}$$

where the classical proton radius has been introduced as

$$r_0 = \frac{e^2}{4\pi\epsilon_0 m_\mathrm{p} c^2} \, . \tag{2.38}$$

This result can also be reached through a different approach [4], by first finding the potential of the strong bunch. The radius dependence of the beam-beam kick in Eq. (2.37) is visualised in Fig. 2.6. For small radii, the kick is approximately linear. For higher radii, the force is strongly nonlinear.

These results are obtained using the assumption of zero transverse translation during the beam-beam interaction. The assumption is valid if the transverse translation $\Delta x_q \sim \sigma_{q'} \cdot \sigma_s = \sigma_q \cdot \sigma_s / \beta_q^*$ is negligible compared to the transverse beam size, σ_q. That the ratio σ_s / β_q^* is approximately zero, was one of the requirements for the 4D approximation to be valid. Thus, if it is valid to calculate

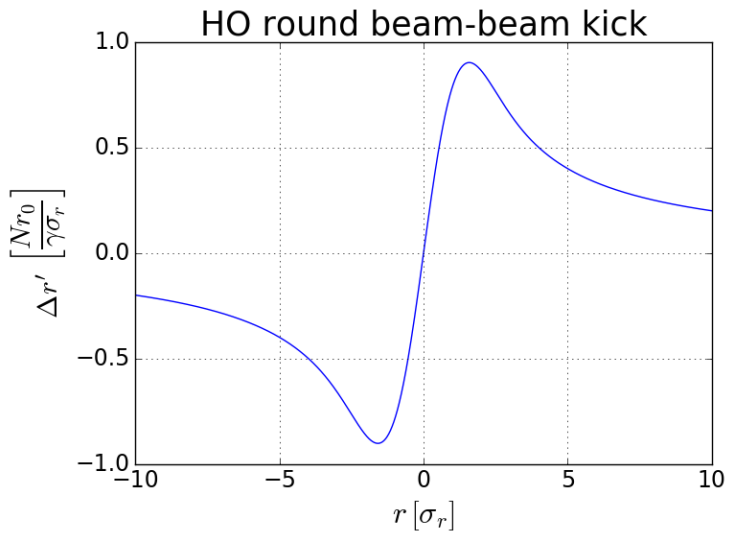

Figure 2.6: Transverse momentum kick on a charged particle from passing a round Gaussian bunch of charged particles of the same charge. Note that the horizontal axis is given in units of transverse beam size of the strong beam, most particles experience the approximately linear kick in the centre.

the kick from only the transverse coordinates, it is valid to assume that the change of the transverse position of particle 1 during the interaction is negligible. It should also be checked similarly that the beam-beam kick does not change the position of the particles. To test this, consider a worst-case scenario, that the entire kick is done at the beginning of the interaction. Using values from the LHC design report [3], the transverse translation is of order $\sigma_q \times 10^{-7}$. The assumptions are valid, in the context of 4D interactions.

2.2.2 Flat beams

If the bunches are flat, $\sigma_x \neq \sigma_y$, one has to derive the force from the more general distribution in Eq. (2.31). The electric field in the lab frame has been derived assuming that the distribution only varies negligibly in the longitudinal direction [24]. For $\sigma_x > \sigma_y$ the electric fields are

$$E_y + \mathrm{i}E_x = \frac{Ne}{2\epsilon_0\sqrt{\sigma_x^2 - \sigma_y^2}}\left(\mathrm{w}\left[\frac{x+\mathrm{i}y}{\sqrt{2(\sigma_x^2-\sigma_y^2)}}\right] - \exp\left[-\frac{x^2}{2\sigma_x^2} - \frac{y^2}{2\sigma_y^2}\right]\cdot\mathrm{w}\left[\frac{x\frac{\sigma_y}{\sigma_x} + \mathrm{i}y\frac{\sigma_x}{\sigma_y}}{\sqrt{2(\sigma_x^2-\sigma_y^2)}}\right]\right) , \tag{2.39}$$

where $\mathrm{w}[a+\mathrm{i}b]$ is the Faddeeva function, sometimes referred to as the complex error function

$$\mathrm{w}[t] = \exp\left[-t^2\right]\left(1 + \frac{2\mathrm{i}}{\sqrt{\pi}}\int_0^t \exp\left[u^2\right]\mathrm{d}u\right) . \tag{2.40}$$

The magnetic fields can be calculated using the Lorentz transformations in Eq. (2.34). The forces can be found by entering the fields into the expression for the Lorentz force. This gives the

following expression for the beam-beam kick from flat beams

$$\Delta y' + \mathrm{i}\Delta x' = \frac{N r_0 \sqrt{2\pi}}{\gamma\sqrt{\sigma_x^2 - \sigma_y^2}} \left(\mathrm{w}\left[\frac{x + \mathrm{i}y}{\sqrt{2(\sigma_x^2 - \sigma_y^2)}} \right] - \exp\left[-\frac{x^2}{2\sigma_x^2} - \frac{y^2}{2\sigma_y^2} \right] \cdot \mathrm{w}\left[\frac{x\frac{\sigma_y}{\sigma_x} + \mathrm{i}y\frac{\sigma_x}{\sigma_y}}{\sqrt{2(\sigma_x^2 - \sigma_y^2)}} \right] \right) , \tag{2.41}$$

which converges to the expression in Eq. (2.37) when $\sigma_x \to \sigma_y$.

The horizontal and vertical momentum kicks have been plotted in Fig. 2.7 for the flatness ratios $\sigma_x/\sigma_y \in \{1.01, 100\}$. When the beam is almost round, the kicks are approximately equal in the two transverse planes and equal to the kick for round beams displayed in Fig. 2.6, as they should be. For a strongly flattened beam in the horizontal direction, the kick is very different in the two planes. In the vertical plane, the charge appears confined at origo, giving an almost immediate local maximum before the kick strength falls off. The opposite happens in the horizontal plane, where the linear regime is now stretched out further than in the round bunch regime. This picture is dependent on the normalisation of the axes. If two equally flat bunches interact, the particles of low vertical amplitude, $A_y < \sigma_y$, are in the approximately linear region.

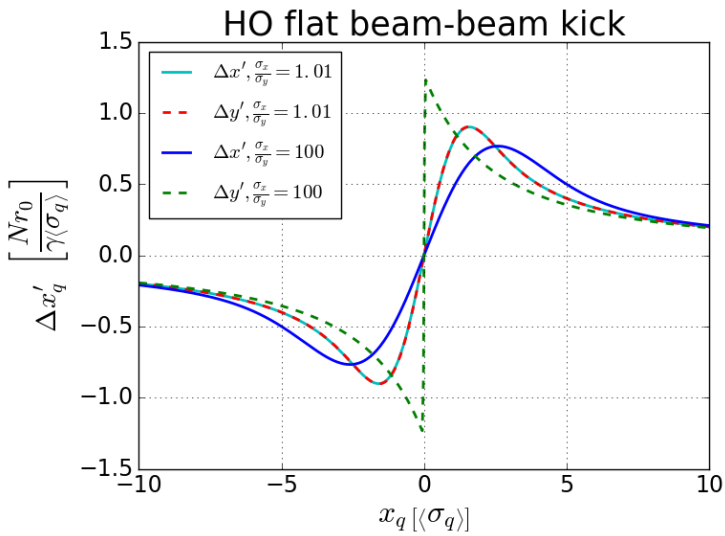

Figure 2.7: Transverse momentum kick on a particle from passing a flat Gaussian beam, consisting of particles of the same charge. The horizontal axis is given in units of average transverse beam size of the strong beam, $\langle\sigma_q\rangle = (\sigma_x + \sigma_y)/2$. The kick is different in the horizontal and vertical directions.

2.2.3 Beam-beam tune shift

The beam-beam interaction causes a tune shift from the machine tunes Q_q. To find this shift, consider first the interaction in the linear region in the centre, $x_q \approx 0$. For round beams, the kick can in this region be given as a transfer matrix

$$\begin{pmatrix} x_q \\ x'_q \end{pmatrix}_{T+BB} = \mathbf{K}_{BB,q}(2\kappa) \begin{pmatrix} x_q \\ x'_q \end{pmatrix}_T \quad , \quad \mathbf{K}_{BB,q}(\kappa) = \begin{pmatrix} 1 & 0 \\ \kappa & 1 \end{pmatrix} , \tag{2.42}$$

where $\kappa = Nr_0/2\gamma\sigma_q^2$, and BB is a subscript to tell it is the beam-beam transfer matrix. The one-turn-map starting at the centre of one IP, assuming only one IP, can be expressed through matrix concatenation as

$$\mathbf{T}_{\mathrm{OTM}} = \mathbf{K}_{BB,q}\left(\kappa\right)\mathbf{R}_q\left(\mu_q\right)\mathbf{K}_{BB,q}\left(\kappa\right) \ . \tag{2.43}$$

Remembering that $\alpha_q = 0$ at the IPs, and assuming that the beam-beam kick expressed through κ is weak, the one-turn map is

$$\mathbf{T}_{\mathrm{OTM}} = \begin{pmatrix} \cos\left(\mu_q - \kappa\beta_q^*\right) & \beta_q^*\sin\left(\mu_q - \kappa\beta_q^*\right) + \mathcal{O}(\kappa) \\ -\gamma_q^*\sin\left(\mu_q - \kappa\beta_q^*\right) + \mathcal{O}(\kappa) & \cos\left(\mu_q - \kappa\beta_q^*\right) \end{pmatrix} . \tag{2.44}$$

By insertion of the expression for κ, one finds that the beam-beam interaction has reduced the rotation in phase space. The amount is commonly given as the beam-beam tune shift $\Delta Q_{q,BB}$, which for particles of zero transverse amplitude is

$$\Delta Q_{q,BB} = -\frac{Nr_0}{4\pi\gamma\epsilon_q} \ . \tag{2.45}$$

The beam-beam parameter ξ_q is a measure on the strength of the beam-beam interaction [11]. For round beams, the parameter can be calculated by using the expression in Eq. (2.37) to get for both transverse planes

$$\xi_q = -\frac{\beta^*}{4\pi}\frac{\mathrm{d}\Delta x_q'}{\mathrm{d}x_q}\bigg|_{r=0} = -\frac{Nr_0}{4\pi\gamma\epsilon_q} \ . \tag{2.46}$$

That is, the beam-beam parameter is equal to the beam-beam tune shift for particles of zero transverse amplitude, $|\mathbf{r}| = 0$. For flat beams, the beam-beam parameter is different for the two transverse planes

$$\xi_q = -\frac{Nr_0\beta_q^*}{2\pi\gamma\sigma_q(\sigma_x + \sigma_y)} \ , \tag{2.47}$$

which reduces to the expression in Eq. (2.46) in the limit of round beams. If $\sigma_x > \sigma_y$, the maximum beam-beam tune shift is largest in the vertical plane if $\epsilon_x > \epsilon_y$ and $\beta_x^* = \beta_y^*$, and largest in the horizontal plane if $\epsilon_x = \epsilon_y$ and $\beta_x^* > \beta_y^*$. The beam-beam parameter and the beam-beam tune shift are negative for beams of the same charge. This thesis refers to the negative of both values after this chapter.

The dependence of the tune shift for round beams on the amplitude A_q, can be calculated in many ways. A comprehensible classical 2D approach can be found in App. B of [4], which rewritten in the notation of this thesis is

$$\Delta Q_q(a_q) = -\frac{Nr_0}{4\pi\gamma\epsilon_q}\cdot\frac{4}{a_q^2}\left(1 - \exp\left[-\frac{a_q^2}{4}\right]\cdot I_0\left(\frac{a_q^2}{4}\right)\right) \quad , \quad a_q = \frac{\sqrt{2J_q\beta_q^*}}{\sigma_q} \ , \tag{2.48}$$

where $a_q = A_q/\sigma_q$ is the normalised amplitude in the given plane. This expression is assuming zero amplitude in the other transverse plane. The dependence of the beam-beam tune shift on the amplitude in position space is plotted in Fig. 2.8. The tune shift is largest for particles of zero transverse amplitude, equal to the beam-beam parameter.

The tune shift may cause problems in the presence of resonances, which will be considered in Sec. 2.3. The bunches may be separated at the IP to reduce the tune shift and problematic effects that come with it. The effect of separation at the IP can also be used to understand the effects of LR interactions. One can apply the same method, used to get the horizontal beam-beam tune shift as in Eq. (2.48), to get the tune shift for particles in a weak bunch that is separated from the strong bunch either in the horizontal or the vertical plane. The dependence of the horizontal beam-beam

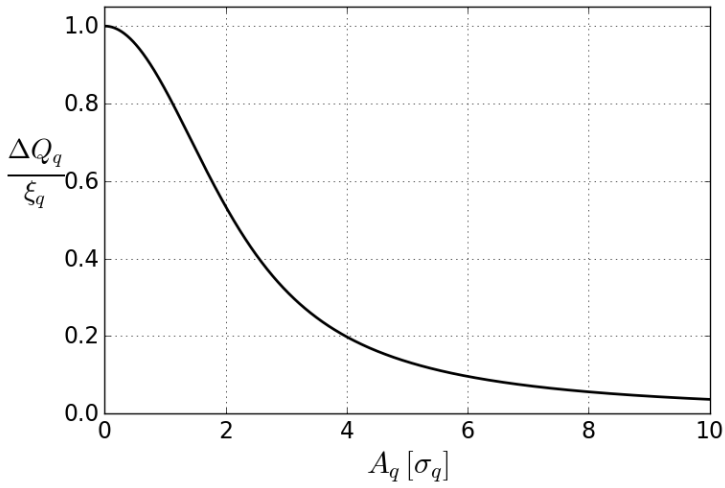

Figure 2.8: Dependence of the beam-beam tune shift, ΔQ_q, on the amplitude of the particle in position space, in units of the transverse beam size of the strong beam, σ_q.

tune shift on the amplitude in horizontal phase space and separation in either transverse plane, is presented in Fig. 2.9. Zero separation produces the tune shift already found above. Separation in the horizontal plane causes a horizontal tune shift of opposite sign of the beam-beam parameter. Separation in the vertical plane reduces the value of the horizontal tune shift, but does not change the sign. The tune shift reduces for increasing separation in both planes. For $\Delta x_q = 10\sigma_q$, the tune shift for particles in the core of the bunch has been reduced to $|\Delta Q_x(0)| = 0.02 \cdot \xi_x$.

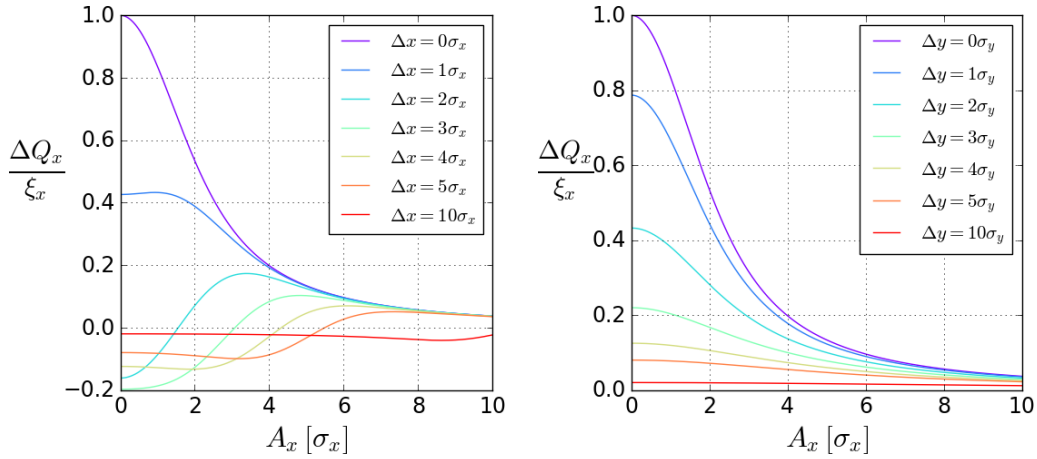

Figure 2.9: Dependence of horizontal beam-beam tune shift, ΔQ_x, for round beams, on the separation in the transverse planes in units of the transverse beam size of the strong beam. The tested particles only distributed in horizontal phase space. (**a**) displays the tune shift for a horizontal separation. (**b**) displays the tune shift for a vertical separation.

It is more difficult to get an analytical expression for the tune shift in two dimensions simultaneously. Nevertheless, it can be estimated numerically. The combined tune shift from the machine tunes (Q_{x0}, Q_{y0}) for particles oscillating with different amplitudes, called the tune footprint, is displayed in Fig. 2.10. The maximum tune shift in either plane is equivalent to $\xi_{q,\mathrm{Tot}}$, and occurs for particles of zero transverse amplitude. The horizontal tune shift decreases for $x = 0$ when y increases, but slower than when $y = 0$ and x increases, similar to what was found for vertical separation in Fig. 2.9b. This behaviour causes the width of the footprint to be nonzero.

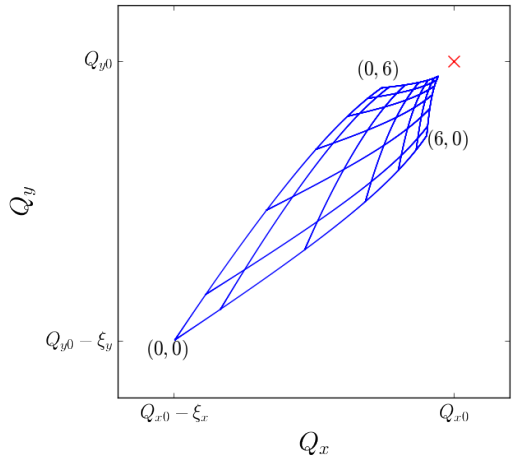

Figure 2.10: Tune footprint caused by the beam-beam tune shift in both transverse planes simultaneously. The lines correspond to $x/\sigma_x = \{0, 1, 2, 3, 4, 5, 6\}$ and $y \in [0, 6]$, or vice versa. The markers on the corners of the footprint correspond to the normalised amplitude in horizontal and vertical phase space, i.e. $(0, 6)$ means $A_x = 0 \cdot \sigma_x$ and $A_y = 6 \cdot \sigma_y$.

What has been presented in this section has assumed a small beam-beam parameter, ξ_{Tot}, and that resonances do not affect the motion of the particles. For larger beam-beam parameters, as will be studied in Ch. 4, the particles will be affected by resonances. The tune shift is for large beam-beam parameters also dependent on the machine tune caused by the lattice. The maximal tune shift varies the most for tunes close to integers and half integers [25].

2.3 Resonances and Resonance Cancelling

2.3.1 Resonances

The particles oscillate in phase space, in a way similar to free oscillations of a harmonic oscillator. However, a circular beam lattice is not ideal, due to nonlinear field imperfections of the magnets, misalignments between elements, and vibrations [26]. In addition, the nonlinear beam-beam interaction affects the motion of the particles. Because the beam passes the same part of the collider multiple times per second, these forces act on the particles periodically, causing forced oscillations [15]. If the forces accumulate effect over multiple turns, strong resonances may cause emittance growth and beam losses. The resonances are introduced conceptually at first, for a more mathematical approach, go directly to Sec. 2.3.2.

Consider first the possibility of a dipole error, for instance in the form of one dipole producing a stronger magnetic field than designed, or a dipole component in some other lattice element. The magnetic field of a dipole was presented in Eq. (2.13). It is ideally equal at every point in the

transverse aperture of the beam. If the tunes were integers,

$$Q_q = p \quad , \quad p \in \mathbb{Z} \, , \tag{2.49}$$

the particles would return to the same position in the Poincaré section every turn, and be kicked in the same direction at the location of the error. Unless corrected for, this would lead to increasingly large transverse amplitudes until the particles were lost from the machine.

Consider next a quadrupole error. The magnetic field of a quadrupole magnet was presented in Eq. (2.14). The horizontal force created by this magnet will be proportional to x. Therefore, the kicks will add up if the tunes are either integers or half integers,

$$2 \cdot Q_q = p \quad , \quad p \in \mathbb{Z} \, , \tag{2.50}$$

and the particles will again be lost. These resonances are second order. This process can be continued to magnetic fields of higher orders. In general, one finds that localised kicks proportional to the transverse coordinates to power $(n-1)$, can cause resonances of n-th order. Combinations of multiple higher-order kicks can cause resonances of even higher order.

Due to mixing between the two planes, resonances may not only depend on the individual tunes Q_x and Q_y, but on the combination of them. A general expression for transverse betatron resonances can be written as

$$k \cdot Q_x + l \cdot Q_y = p \quad , \quad k, l, p \in \mathbb{Z} \, , \tag{2.51}$$

where k, l and p are integers. The tunes that fulfill this relation make up lines in tune space of resonance order

$$n = |k| + |l| \, . \tag{2.52}$$

All resonances up to order 5 are shown in tune space, (Q_x, Q_y), in Fig. 2.11a. The magnetic errors do cause problems, requiring the usage of high field quality magnets. Yet, the working point must be chosen to avoid the resonance lines for realistic magnetic imperfections. Commonly, the machine tunes chosen in actual colliders are close to the coupling resonance, $Q_x = Q_y$, highlighted red in the graph.

The beam-beam interaction is possibly more problematic than lattice errors. First of all, this is because the strength of the beam-beam interaction is closely bound to the luminosity, seen by comparison of the beam-beam parameter in Eq. (2.47) and the luminosity in Eq. (2.27). One cannot achieve the high luminosity required without having strong beam-beam interactions. Another problem is that the interaction is strongly nonlinear, caused by the exponential term in the beam-beam kick for round beams in Eq. (2.37). The exponential function can be expanded as

$$\exp[x] = \sum_{i=0}^{\infty} \frac{x^i}{i!} \, , \tag{2.53}$$

depending gradually less on larger i due to the factorial in the denominator. All resonance lines up to order 20 are plotted in Fig. 2.11b. This emphasises the problem of choosing machine tunes that do not overlap with any beam-beam driven resonance, especially considering that the beam-beam interaction also causes a spread of the tunes for particles at different amplitudes in the beam. The kick is however gradually weaker for larger order and, as will be shown later, the resonances of higher order n are usually weaker and consequently less problematic.

What has been presented above is the situation caused by the transverse motion alone. If the motion is also coupled between the longitudinal and transverse planes, synchro-betatron resonances

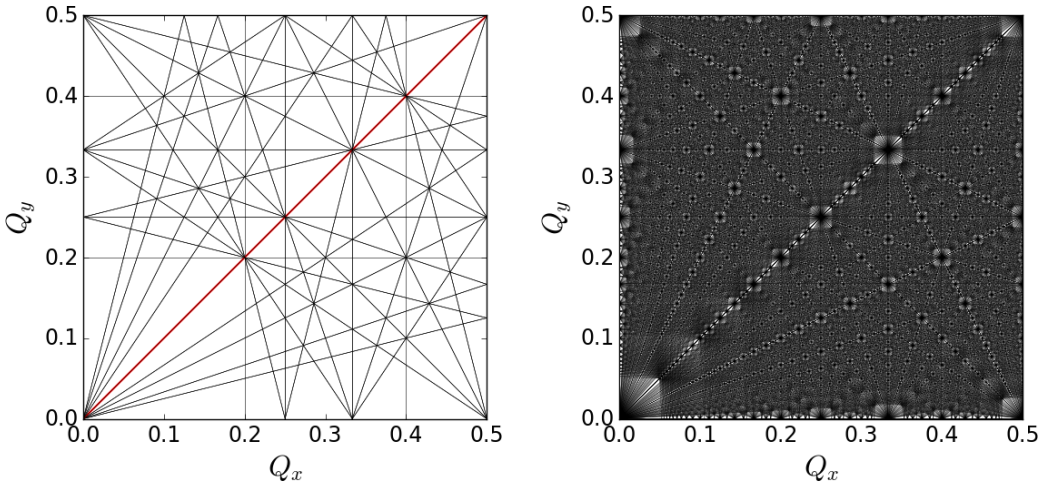

Figure 2.11: Resonance lines in tune space (Q_x, Q_y). (**a**) displays all resonance lines up to order 5. The red line corresponds to the coupling resonance. (**b**) displays all resonance lines up to order 20, relevant due to the beam-beam interaction.

are relevant. As was derived for the regular motion due to chromaticity in Eq. (2.25), these resonances come as side-bands to the betatron resonances. The general expression for resonances in 6D is therefore

$$k \cdot Q_x + l \cdot Q_y + m \cdot Q_s = p \quad , \quad k, l, m, p \in \mathbb{Z} \, . \tag{2.54}$$

This makes it increasingly difficult to avoid all resonances in tune space. As it is impossible in theory to avoid all of them, it is of interest to understand which of the resonances are the most problematic.

2.3.2 Resonances through Lie theory

There are multiple approaches to study the nonlinearity of the beam-beam interaction quantitatively. The method presented here is based on Lie transfer maps. Formulation of the technique and application to a single IP for one transverse direction can be found in [27]. Further scaling to two IPs is done in [4, 6]. This section studies a 2D transverse phase space. The results are valid for both the horizontal and vertical directions separately.

A particle in a lattice is subject to the one-turn-map given in Eq. (2.15). The rotation can be considered from the IP, where β is at a local minimum, $\alpha = 0$ and $\gamma = 1/\beta$. The linear lattice can be written in Lie maps as

$$e^{:f:} \quad , \quad f = -\frac{\mu}{2}\left(\frac{x^2}{\beta} + \beta x'^2\right) = -\mu J \, , \tag{2.55}$$

where f is the effective Hamiltonian, which is conserved by definition. It is linear in the action J, which has already been shown to be a constant for this motion.

Particles that move through an IP experience the nonlinear beam-beam kick given in Eq. (2.37), assuming round bunches. The kick can be expressed by the Lie map

$$e^{:F:} \quad , \quad F(x) = \int_0^x \mathrm{d}\chi \, \Delta x'(\chi) \, , \tag{2.56}$$

where $-F$ is the potential due to the beam-beam force. F can be expanded in a Fourier series

$$F(x) = \sum_{-\infty}^{\infty} c_n(J) e^{in\phi} \quad , \quad c_n(J) = \frac{1}{2\pi} \int_0^{2\pi} \mathrm{d}\phi \, e^{-in\phi} F(x) \, . \tag{2.57}$$

The Fourier coefficients $c_n(J)$ in the beam-beam Lie map can be expressed as

$$c_n(J) = \frac{Nr_0}{\gamma} \int_0^{J\beta/2\sigma} \frac{\mathrm{d}\alpha}{\alpha} \begin{cases} (1 - e^{-\alpha} I_0(\alpha)) & \text{, if } n = 0 \\ 0 & \text{, if } n = \text{odd} \\ -e^{-\alpha} I_{n/2}(\alpha) & \text{, otherwise} \end{cases} , \tag{2.58}$$

where I are the modified Bessel functions of the first kind [27]. Because the beam-beam force is an odd function, only the even coefficients of its potential are nonzero. This is not true if there is a transverse separation or a nonzero crossing angle between the beams. The first four nonzero coefficients are plotted in Fig 2.12. The horizontal axis in the plot is the amplitude in position space as in Eq. (2.7), normalised by the standard deviation. Two things to note are that the coefficient strength increases with the action J, and that it decreases with increasing n. That is, beam-beam resonances of higher order n have smaller resonance coefficients, and all nonzero resonance coefficients are larger at larger transverse amplitudes.

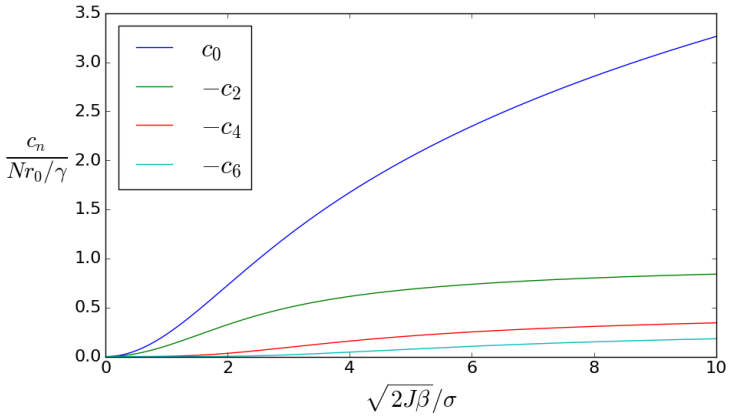

Figure 2.12: Fourier coefficients for the beam-beam potential. The horizontal axis is amplitude in position space in units of the transverse beamsize σ of the strong beam.

The two Lie maps for the lattice and the beam-beam kick can be concatenated together using the BCH formula, which reads

$$e^{:h:} = e^{:f:} e^{:F:} \approx \exp\left[: f + \frac{:f:}{1 - e^{-:f:}} F + \mathcal{O}(F^2) : \right] . \tag{2.59}$$

Given that the beam-beam interaction, represented by F, is weak and only needs to be included to the first order, this gives after some arithmetic an expression for the effective Hamiltonian

$$h = -\mu J + \sum_{n=0}^{\infty} c_n(J) \frac{n\mu}{2\sin\left(\frac{n\mu}{2}\right)} \exp\left[in\phi + \frac{in\mu}{2} \right] . \tag{2.60}$$

The constant of motion, h, now depends on the angle ϕ in phase space. The action J is thus no longer independent of the angle ϕ.

The effective Hamiltonian gives rise to a resonance condition when the sine in the denominator is zero

$$Q = \frac{\mu}{2\pi} = \frac{m}{n} \quad , \quad m \in \mathbb{Z},\, n \in \mathbb{N}\,. \tag{2.61}$$

This can easily be generalised to a 2D transverse resonance condition

$$k \cdot Q_x + l \cdot Q_y = p \quad , \quad k, l, p \in \mathbb{Z}\,, \tag{2.62}$$

equal to Eq. (2.51). Resonance lines up to order 20 are plotted in Fig. 2.13, with the requirement that k and l are even. The strength of the resonances is linked to the Fourier coefficients $c_n(J)$, which can be calculated in 1D using Eq. (2.25). This can be extended to 2D using numerical solutions to calculate the coefficients, which has been done by a code developed at CERN [28]. These coefficients have been used to weight the resonance lines. The cancellation of odd resonances has reduced the density of resonance lines in comparison to Fig. 2.11, where all resonance lines were displayed. The area between the strong 4th order and 6th order resonance lines is displayed in Fig. 2.13b, including the LHC working point, $(Q_x, Q_y) = (0.31, 0.32)$, marked by a red cross.

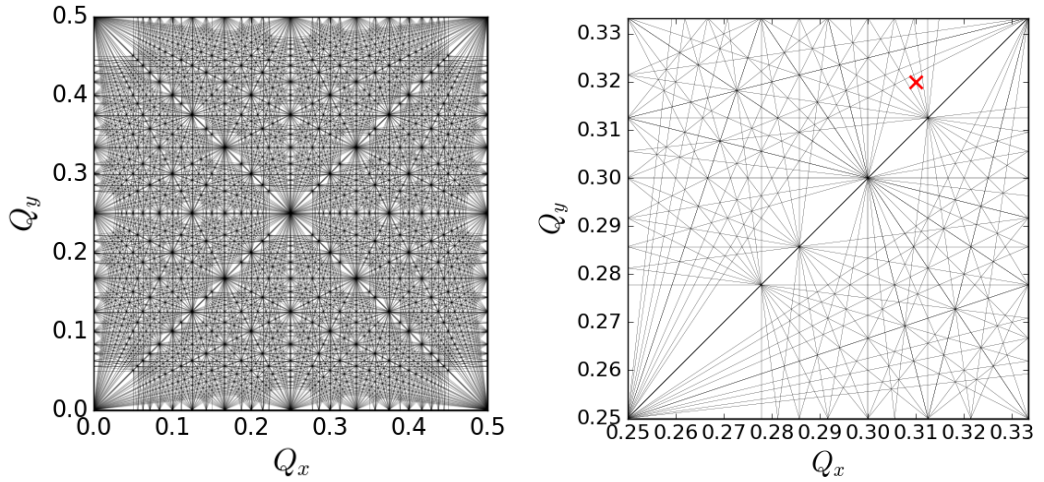

(a) **(b)**

Figure 2.13: All resonance lines up to order 20 with nonzero Fourier coefficients. The tune space comparable to Fig. 2.11 is shown in (**a**), while the square between the strong 4th order and 6th order resonances is shown in (**b**). The red cross in (**b**) is the machine tune used in the LHC.

As the Hamiltonian diverges, there is no longer a strict relationship between the action J and the phase angle ϕ. The dynamics of Hamiltonian systems close to resonances are complex. Multiple mechanisms can lead to diffusion [14]. Numerical simulations are needed to evaluate the effect of the resonances on the single particle diffusion.

The resonance condition has strong implications for which tunes it is safe to operate at, because the effect of the resonance may lead to diffusion of the particles towards higher actions. If the tune of a particle is far from strong resonances, then the efficient Hamiltonian can be averaged over the angle to give

$$\langle h \rangle = -\mu J + c_0(J)\,. \tag{2.63}$$

The constant tune $Q = \mu/2\pi$ has apparently been shifted by the action dependent beam-beam interaction

$$\Delta Q = -\frac{1}{2\pi}\frac{\mathrm{d}c_0(J)}{\mathrm{d}J} \,. \tag{2.64}$$

Applying the fundamental theorem of calculus gives

$$\Delta Q = -\frac{Nr_0}{4\pi\gamma\epsilon_x}\cdot\frac{1}{x}\left(1 - e^{-x}I_0(x)\right) \quad , \quad x = \frac{J\beta^*}{2\sigma^2} \,. \tag{2.65}$$

The beam-beam tune shift in Eq. (2.48) is thus recovered. Deriving the beam-beam tune shift in this manner makes it obvious that the expression is only valid when resonances do not affect the Hamiltonian.

2.3.3 Resonance cancelling

Consider next a similar setting where the change is that there are now two IPs instead of one, splitting the lattice in two separate parts. In the LHC, IP1 and IP5 are diametrically positioned. The beam performs betatron rotations, with phase advances μ_1 and μ_2 in the two parts of the lattice. In total $\mu_1 + \mu_2 = \mu$ as in the entire lattice in the previous case. The four separate Lie maps can be concatenated

$$e^{:h_2:} = e^{:f(\mu_1):}e^{:F:}e^{:f(\mu_2):}e^{:F:} \,, \tag{2.66}$$

which gives an expression for the effective Hamiltonian to first order in the beam-beam interaction using the BCH-formula [6]

$$h_2 = -\mu J + 2c_0(J) + \sum_{n=2}^{\infty}\frac{2n\mu c_n(J)}{\sin\left(\frac{n\mu}{2}\right)}\cos\left[n\left(\phi + \frac{\mu}{2} + \frac{\mu_1}{2}\right)\right]\cos\left(\frac{n\mu_1}{2}\right) \,. \tag{2.67}$$

In comparison to Eq. (2.63), the beam-beam tune shift has doubled as the number of IPs has doubled.

The effective Hamiltonian, h_2, gives rise to the same resonance condition as before, when the sine in the denominator is zero. However, with carefully adjusting the intermediate phase advance between the two IPs, μ_1, it is possible to cancel these resonances. This can be achieved when the cosine in the nominator is zero as well, leading to the following resonance-cancelling condition on the intermediate phase advance

$$\mu_1 = \frac{2m+1}{n}\cdot\pi \quad , \quad m \in \mathbb{Z}, n \in \mathbb{N} \,, \tag{2.68}$$

for cancelling resonances of order n. $c_n(J)$ is still zero for odd n, and larger for smaller n. Two strong resonances close to the LHC operation point are the 4th order at $Q = 1/4$ and the 6th order at $Q = 1/3$. The 4th order resonance can according to this be cancelled if $\mu_1 = \{\pi/4, 3\pi/4, ...\}$. The 6th order can likewise be cancelled if $\mu_1 = \{\pi/6, 3\pi/6, ...\}$. This effect was studied and found effective for individual resonances in part one of this project [1]. There is no common initial phase advance that can cancel resonances of order $n = 4 \cdot m$, where m is an integer. The resonances of order $n = 2 \cdot (2m + 1)$ may however be cancelled if $\mu_1 = \{\pi/2, 3\pi/2, ...\}$. That is, resonances of order $n = \{2, 6, 10, ...\}$ can be cancelled simultaneously according to this theory.

Another suggestion for a phase advance that improves the beam quality is

$$\mu_1 = \frac{\mu}{2} \,, \tag{2.69}$$

i.e. splitting the phase advance equally between the two separate parts of the lattice. This phase advance was found from a symmetry perspective [6], and confirmed numerically through trial to give the best performance [10]. The suggested intermediate phase advances in Eq. (2.68) and Eq. (2.69) will be tested in this thesis.

2.4 Beam-Beam Interaction in 6D

The beam-beam interaction was derived with a 4D treatment in Sec. 2.2. That method was justified in the limit of zero crossing angle, $\theta_{\text{xing}} = 0$, and negligible hourglass effect, $\sigma_s/\beta_q^* \ll 1$. In real accelerators, the crossing angle is in general nonzero and the hourglass effect is non-negligible. Currently $\sigma_s/\beta_q^* = 0.19$ in the LHC during normal physics fills [29], and it is expected to increase with the future improvements to HL-LHC and FCC-hh. The nonzero crossing angle has the effect that the transverse distance between the bunch centres is not constant throughout each bunch, as was visualised in Fig. 2.4. The hourglass effect causes the transverse beam size, σ_q, of the bunches charge distribution in Eq. (2.31), to be dependent on the longitudinal distance from the IP, $z - z_{\text{IP}}$. If either of these effects are present, the longitudinal dependence of the beam-beam kick is no longer negligible and a 6D kick is needed.

It is possible to directly calculate the kick of one bunch on another, as they pass with a nonzero crossing angle. The problem can also be separated into

1. Lorentz transformation ($\mathcal{L}$) to boosted frame where two tilted bunches collide head-on [30].
2. Perform a symplectic 6D synchro-beam mapping (SBM) [31].
3. Inverse Lorentz transformation ($\mathcal{L}^{-1}$) back to the accelerator coordinates.

This method was introduced in [30], and it is how the beam-beam interaction is calculated in tracking codes such as SixTrack [32], and also in CABIN.

2.4.1 Transformation to head-on frame

The transformation from accelerator coordinates to a head-on frame is straightforward [30]. Here I derive it and its inverse in more detail. Consider an IP in a circular collider, located at $z_{\text{IP}} = 0$ for ease of notation. The steps depicted in the list above produce new combinations of the same variables. The Lorentz transformation $\mathcal{L}$ consists of a transformation from accelerator coordinates to lab frame coordinates by matrices $\mathbf{A}$ and $\mathbf{B}$, followed by a Lorentz rotation and boost to the head-on frame by a matrix $\mathbf{L}$, before the lab frame coordinates are transformed back to accelerator coordinates and shifted to $z^* = 0$. The coordinates after each step are distinguished by different notation as

$$\mathbf{x}(0) \xrightarrow{\mathbf{A},\mathbf{B}} \mathbf{X}(0) \xrightarrow{\mathbf{L}} \mathbf{X}^*(z^*) \xrightarrow{\mathbf{A}^{-1},\mathbf{B}^{-1}} \mathbf{x}^*(z^*) \to \mathbf{x}^*(0^*)\,, \tag{2.70}$$

where the argument (0) signifies that the values are taken at the IP, $z = 0$. The goal of this transformation is to go from the problem expressed in accelerator coordinates in Fig. 2.14a to the problem of head-on collisions between tilted bunches in Fig. 2.14b. We will consider the problem of a horizontal crossing angle, but the results are directly transferable to a vertical crossing angle.

The accelerator coordinate system has already been defined as $\mathbf{x} = (x, x', y, y', s, \delta; h, z)$. For readability, the canonical momenta x'_q will be written as p_q in this section, making $\mathbf{x}$ equal to $(x, p_x, y, p_y, s, \delta; h, z)$. If the reader is used to Hirata's notation, note the exchange of s and z. The h is the effective Hamiltonian, defined as

$$h(p_x, p_y, \delta) = 1 + \delta - \sqrt{(1+\delta)^2 - p_x^2 - p_y^2}\,, \tag{2.71}$$

which is the momentum along the reference trajectory. Instead of the full crossing angle θ_{xing}, the half crossing angle appears many times in this derivation, and for ease of notation it is defined as

$$\theta_{\text{h}} = \frac{\theta_{\text{xing}}}{2}\,. \tag{2.72}$$

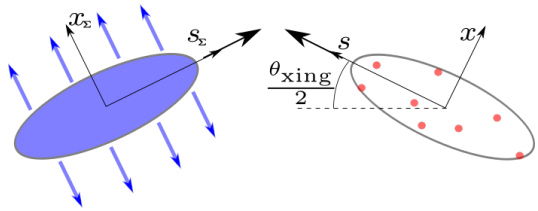

(a)

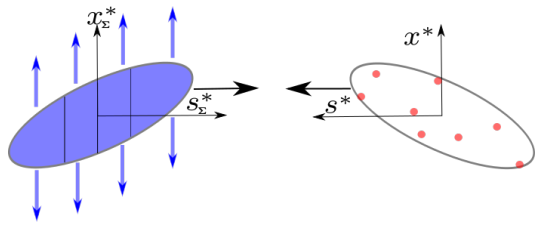

(b)

Figure 2.14: Beam-beam interaction at the IP with nonzero crossing angle. The strong bunch is blue, and its coordinates have a subscript Σ, while the weak bunch is represented by incoherent red particles. (**a**) displays the situation in accelerator coordinates. (**b**) displays the situation in the head-on frame after the full Lorentz transformation $\mathcal{L}$.

The Lorentz boost, $\mathbf{L}$, transforms particles that are expressed in the laboratory coordinates, $\mathbf{X} = (X, P_X, Y, P_Y, S, P_S; H, T)$. H is the real Hamiltonian, i.e. the energy, T is the actual time, S is the distance from the IP in the lab frame, and P_i are the mechanical momenta in the three directions. These are related to the accelerator coordinates through

$$\begin{pmatrix} cT \\ X \\ S \\ Y \end{pmatrix} = \mathbf{A} \begin{pmatrix} s(z) \\ x(z) \\ z \\ y(z) \end{pmatrix} \text{ , where } \quad \mathbf{A} = \mathbf{A}^{-1} = \begin{pmatrix} -1 & 0 & 1 & 0 \\ 0 & 1 & 0 & 0 \\ 0 & 0 & 1 & 0 \\ 0 & 0 & 0 & 1 \end{pmatrix} , \tag{2.73}$$

and

$$\begin{pmatrix} \frac{H}{c} - \bar{p}_0 \\ P_X \\ P_S - \bar{p}_0 \\ P_Y \end{pmatrix} = \bar{p}_0 \mathbf{B} \begin{pmatrix} \delta \\ p_x \\ h \\ p_y \end{pmatrix} \text{ , where } \quad \mathbf{B} = \mathbf{B}^{-1} = \begin{pmatrix} 1 & 0 & 0 & 0 \\ 0 & 1 & 0 & 0 \\ 1 & 0 & -1 & 0 \\ 0 & 0 & 0 & 1 \end{pmatrix} , \tag{2.74}$$

where $\bar{p}_0$ is the absolute value of the momentum of the design particle. The matrices $\mathbf{A}$ and $\mathbf{B}$ are their own inverses separately.

The Lorentz transformation that will make the collision head-on, consists of first a rotation counter clockwise by an angle θ_{h}, $\mathbf{L}_{\text{rot}}$, followed by a boost in the direction of the rotated x coordinate, $\mathbf{L}_{\text{boost}}$. These operations are well known to be given by

$$\mathbf{L}_{\text{rot}} = \begin{pmatrix} 1 & 0 & 0 & 0 \\ 0 & \cos(\theta_{\text{h}}) & \sin(\theta_{\text{h}}) & 0 \\ 0 & -\sin(\theta_{\text{h}}) & \cos(\theta_{\text{h}}) & 0 \\ 0 & 0 & 0 & 1 \end{pmatrix} , \quad \mathbf{L}_{\text{Boost}} \begin{pmatrix} \sec(\theta_{\text{h}}) & -\tan(\theta_{\text{h}}) & 0 & 0 \\ -\tan(\theta_{\text{h}}) & \sec(\theta_{\text{h}}) & 0 & 0 \\ 0 & 0 & 1 & 0 \\ 0 & 0 & 0 & 1 \end{pmatrix} , \tag{2.75}$$

and concatenated as $\mathbf{L} = \mathbf{L}_{\mathrm{Boost}}\mathbf{L}_{\mathrm{rot}}$. The Lorentz transformation is thus applied as

$$\begin{pmatrix} cT^* \\ X^* \\ S^* \\ Y^* \end{pmatrix} = \mathbf{L} \begin{pmatrix} cT \\ X \\ S \\ Y \end{pmatrix} \quad \text{and} \quad \begin{pmatrix} \frac{H^*}{c} \\ P_X^* \\ P_S^* \\ P_Y^* \end{pmatrix} = \mathbf{L} \begin{pmatrix} \frac{H}{c} \\ P_X \\ P_S \\ P_Y \end{pmatrix} , \tag{2.76}$$

where the $*$ signifies that the coordinates are in the boosted frame, as in Eq. (2.70), and

$$\mathbf{L} = \begin{pmatrix} \sec(\theta_{\mathrm{h}}) & -\sin(\theta_{\mathrm{h}}) & -\tan(\theta_{\mathrm{h}})\sin(\theta_{\mathrm{h}}) & 0 \\ -\tan(\theta_{\mathrm{h}}) & 1 & \tan(\theta_{\mathrm{h}}) & 0 \\ 0 & -\sin(\theta_{\mathrm{h}}) & \cos(\theta_{\mathrm{h}}) & 0 \\ 0 & 0 & 0 & 1 \end{pmatrix} . \tag{2.77}$$

For a reference particle, $P_X = 0 = P_Y$ and $H/c = \bar{p}_0 = P_S$, which in the boosted frame become transformed into $P_X^* = 0 = P_Y^*$ and $H^*/c = \bar{p}_0^* = \bar{p}_0 \cos(\theta_{\mathrm{h}})$.

The entire transformation from $\mathbf{x}(0)$ to $\mathbf{x}^*(z^*)$ can thus be written as

$$\begin{pmatrix} s^*(z^*) \\ x^*(z^*) \\ z^* \\ y^*(z^*) \end{pmatrix} = \mathbf{A}^{-1}\mathbf{L}\mathbf{A} \begin{pmatrix} s(0) \\ x(0) \\ 0 \\ y(0) \end{pmatrix} = \begin{pmatrix} \sec(\theta_{\mathrm{h}}) & 0 & 0 & 0 \\ \tan(\theta_{\mathrm{h}}) & 1 & 0 & 0 \\ 0 & -\sin(\theta_{\mathrm{h}}) & \cos(\theta_{\mathrm{h}}) & 0 \\ 0 & 0 & 0 & 1 \end{pmatrix} \begin{pmatrix} s(0) \\ x(0) \\ 0 \\ y(0) \end{pmatrix} , \tag{2.78}$$

and

$$\begin{pmatrix} \delta^* \\ p_x^* \\ h^* \\ p_y^* \end{pmatrix} = \frac{\bar{p}_0}{\bar{p}_0^*}\mathbf{B}^{-1}\mathbf{L}\mathbf{B} \begin{pmatrix} \delta \\ p_x \\ h \\ p_y \end{pmatrix} = \begin{pmatrix} 1 & -\tan(\theta_{\mathrm{h}}) & \tan^2(\theta_{\mathrm{h}}) & 0 \\ 0 & \sec(\theta_{\mathrm{h}}) & -\tan(\theta_{\mathrm{h}})\sec(\theta_{\mathrm{h}}) & 0 \\ 0 & 0 & \sec^2(\theta_{\mathrm{h}}) & 0 \\ 0 & 0 & 0 & \sec(\theta_{\mathrm{h}}) \end{pmatrix} \begin{pmatrix} \delta \\ p_x \\ h \\ p_y \end{pmatrix} , \tag{2.79}$$

where the ratio $\bar{p}_0/\bar{p}_0^*$ introduces an additional factor $\sec(\theta_{\mathrm{h}})$. The transformation $\mathbf{L}$ acts on the array $(H/c, P_X, P_S, P_Y)$ and not the array $(H/c - \bar{p}_0, P_X, P_S - \bar{p}_0, P_Y)$ in Eq. (2.74) that is produced by the $\mathbf{B}$ transformation. The additional terms do however cancel, and the matrices displayed here are valid to perform the required transformation to a boosted head-on frame at $z^* = -\sin(\theta_{\mathrm{h}})x(0)$.

The desired coordinates are $\mathbf{x}^*(0^*)$, not $\mathbf{x}^*(z^*)$. An additional transformation is thus needed, taken as the Taylor expansion to first order [30]

$$x_i^*(0^*) = x_i^*(z^*) - \frac{\mathrm{d}x_i^*(0^*)}{\mathrm{d}z^*} z^* = x_i^*(z^*) + \frac{\partial h^*}{\partial p_i^*} \sin(\theta_{\mathrm{h}}) x(0) , \tag{2.80}$$

where the Hamiltonian equation has been used, considering z^* to be equivalent to time scaled by the speed of light [15]. It can also be shown that

$$h^*(p_x^*, p_y^*, \delta^*; \bar{p}_0^*) = h(p_x^*, p_y^*, \delta^*; \bar{p}_0^*) . \tag{2.81}$$

The complete mapping $\mathcal{L}$ from $\mathbf{x}(0)$ to $\mathbf{x}^*(0^*)$ is thus

$$\begin{aligned}
x^* &= x \cdot \left(1 + \frac{\partial h^*}{\partial p_x^*}\sin(\theta_\mathrm{h})\right) + s\tan(\theta_\mathrm{h}) \,, \\
y^* &= y + x\sin(\theta_\mathrm{h})\frac{\partial h^*}{\partial p_y^*} \,, \\
s^* &= \frac{s}{\cos(\theta_\mathrm{h})} + x\sin(\theta_\mathrm{h})\frac{\partial h^*}{\partial \delta^*} \,, \\
p_x^* &= \frac{p_x - \tan(\theta_\mathrm{h})h}{\cos(\theta_\mathrm{h})} \,, \\
p_y^* &= \frac{p_y}{\cos(\theta_\mathrm{h})} \,, \\
\delta^* &= \delta - p_x\tan(\theta_\mathrm{h}) + h\tan^2(\theta_\mathrm{h}) \,.
\end{aligned} \tag{2.82}$$

Pay attention to the combination of terms from both the boosted and the original frame on the right side of these equations. In the ultra-relativistic limit, this mapping is exact.

Based on the mapping $\mathcal{L}$ in Eq. (2.82), one can already predict a few effects of the crossing angle. The beam size can be found from the expression for the variation of independently distributed particles, $\sigma_x^2 = \langle x^2\rangle - \langle x\rangle^2$. All coordinates are independently distributed, meaning that $\langle xs\rangle = \langle x\rangle\langle s\rangle$. Furthermore, all coordinates are distributed with zero mean, $\langle x_i\rangle = 0 = \langle p_i\rangle$. Therefore, $\sigma_x^2 = \langle x^2\rangle$ and only terms proportional to squared values will be nonzero. The derivatives of h^* with respect to p_q^* are proportional to p_q^*. The terms containing squares of the derivatives of h^* are proportional to $\sin^2(\theta_\mathrm{h}) \approx 0$ and are negligible for the relevant angles. This gives the expressions for the effective transverse beam sizes in the boosted frame for a horizontal crossing

$$\begin{aligned}
\sigma_x^* &= \sigma_x \cdot \sqrt{1 + \left(\frac{\sigma_s}{\sigma_x}\tan(\theta_\mathrm{h})\right)} \,, \\
\sigma_y^* &= \sigma_y \,,
\end{aligned} \tag{2.83}$$

where the effective boosted horizontal beam size is divided by the factor S in Eq. (2.28), which explains the luminosity reduction for nonzero crossing angle.

The maximum beam-beam tune shift for head-on collisions was found to be equal to the beam-beam parameter ξ_q in Eq. (2.47). By insertion of the effective head-on beam sizes in Eq. (2.83) into that expression, one gets for a horizontal crossing

$$\begin{aligned}
\eta_{x,h} &= \left|\xi_{x,h}^*\right| = \frac{N r_0 \beta_x^* S^2}{2\pi\gamma\sigma_x(\sigma_x + S\sigma_y)} \,, \\
\eta_{y,h} &= \left|\xi_{y,h}^*\right| = \frac{N r_0 \beta_y^* S}{2\pi\gamma\sigma_y(\sigma_x + S\sigma_y)} \,,
\end{aligned} \tag{2.84}$$

where the subscript h signifies the horizontal crossing angle. Here $\eta_{q,h/v}$ is introduced as the effective beam-beam parameter, compared to the nominal $|\xi_q|$. For a Piwinski angle $\phi_{\mathrm{PIW},x} = 1$, $S = 1/\sqrt{2}$. For round beams, this corresponds to a reduction of the maximum beam-beam tune shift in the horizontal plane as $\eta_{x,h} = 0.59|\xi_x|$, and in the vertical plane as $\eta_{y,h} = 0.83|\xi_x|$. A common crossing scheme in an accelerator is to have two IPs of equal strength $|\xi_q|$, with one horizontal and one vertical crossing. For round beams, this leads to a total tune shift

$$\Delta Q_{q,\mathrm{Tot}} = \left|\xi_{q,h}^* + \xi_{q,v}^*\right| = \left|\xi_\mathrm{Tot}\right| \cdot S \,, \tag{2.85}$$

where $\xi_\mathrm{Tot} = 2\xi$ is the sum of the nominal beam-beam parameters in the two independent IPs.

2.4.2 Transformation back to accelerator coordinates

To find the inverse mapping from the head-on frame to the original frame, one can begin by calculating the inverses of Eq. (2.78) and Eq. (2.79). Physically, the inverse Lorentz transformation, L^{-1}, consists of first boosting in the opposite direction followed by rotating clockwise by an angle θ_h, thus

$$\mathbf{L}^{-1} = \begin{pmatrix} \sec(\theta_\mathrm{h}) & \tan(\theta_\mathrm{h}) & 0 & 0 \\ \sin(\theta_\mathrm{h}) & 1 & -\sin(\theta_\mathrm{h}) & 0 \\ \sin(\theta_\mathrm{h})\tan(\theta_\mathrm{h}) & \tan(\theta_\mathrm{h}) & \cos(\theta_\mathrm{h}) & 0 \\ 0 & 0 & 0 & 1 \end{pmatrix} , \tag{2.86}$$

which can be checked by insertion in $\mathbf{L}^{-1}\mathbf{L} = \mathbf{I}_4$, where $\mathbf{I}_4$ is the 4D unity matrix. Applying the known concepts for matrices $\mathbf{C}$ and $\mathbf{D}$ that

$$(\mathbf{CD})^{-1} = \mathbf{D}^{-1}\mathbf{C}^{-1} , \tag{2.87}$$

$$(\mathbf{C}^{-1})^{-1} = \mathbf{C} , \tag{2.88}$$

one finds the inverse of the transformation in Eq. (2.78) to be

$$\begin{pmatrix} s(0) \\ x(0) \\ 0 \\ y(0) \end{pmatrix} = \mathbf{A}^{-1}\mathbf{L}^{-1}\mathbf{A} \begin{pmatrix} s^*(z^*) \\ x^*(z^*) \\ z^* \\ y^*(z^*) \end{pmatrix} = \begin{pmatrix} \cos(\theta_\mathrm{h}) & 0 & 0 & 0 \\ -\sin(\theta_\mathrm{h}) & 1 & 0 & 0 \\ -\sin(\theta_\mathrm{h})\tan(\theta_\mathrm{h}) & \tan(\theta_\mathrm{h}) & \sec(\theta_\mathrm{h}) & 0 \\ 0 & 0 & 0 & 1 \end{pmatrix} \begin{pmatrix} s^*(z^*) \\ x^*(z^*) \\ z^* \\ y^*(z^*) \end{pmatrix} , \tag{2.89}$$

and the inverse of the transformation in Eq. (2.79) to be

$$\begin{pmatrix} \delta \\ p_x \\ h \\ p_y \end{pmatrix} = \frac{\bar{p}_0^*}{\bar{p}_0}\mathbf{B}^{-1}\mathbf{L}^{-1}\mathbf{B} \begin{pmatrix} \delta^* \\ p_x^* \\ h^* \\ p_y^* \end{pmatrix} = \begin{pmatrix} 1 & \sin(\theta_\mathrm{h}) & 0 & 0 \\ 0 & \cos(\theta_\mathrm{h}) & \sin(\theta_\mathrm{h})\cos(\theta_\mathrm{h}) & 0 \\ 0 & 0 & \cos^2(\theta_\mathrm{h}) & 0 \\ 0 & 0 & 0 & \cos(\theta_\mathrm{h}) \end{pmatrix} \begin{pmatrix} \delta^* \\ p_x^* \\ h^* \\ p_y^* \end{pmatrix} . \tag{2.90}$$

The entire transformation is multiplied by a factor $\bar{p}_0^*/\bar{p}_0 = \cos(\theta_\mathrm{h})$. Reapplying Eq. (2.80) on the array elements, one gets the complete mapping $\mathcal{L}^{-1}$ back from $\mathbf{x}^*(0^*)$ to $\mathbf{x}(0)$

$$\begin{aligned} x &= \frac{x^* - s^*\sin(\theta_\mathrm{h})}{1 + \sin(\theta_\mathrm{h})\frac{\partial h^*}{\partial \delta^*} + \sin^2(\theta_\mathrm{h})\frac{\partial h^*}{\partial p_x^*}} , \\ y &= y - x\sin(\theta_\mathrm{h})\frac{\partial h^*}{\partial p_y^*} , \\ s &= \left(s^* - x\sin(\theta_\mathrm{h})\frac{\partial h^*}{\partial \delta^*}\right)\cos(\theta_\mathrm{h}) , \\ p_x &= (p_x^* + \sin(\theta_\mathrm{h})h^*)\cos(\theta_\mathrm{h}) , \\ p_y &= p_y^*\cos(\theta_\mathrm{h}) , \\ \delta &= \delta^* + p_x^*\sin(\theta_\mathrm{h}) . \end{aligned} \tag{2.91}$$

Pay attention to the fact that x has been defined from x^*, while y and s has been defined using the more compact form x.

2.4.3 Synchro-beam mapping

By applying the transformation $\mathcal{L}$ in Sec. 2.4.1, the opposing beams may be described in boosted coordinate systems with parallel longitudinal axes. It is however obvious from Fig 2.14 that the interaction does change as a function of s^*. Therefore, the motion through the IP must be integrated. The method that will be presented in this section performs this integration by calculating the kick from a finite number of slices, N_S, separated by empty drift spaces [31]. Each slice is made to consist of equally many particles N/N_S, located at its centre of mass $s_{\Sigma,j}$, where $j = \{1, ..., N_\mathrm{S}\}$ is the slice number. The subscript Σ denotes that this is for the strong beam. For a Gaussian distribution, the centres of mass are

$$s_{\Sigma,j} = \frac{N_\mathrm{S}}{\sqrt{2\pi}} \left(\exp\left[-\frac{1}{2} \left(\mathrm{pp}\left[\frac{j}{N_\mathrm{S}} \right] \right)^2 \right] - \exp\left[-\frac{1}{2} \left(\mathrm{pp}\left[\frac{j-1}{N_\mathrm{S}} \right] \right)^2 \right] \right) , \tag{2.92}$$

where pp is the percentile point function, otherwise known as the inverse cumulative density function for a Gaussian distribution. $\mathrm{pp}[x]$ gives the border for when the cumulative density below the border is equal to x, i.e.

$$x = \frac{1}{\sqrt{2\pi}\sigma_u} \int_{-\infty}^{\mathrm{pp}[x]} \exp\left[-\frac{u^2}{2\sigma_u^2} \right] \mathrm{d}u \ . \tag{2.93}$$

The longitudinal position of the slices, $s_{\Sigma,j}$, are calculated such that the particles in the weak beam first interact with slice $j = 1$.

The coordinates for the strong beam centred at $z^* = 0$ are denoted by a † as $\mathbf{x}^*_\Sigma(z^* = 0) = \mathbf{x}^\dagger$. Due to the assumed Gaussian shape, the necessary values are the average positions $\langle x^\dagger \rangle$, denoted as $x_i^\dagger$ in the following, and the variations of each coordinate, denoted as $(\sigma^\dagger)^2 = \Sigma^\dagger$. The position of the particles in the strong beam in its boosted frame can also be found by Eq. (2.82), because its coordinate system is left-handed due to the flipping of $s^*_\Sigma = -s^*$. The effective position of the particles in the slice located at $s_{\Sigma,j}$ is for a horizontal crossing

$$\begin{aligned} x^\dagger &= s_{\Sigma,j} \tan(\theta_\mathrm{h}) \ , \\ y^\dagger &= 0 \ , \\ s^\dagger &= \frac{s_{\Sigma,j}}{\cos(\theta_\mathrm{h})} \ , \end{aligned} \tag{2.94}$$

and all the momentums average to zero. The variations of the coordinates are to first order in the dynamical variables at $z^* = 0$

$$\begin{aligned} \Sigma_x^\dagger &= \Sigma_x \ , \\ \Sigma_y^\dagger &= \Sigma_y \ , \\ \Sigma_s^\dagger &= \frac{\Sigma_s}{\cos^2(\theta_\mathrm{h})} \ , \\ \Sigma_{p_x}^\dagger &= \frac{\Sigma_{p_x}}{\cos^2(\theta_\mathrm{h})} \ , \\ \Sigma_{p_y}^\dagger &= \frac{\Sigma_{p_y}}{\cos^2(\theta_\mathrm{h})} \ , \\ \Sigma_\delta^\dagger &= \Sigma_\delta \ . \end{aligned} \tag{2.95}$$

The interaction between the slice at $s^\dagger$ and the particle at s^*, occurs at the collision point (CP) at position

$$Z = \frac{s^* - s^\dagger}{2} \ , \tag{2.96}$$

along the z^*-axis. The coordinates of the particles in the weak beam and the slices in the strong beam must be transported to the CP. To achieve this, assume a drift space from $z^* = 0$ to $z^* = Z$, giving

$$\begin{aligned} x_q^*(Z) &= x_q^*(0) + p_q^*(0) \cdot Z \ , \\ p_q^*(Z) &= p_q^*(0) \ , \end{aligned} \tag{2.97}$$

shifting the position, while leaving the momentum unchanged. The transverse distance between the centre of the slice, $x_q^\dagger$, and the particle at $x_q^*(Z)$ is therefore

$$\begin{aligned} X(Z) &= x^*(0) + p_x^*(0) \cdot Z - x^\dagger \ , \\ Y(Z) &= y^*(0) + p_y^*(0) \cdot Z - y^\dagger \ , \end{aligned} \tag{2.98}$$

where $y^\dagger = 0$ for horizontal crossings. Using again the fact that $\langle xs \rangle = 0$ for independently distributed particles around a zero mean, gives the change of the transverse slice sizes of the strong beam to be

$$\begin{aligned} \Sigma_q^\dagger(Z) &= \Sigma_q^\dagger(0) + \Sigma_{p_q}^\dagger(0) \cdot Z^2 \ , \\ \Sigma_{p_q}^\dagger(Z) &= \Sigma_{p_q}^\dagger(0) \ , \end{aligned} \tag{2.99}$$

which is similar to the dependence expected from the hourglass effect in Eq. (2.1).

The interaction between a particle of charge q and a slice containing N/N_S particles, can be calculated from the Hamiltonian [31]

$$H_{BB} = qU(X, Y, \Sigma_x^\dagger, \Sigma_y^\dagger; Z)\partial(Z), \tag{2.100}$$

where the potential felt by the particle, U, is defined per particle in the slice as

$$U(X, Y, \Sigma_x^\dagger, \Sigma_y^\dagger; Z) = \frac{Nr_0}{qN_\mathrm{S}\gamma} \int_0^\infty \frac{\exp\left[-\frac{X(Z)^2}{2\Sigma_x^\dagger(Z)+u} - \frac{Y(Z)^2}{2\Sigma_y^\dagger(Z)+u}\right]}{\sqrt{2\Sigma_x^\dagger(Z)+u}\sqrt{2\Sigma_y^\dagger(Z)+u}} \, \mathrm{d}u \ . \tag{2.101}$$

The transverse electric field from this potential can be calculated as

$$\mathbf{E} = -\boldsymbol{\nabla} U \ , \tag{2.102}$$

whereupon the kick on the momentum can be calculated.

The explicit form of the transfer map from a single slice can, through another shift of canonical variables [30], be found to be

$$\begin{aligned} \Delta x^* &= -Z \cdot f_x(X, Y; Z) \ , \\ \Delta p_x^* &= f_x(X, Y; Z) \ , \\ \Delta y^* &= -Z \cdot f_y(X, Y; Z) \ , \\ \Delta p_y^* &= f_y(X, Y; Z) \ , \\ \Delta s^* &= 0 \ , \\ \Delta \delta^* &= \frac{1}{2} f_x(X, Y; Z) \left(p_x^* + \frac{1}{2} f_x(X, Y; Z) \right) \\ &\quad + \frac{1}{2} f_y(X, Y; Z) \left(p_y^* + \frac{1}{2} f_y(X, Y; Z) \right) + g(X, Y; Z) \ , \end{aligned} \tag{2.103}$$

where f_x, f_y and g depend on the distribution. The change in x^* and y^* can, when $Z < 0$, be understood to be the shift that Δp_q^* would have caused before the particle reaches $z^* = 0$. This expression is aimed at pp-colliders and not e^+e^--colliders, making it different from the original expression [31].

For round beams, $f_x(X, Y; Z)$ and $f_y(X, Y; Z)$ are calculated by inserting $(X, Y, \sigma_x^\dagger, \sigma_y^\dagger, N/N_\mathrm{S})$ for $(x, y, \sigma_x, \sigma_y, N)$ in Eq. (2.37), where $\Delta x_q'$ is equivalent to Δp_q in this section. g can, using that $\Sigma_x^\dagger = \Sigma_y^\dagger = \Sigma_r^\dagger$ and $\Sigma_{p_x}^\dagger = \Sigma_{p_y}^\dagger = \Sigma_{p_r}^\dagger$, be calculated to be

$$g = \frac{Z\Sigma_{p_r}^\dagger}{\Sigma_r} \cdot \frac{Nr_0}{N_\mathrm{S}\gamma} \exp\left[-\frac{X(Z)^2 + Y(Z)^2}{2\Sigma_r(Z)}\right]. \tag{2.104}$$

For flat beams, $f_x(X, Y; Z)$ and $f_y(X, Y; Z)$ are calculated by inserting $(X, Y, \sigma_x^\dagger, \sigma_y^\dagger, N/N_\mathrm{S})$ for $(x, y, \sigma_x, \sigma_y, N)$ in Eq. (2.41), assuming that $\sigma_x^\dagger > \sigma_y^\dagger$. g can for this situation be calculated to be

$$\begin{aligned} g = &\frac{Z\Sigma_{p_x}}{2(\Sigma_x^\dagger - \Sigma_y^\dagger)} \left(X f_x + Y f_y + \frac{2Nr_0}{N_\mathrm{S}\gamma} \left(\frac{\sigma_y^\dagger}{\sigma_x^\dagger} \exp\left[-\frac{X}{2\Sigma_x} - \frac{Y}{2\Sigma_y}\right] - 1 \right) \right) \Bigg|_Z \\ &- \frac{Z\Sigma_{p_y}}{2(\Sigma_x^\dagger - \Sigma_y^\dagger)} \left(X f_x + Y f_y + \frac{2Nr_0}{N_\mathrm{S}\gamma} \left(\frac{\sigma_x^\dagger}{\sigma_y^\dagger} \exp\left[-\frac{X}{2\Sigma_x} - \frac{Y}{2\Sigma_y}\right] - 1 \right) \right) \Bigg|_Z , \end{aligned} \tag{2.105}$$

where the subscript Z at the far right denotes that all values are to be evaluated at Z.

From what has been presented so far, it is obvious that the 6D beam-beam interaction causes mixing between the longitudinal and transverse planes. The hourglass effect makes the interaction dependent on where the particles are located longitudinally, s. The interaction is however still symmetric with respect to x and y for zero crossing angle. Therefore, one can expect that the hourglass effect causes synchro-betatron resonances of nonzero m in Eq. (2.54), but the odd resonances should still remain zero, as found in Eq. (2.58). A nonzero crossing angle will however make the interaction asymmetrical with respect to x and y, and odd resonances induced by the crossing angle may become important to understand the dynamics of the beam.

2.5 Beam Evolution

The goal of a collider is to maximise the integrated luminosity over time. The luminosity at a certain time is given by Eq. (2.27), and it will decrease if either the bunches lose particles or the bunch emittances grow. If there would be only conservative and differentiable forces acting on the bunches, the beam could in principle remain unaltered forever. In real colliders, this is not the case. The strongly nonlinear and resonance driving beam-beam interactions have already been presented in detail. Some additional concepts related to the evolution of the beam quality will be presented in this section.

There are multiple sources of particle losses from the bunches. One unavoidable source of particle losses is the luminosity burn-off. These particles are lost because they collide at the IPs, i.e. what the collider was built for. The other main source of beam losses is particles that drift to large transverse amplitudes, whereupon they collide with the collimation system of the accelerator. The collimators are put in the machine to shield the magnets and the rest of the machine from the large quantity of energy that is stored in the beam [33]. There are multiple causes for particles to drift to such large amplitudes, including the beam-beam interaction and nonlinearities of the lattice.

Intra-beam scattering (IBS) is small angle Coulomb scattering between particles in the same bunch. This effect is therefore stronger for denser beams. Coulomb collisions can be considered

approximately instantaneous. Therefore, it is valid to assume that only the momentum is directly affected by the IBS, while the position is kept unchanged, as for the beam-beam interaction. There is much theory on the subject, see for instance [34]. The effect of the IBS is in many cases well approximated by a linear increase of the beam emittance with time. It is thus quite similar to regular diffusion, which is discussed in App. A.

A charged particle moving through a magnetic field emits radiation due to the acceleration transverse to the direction of travel. In a circular accelerator, this emission is continuously depriving the beam of energy due to the bending in the arcs. This synchrotron radiation leads to an exponential damping of the emittances. The radiation is however not smooth. On the quantum level, this radiation is emitted as discrete photons, leading to so-called quantum excitations [35]. The synchrotron radiation of energy causes damping of the emittances, while the quantum excitation causes growth. These opposing effects cause the emittance to evolve to an equilibrium emittance. The energy loss scales like $P \propto (E/m)^4$. For e^+e^--colliders, the damping is strong, and the emittance damping time is in the order of ms. A pp-collider can maintain collisions at the same energy E with energy losses reduced by a factor $(m_e/m_p)^4$. That is why pp-colliders as the LHC and the FCC-hh are preferred to reach higher energies. The emittance damping is negligible in the LHC, with a damping time in the order of $24\,\mathrm{h}$, whereas the damping time in the FCC-hh will be in the order of $1\,\mathrm{h}$ due to the higher energy. In both cases the effect of the quantum excitation is small compared to the IBS. In the FCC-hh, the reduction of the emittance can lead to configurations where the effect of quantum excitation is no longer negligible [36]. Since the number of photons emitted per turn is high, the integrated effect in one turn can also be modelled as a regular diffusion mechanism driven by a Gaussian white noise.

Nonlinear diffusion mechanisms and stability of generic Hamiltonian systems is a wide field of theory. The KAM theorem states that for systems perturbed away from integrable ones, there remain invariant surfaces for most initial conditions [14]. Thus, although a motion is stochastic due to resonances as described in Sec. 2.3, it remains constrained by KAM curves. Motion in a 2D phase space can thus be found to be confined, and a resonance in either the horizontal or vertical plane is not sufficient to produce diffusion. For systems with three or more dof, the KAM curves can however not stop the particles and there is a motion along stochastic layers. Thus, there can be a lack of conservation of action for slightly perturbed systems of more than 2 dof. This is referred to as Arnold diffusion. The diffusion is larger when multiple dof are mixed. In particular, it will be found that even though a single resonance may not affect the beam quality significantly, overlapping of resonances can cause great diffusion and losses.

Chapter 3

NUMERICAL MODEL

CABIN (Cuda-Accelerated Beam-beam INteraction) is a code developed to track incoherent particles of a single bunch through two interaction points, separated by two individual stretches of the magnetic lattice, as visualised in Fig. 3.1. In an ideal setting, a simulation would be an exact replication of the physics. That includes the true fields of all magnets around the lattice, noise from many different sources, Coulomb scattering from every particle in the opposing beam, etc. This is not within reach numerically. Assumptions have to be made, and validity of these have to be checked. In CABIN, the beam-beam interaction can be set to be either 4D or 6D, and to be caused by either a round or a flat, fixed opposing bunch in the weak-strong model. Instead of modelling how the IBS and the quantum excitation works exactly, their effect is modelled as a Gaussian white noise, affecting each particle independently. The motion through all the magnets around the lattice has been modelled as a linear transfer matrix, which is correct to first order. The phase advances vary due to a linear chromaticity. The collimation is done only once per turn around the ring, and counts every particle beyond an elliptical limit in (x, y) as lost. This chapter explains how the physics, which have been explained in Ch. 2, is implemented in CABIN. The code is available online through Gitlab [37].

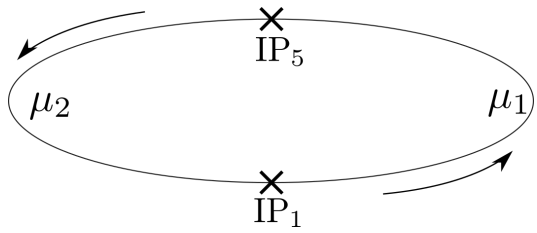

Figure 3.1: Visualisation of what can be modelled by CABIN. Two interaction points where the weak and strong beams interact. Two stretches of beam pipe with independent phase advances affected by chromaticity.

The goal of CABIN is to study the effect of strong beam-beam interactions on the quality of the beam in circular hadron colliders. The structure is written in Python. The computation heavy tracking is performed using PyCUDA, putting the parallel infrastructure of graphic cards to good use. This makes it possible to track sufficiently many particles to represent the distribution of the beam, and thereby study the evolution of bunch emittance and intensity over many turns. A timing study on the improvement by using PyCUDA is presented in App. C.1. Important parameters at the

high-luminosity IPs in the model are given in Table 3.1, alongside the equivalent parameters in the LHC (design) [3], LHC (2017) [29], HL-LHC [38] and FCC-hh for bunches at $25\,\mathrm{ns}$ spacing [5]. The max beam-beam tune shift for FCC-hh is achieved after the emittance has decreased due to synchrotron radiation. The values can be set for each simulation separately in CABIN. The default values are given in the table, and will be used unless stated otherwise. The intensity of the strong bunch is not set directly, but depends on the beam-beam parameter and normalised emittance as given in Eq. (2.46). The max tune shift depends on the beam-beam parameter and the configuration. The influence of the relativistic γ is solely as a ratio between the emittance and the normalised emittance, in agreement with Eq. (2.10).

Table 3.1: Values for parameters in present and future circular colliders, in addition to CABIN.

Parameter	Symbol	LHC (design)	LHC (2017)	HL-LHC	FCC-hh	CABIN [4]
Particles per bunch	$N\ [10^{11}]$	1.15	1.2	2.2	1	$N(\xi)$
Number of bunches	$n_b\ [1]$	2808	2556	2738	10600	1
rms bunch length	$\sigma_s\ [\mathrm{cm}]$	7.55	8.2	7.55	8	8
rms energy spread	$\sigma_\delta\ [10^{-4}]$	1.1	1.2	1.1	~ 1	1
Normalised emittance	$\epsilon_n\ [\mu\mathrm{m}]$	3.75	2.5	2.5	2.2	3
IP beta function [1]	$\beta_q^*\ [\mathrm{m}]$	0.55	0.4	0.15	0.3	0.4
Crossing angle	$\theta_{\mathrm{xing}}\ [\mu\mathrm{rad}]$	285	300	590 [2]	175 [2]	0
Piwinski angle	$\phi_{\mathrm{PIW}}\ [1]$	0.65	1.02	3.14 [2]	1.99 [2]	0
Proton energy	$E_p\ [\mathrm{TeV}]$	7	6.5	7	50	6.5
Gamma factor	$\gamma\ [1]$	7460.5	6927.6	7460.5	53289	6927.6
Max tune shift [3]	$\Delta Q_{\mathrm{Tot}}\ [1]$	0.0063	0.0082	0.021	0.03	$f(\xi)$
Horizontal tune	$Q_x\ [1]$	0.31	0.31	0.31	0.31	0.31
Vertical tune	$Q_y\ [1]$	0.32	0.32	0.32	0.32	0.324
Revolution frequency	$f_{\mathrm{rev}}\ [\mathrm{kHz}]$	11.245	11.245	11.245	3.067	11.245

[1] At the IPs of minimum beta function.
[2] May be countered by use of crab cavities.
[3] Assumed collisions in two IPs, zero Piwinski angle in HL-LHC and FCC-hh.
[4] Set for each simulation separately. These are the default values.

3.1 Normalised Coordinates

Calculations can be done using physical quantities as the position and momentum of particles in the beam. However, doing calculations on positions in the range of $\mu\mathrm{m}$, while energies are given in TeV, has certain disadvantages. First of all, calculations on values of different orders increase numerical noise. Second of all, it is difficult to discuss and compare values acquired in different settings. A set of normalised coordinates with reduced units has been applied in CABIN. In this section a hat refers to normalised values, as $\hat{x}$ in comparison to x.

A normalisation has already been done by dividing the mechanical momentum of the particles by the reference momentum, $\bar{p}_0$. For reasons that will soon be clear, the transverse phase space coordinates have been transformed further into

$$\hat{x}_q = \frac{x_q}{\sigma_q} \qquad , \qquad \hat{p}_q = \frac{1}{\sigma_q}\left(\alpha_q x_q + \beta_q x_q'\right) \ , \tag{3.1}$$

where σ_q is the initial beam size in either transverse plane of the weak beam. The transverse actions change accordingly to

$$\hat{J}_q = \frac{1}{2}\left(\hat{x}_q^2 + \hat{p}_q^2\right) = \frac{J_q}{\epsilon_{q,0}}\,, \tag{3.2}$$

where $\epsilon_{q,0}$ is the initial transverse beam emittance as defined in Eq. (2.9). For Gaussian beams, this leads to $\hat{\epsilon}_{q,0} = 2$. In the longitudinal plane,

$$\hat{s} = \frac{s}{\sigma_s} \qquad , \qquad \hat{\delta} = \frac{\delta}{\sigma_\delta}\,. \tag{3.3}$$

In the old phase space coordinates, (x_i, x_i'), the transfer due to the lattice was given by Eq. (2.15) and Eq. (2.18). In the new coordinates, $(\hat{x}_i, \hat{p}_i)$, the transfer due to the lattice from IP1 to IP5 is only a rotation

$$\begin{bmatrix}\hat{x}_i\\ \hat{p}_i\end{bmatrix}_{\text{IP5}} = \hat{\mathbf{R}}_i \begin{bmatrix}\hat{x}_i\\ \hat{p}_i\end{bmatrix}_{\text{IP1}} \qquad , \qquad \hat{\mathbf{R}}_i = \begin{bmatrix}\cos(\mu_{1,i}) & \sin(\mu_{1,i})\\ -\sin(\mu_{1,i}) & \cos(\mu_{1,i})\end{bmatrix}\,, \tag{3.4}$$

where $\mu_{1,i}$ is the intermediate phase advance in the three phase space planes through that part of the lattice, and μ_q is dependent on δ due to Q', as given by Eq. (2.20). Going from IP5 to IP1 is done equivalently using $\mu_{2,i}$ to complete the turn. The zero chromaticity phase advance is divided in any way desirable with the restraint $\mu_{1,q} + \mu_{2,q} = \mu_q = 2\pi Q_q$, where Q_q is the transverse tune in that plane. Due to the separation of the lattice in these two intermediate sections, the chromaticity is divided evenly over the two sections as $Q_1' = Q_2' = Q'/2$, and so is the synchrotron tune, Q_s. The chromaticity is kept equal in the two transverse planes, $Q_x' = Q_y'$. The figure traced out in $(\hat{x}, \hat{p}_x)$-space due to this rotation is in the normalised coordinates a circle of radius or amplitude

$$\hat{A}_x = \sqrt{\hat{x}^2 + \hat{p}_x^2}\,, \tag{3.5}$$

in contrast to the ellipse in Fig. 2.3. Deviations from these circles in the Poincaré sections are easier to detect visually.

The IBS is a complex interaction between charged particles, which has an effect similar to a diffusion of the particle momentum with constant diffusivity. The quantum excitations can happen at any time, inducing a random deflection of a single particle's momentum. Both effects have the same result in many cases, an approximately linear growth of beam emittance. This can be approximated by a random walk of the momentum. The synchrotron damping has so far not been taken into account in CABIN.

Consider one normally distributed kick per turn, κ_q, with rms amplitude $\hat{\Delta} = 1 \times 10^{-4}$, on the normalised momentum $\hat{p}_q$

$$\hat{p}_q = \hat{p}_q + \kappa_q\,, \tag{3.6}$$

as discussed in App. A. Applying Eq. (A.4), the diffusivity per turn is $\hat{D} = 5 \times 10^{-9}$. In result, the normalised beam emittance, $\hat{\epsilon}_q$, increases with 1×10^{-8} /turn . The LHC has a rotation frequency of about 11 kHz, giving a doubling time with this noise of $\tau_{\text{LHC}} = 5\,\text{h}$. For the FCC, the frequency will be about 3 kHz, giving a doubling time with this noise of $\tau_{\text{FCC}} = 19\,\text{h}$. These doubling times can easily be changed by changing the kicks' rms amplitude. The noise will for most presented results either be kept at this value or set to zero. This improves the comparability of the effect of the beam-beam interaction in different situations. However, it creates the issue that the growth in the non-normalised coordinates is smaller for a denser beam, opposite to the increased effect of IBS on denser bunches. As most simulations are done with the same emittance, this modelling has been found sufficiently accurate for the purpose of CABIN, which is to understand the effect of the head-on beam-beam interaction.

3.2 Beam-Beam Interaction

In the original phase space coordinates, the kick due to the beam-beam interaction between round beams of equal size was given by Eq. (2.37). In normalised coordinates this is

$$\Delta\hat{\mathbf{p}} = \frac{\beta_q^*}{\sigma_q}\Delta\mathbf{r}' = -8\pi\xi\left(1-\exp\left[-\frac{\hat{r}^2}{2}\right]\right)\frac{\hat{\mathbf{r}}}{\hat{r}^2}\,. \tag{3.7}$$

The kick is only dependent on the beam-beam parameter ξ and the position of the particle. The maximum design beam-beam tune shift of the FCC-hh is 0.03 for zero crossing angle [5]. When divided over 2 IPs, this gives per IP, $\xi_{\text{FCC}} = 0.015$.

The kicks from flat beams in Eq. (2.41) and the transformation to and from the boosted frame in Eq. (2.82) and Eq. (2.91), are strongly dependent on the non-normalised coordinates. Therefore, the beam-beam interactions for these scenarios are performed on the original coordinates $\mathbf{x}$, not $\hat{\mathbf{x}}$. To achieve this, all coordinates $\hat{\mathbf{x}}$ are scaled by their standard deviations σ before the beam-beam interactions, and divided by them afterwards. The Faddeeva functions in the flat beam-beam interaction is calculated using an existing CUDA-implementation [39]. Benchmarking of the implementation of the 6D beam-beam effect in CABIN is presented in App. B.1.

The beam-beam interaction is the most time-consuming effect modelled in CABIN. A profiling study on the beam-beam implementation is presented in App. C.2. To summarise the findings, the 4D round beam-beam implementation is comparable in time spending to the lattice and the noise. The other implementations of the beam-beam interaction consumes in general more than 95% of the computation time of the simulations. The flat beam kick is ~ 35 times slower than the round beam kick per slice. This is because the Faddeeva function, $\mathrm{w}[x+\mathrm{i}y]$, is much slower than the exponential function, $\exp[x]$. The overhead, due to the boost $\mathcal{L}$ in Eq. (2.82) among other calculations, takes approximately as much time as the kick from $N_{\mathrm{S}} = 6$ slices for round beams, while the overhead is much faster than a single slice for flat beams. The time per slice for either round or flat beams is naturally similar to the equivalent 4D implementations.

As the beam-beam interaction is the most time-consuming effect implemented, there is effectively a constraint on how many slices, N_{S}, that can be used in the 6D simulations. Therefore, it was important to find out how fast the implementation converges. How this was done is presented in App. B.2. There it was found that the number of slices, N_{S}, required to achieve a certain tolerance on the kicks, depends on the configuration that is being simulated. For a small crossing angle, θ_{xing}, and a negligible hourglass effect, $\sigma_s/\beta_q^* \ll 1$, the convergence is fast and a single slice may be sufficient. The 4D model may then be applied to achieve the correct behaviour. The required number of slices grows without bound as θ_{xing} and σ_s/β_q^* increase. Therefore, the code finds for each simulation the required number of slices to achieve a certain tolerance.

3.3 Macroparticle Distributions

The number of particles per bunch, N, in circular colliders like the LHC, is in the order of 10^{11}. In CABIN, each particle is tracked in 6 dimensions, at double precision. A single state of a single bunch of this magnitude would require $4.8\,\mathrm{TB}$ of memory. Furthermore, computation time increases in general linearly with N for incoherent particle simulations, ignoring overhead of initialising the simulations. Such a simulation would not be feasible. Instead one models a smaller number of macroparticles, N_{mp}, and attempts extrapolating to the behaviour of the entire bunch. As the goal of this project has been to track the evolution of the beam quality, it is quite important that the smaller number of macroparticles still manage to represent well a Gaussian distribution, both at low transverse amplitudes in the core, and at high transverse amplitudes in the tail. It has been required

that the bunch can represent the distribution up to 6σ. The σ's in this section refer to the weak beam. Different macroparticle distributions are studied in this section.

Multiple initial conditions (IC) for distributing the macroparticles have been attempted. These include a Gaussian distribution, a combined hollow and limited Gaussian distribution, a 6D grid, a uniform distribution and a regionally uniform distribution. Depending on the distribution type, the N_{mp} macroparticles have either been assigned the same weight, N/N_{mp}, or a special weighting based on its position, to represent the N actual particles. The distributions have been compared on how well they fill 6D phase space evenly through histograms of each coordinate separately, of which only the x coordinate will be presented here, and how well the sum of the square of the coordinates fits to the χ^2_6 distribution. The chi-squared distribution is defined as

$$\chi^2_k = \sum_{j=1}^{k} N_j^2 \,, \tag{3.8}$$

where N_j are independently normally distributed variables, as the components of $(\hat{x}, \hat{p}_x, \hat{y}, \hat{p}_y, \hat{s}, \hat{\delta})$. The normalised 6D radius of a particle will be referred to as

$$\chi_6 = \sqrt{\chi^2_6} = \sqrt{\hat{x}^2 + \hat{p}_x^2 + \hat{y}^2 + \hat{p}_y^2 + \hat{s}^2 + \hat{\delta}^2} \,. \tag{3.9}$$

The convergence of the emittance growth rate and the beam loss rate calculations with N_{mp} will be tested for the Gaussian and the regionally uniform distributions, when these measurements are introduced in Sec. 3.4.

The test of a Gaussian distribution of $N_{\text{mp}} = 1 \times 10^5$ macroparticles is visualised in Fig. 3.2. This distribution is most equal to how the particles are distributed in a true bunch, although each macroparticle is weighted equally to represent N/N_{mp} real particles. It is however difficult to represent 10^{11} particles by 10^5 macroparticles. The core is modelled well, as seen from the leftmost subplot, and this distribution would be well apt to measure emittance growth. It is however not able to represent the tail accurately, as detailed in the log-scaled plots, and it does not model the losses of the bunch accurately.

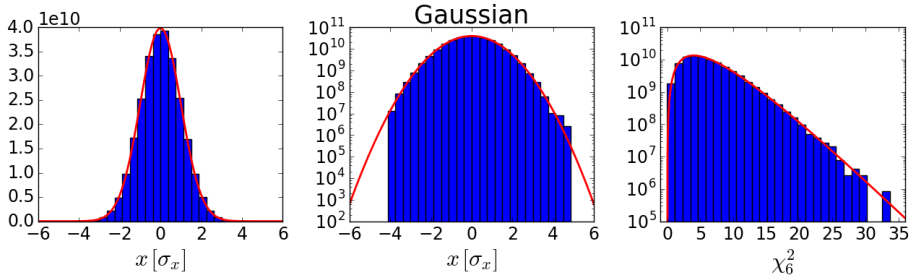

Figure 3.2: Comparison of the Gaussian initial distribution of $N_{\text{mp}} = 1 \times 10^5$ macroparticles, with actual Gaussian and χ^2_6 distributions. The sum of the weight of all particles is $N = 1 \times 10^{11}$. The first plot from the left displays a histogram of x. The second plot displays the same histogram of x, but with a log-scaled y-axis. The last plot displays a histogram of χ^2_6.

In the hollow Gaussian distribution, one half of the particles have been distributed normally below 4σ in the 4D transverse phase space, and the second half have been distributed normally, requiring that they are above 4σ in the 4D transverse phase space [40]. The longitudinal coordinates have been distributed as in the regular Gaussian distribution. This has been done to achieve a better

representation of the tail. The N_{reg} macroparticles in each region separately are weighted equally, but the weighting is different between the different regions. Denoting the cumulative density function for the χ^2_4 distribution as cdf, the weight of all particles in a given region is

$$W_{\text{reg}} = \left(\text{cdf}[\chi^2_{4,\text{max}}] - \text{cdf}[\chi^2_{4,\text{min}}]\right) \cdot \frac{N}{N_{\text{reg}}} \,, \tag{3.10}$$

where the limits on the 4D normalised radius are as mentioned above, $\{0, 4, \infty\}$. The test of this hollow Gaussian distribution of $N_{\text{mp}} = 1 \times 10^5$ macroparticles is visualised in Fig. 3.3. The core is still modelled well, as seen from the leftmost subplot, and this distribution would also be well apt to measure emittance growth. The tail is better represented than by the regular Gaussian distribution, as seen by the χ^2_6 plot, but it is still less accurate than required for correct modelling of the beam losses.

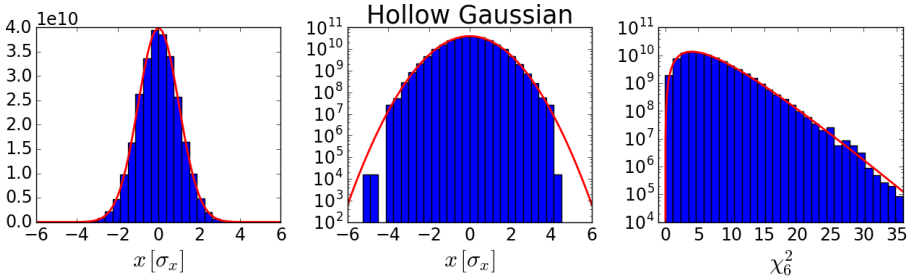

Figure 3.3: Comparison of the hollow Gaussian initial distribution of $N_{\text{mp}} = 1 \times 10^5$ macroparticles, with actual Gaussian and χ^2_6 distributions. The sum of the weight of all particles is $N = 1 \times 10^{11}$. The first plot from the left displays a histogram of x. The second plot displays the same histogram of x, but with a log-scaled y-axis. The last plot displays a histogram of χ^2_6.

In the 6D grid, the particles are distributed equally every time, not dependent on random distributions. The particles are distributed linearly in each coordinate, whereupon these are meshed together in a grid. If the 6th root of N_{mp} is not an integer, this value is rounded up to the closest integer, whereupon the particles of largest normalised 6D amplitude in the grid will be removed. Macroparticle j is weighted individually based on its coordinates as

$$W_j \propto \exp\left[-\frac{\chi^2_6}{2}\right] , \tag{3.11}$$

whereupon the weights are normalised to give a total weight of N. The test of this 6D grid consisting of $N_{\text{mp}} = 1 \times 10^5$ macroparticles is visualised in Fig. 3.4. As visible from all subplots, this distribution does manage to represent particles in the tail, and a loss rate may be found. The distribution is however far from smooth, causing multiple problems. First of all, this distribution will not correctly measure the effect of the highly amplitude dependent resonances. Some will be weighted too strongly, while others will not be taken into account. Second of all, the change of this distribution with time will misrepresent the actual behaviour as the initial peaks will diffuse to neighbouring areas. The grid works well for lower dimensions, and a 2D grid in (x, y) space is commonly used to perform frequency analysis, as will be explained in Sec. 3.5.

The uniform distribution is made by uniformly distributing each coordinate separately to a maximum amplitude of 6σ, followed by demanding that $\chi_6 \leq 6$. The individual particles are then weighted by Eq. (3.11), making each macroparticle in the core represent more real particles than the macroparticles in the tail. The test of this 6D grid of $N_{\text{mp}} = 1 \times 10^5$ macroparticles is visualised in Fig. 3.5. The tail is much better modelled than with the previous distributions, as seen

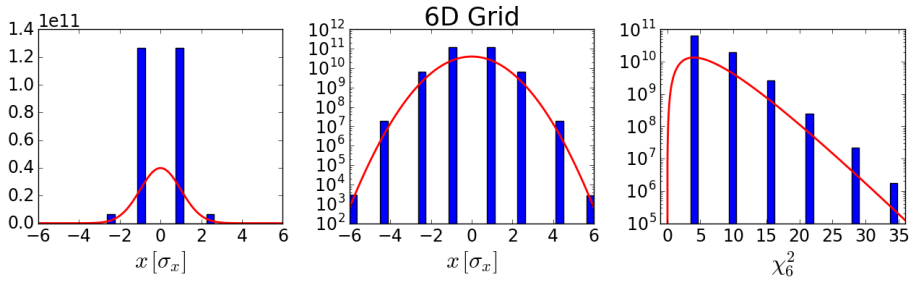

Figure 3.4: Comparison of the 6D grid initial distribution of $N_{\text{mp}} = 1 \times 10^5$ macroparticles, with actual Gaussian and χ_6^2 distributions. The sum of the weight of all particles is $N = 1 \times 10^{11}$. The first plot from the left displays a histogram of x. The second plot displays the same histogram of x, but with a log-scaled y-axis. The last plot displays a histogram of χ_6^2.

by the log-scaled plots. This distribution will do well in modelling the beam losses. The core is however not modelled accurately by this distribution, as seen by the first plot. That is not surprising, as the particles are distributed uniformly in a 6D volume. The modelled volume beyond $\chi_6 = 2$ is therefore 728 times larger than the volume below this 6D radius, meaning that only 0.137% of the macroparticles will on average be distributed in this region. This is too few compared to the 8% of real particles that are supposed to be represented, and are modelled in the Gaussian distribution.

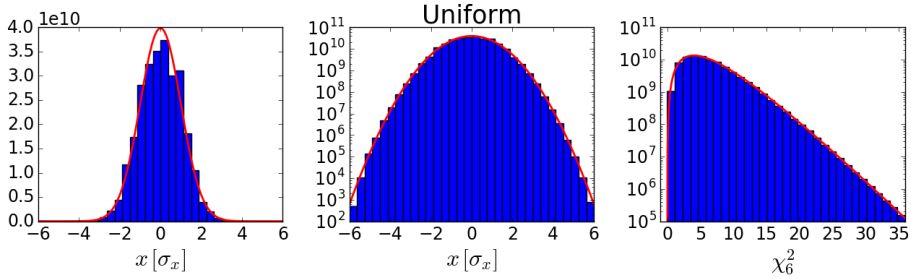

Figure 3.5: Comparison of the uniform initial distribution of $N_{\text{mp}} = 1 \times 10^5$ macroparticles, with actual Gaussian and χ_6^2 distributions. The sum of the weight of all particles is $N = 1 \times 10^{11}$. The first plot from the left displays a histogram of x. The second plot displays the same histogram of x, but with a log-scaled y-axis. The last plot displays a histogram of χ_6^2.

The regionally uniform distribution is a modification of the uniform distribution, attempting to improve the modelling of the core of the bunch. The number of macroparticles are divided into three approximately equally large groups. The particles in each group are distributed uniformly, requiring that they have a 6D radius within a given interval. The intervals are limited by the radii $\chi_6 \in \{0, 2, 4, 6\}$. Each particle within a group is weighted as in Eq. (3.11). In addition, the macroparticles in each group are weighted proportional to the volume of the region, V_{reg}, and to the inverse of the number of macroparticles in the region, N_{reg}, making the weight of macroparticle j proportional to

$$W_j \propto \frac{V_{\text{reg}}}{N_{\text{reg}}} \cdot \exp\left[-\frac{\chi_6^2}{2}\right], \tag{3.12}$$

whereupon the weights are normalised to give a total weight of N. The test of this regionally uniform distribution of $N_{\text{mp}} = 1 \times 10^5$ macroparticles is visualised in Fig. 3.6. Due to the higher den-

sity of particles at lower amplitudes, the core is much better modelled by this distribution. It seems that the good representation of the tail at high amplitudes is preserved from the uniform distribution, based on the log-scaled plots. The amplitude limits and number of particles of each region can be shifted, in addition to the number of regions. However, there was no significant reduction of the relative errors for other combinations. The regionally uniform IC with $N_{\text{mp}} = 1 \times 10^5$ macroparticles will be applied to study the evolution of the beam distribution, unless stated otherwise.

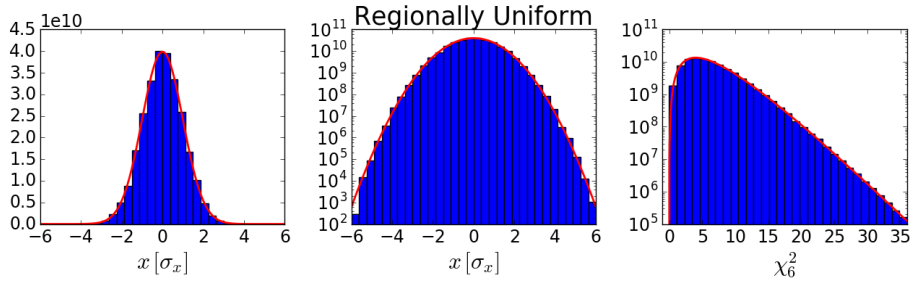

Figure 3.6: Comparison of the regionally uniform initial distribution of $N_{\text{mp}} = 1 \times 10^5$ macroparticles, with actual Gaussian and χ_6^2 distributions. The sum of the weight of all particles is $N = 1 \times 10^{11}$. The first plot from the left displays a histogram of x. The second plot displays the same histogram of x, but with a log-scaled y-axis. The last plot displays a histogram of χ_6^2.

3.4 Beam Quality Simulations

The method of this master project has been to study the evolution of measurable quantities in a real machine, such as growth of the beam emittance and loss rate of the beam intensity. This section provides information on how that is accomplished, based on the modelled physics and initial conditions presented earlier. Extending the memory argument from Sec. 3.3, the 6 dynamical dof cannot be saved for every particle after each turn. All values necessary to describe the individual particles are therefore stored in snapshots every $T_{\text{mid}} = 2 \times 10^4$ turns. This interval can be changed. The stored values are the 6 dynamical dof, whether a particle is lost or not, and the horizontal, vertical and longitudinal actions. Due to the modelled nonlinearities, the perturbed action of each particle is no longer independent of the unperturbed phase ϕ. Therefore, an average is taken of the action of each particle over the subsequent $T_\epsilon = 2048$ turns, to avoid the angle dependent fluctuations. Then the beam emittance is calculated for each snapshot as the average of these averaged actions.

During a normal physics fill in a high-energy circular hadron collider, the beam can circulate for hours. In the LHC, a fill time of 20 h equals $T_{\text{Tot}} = 8 \times 10^8$ turns. In the FCC-hh, an estimated 3 h of runtime would equal $T_{\text{Tot}} = 3 \times 10^7$ turns. Multiple reasons make tracking for that long using the weak-strong model inappropriate. First of all, in some settings the bunches will change size and charge non-negligibly from the initial distribution. In that case, the beam-beam interaction would not be modelled well by the weak-strong model. Another point is that numerical error builds up over time. Finally, more turns require more computer operations and the simulations will take more time. Simultaneously, one has to track for sufficiently many turns to represent accurately the long-term evolution of the beam quality in a given configuration. The results presented in this thesis have been acquired from tracking particles in the weak beam through usually $T_{\text{Tot}} = 2 \times 10^6$ turns, equivalent to 3 min in the LHC.

How the emittance growth and beam losses are calculated, will be presented in the following. Then another parameter will be introduced, referred to as the noise affected dynamic aperture

(*NADA*). For ease of notation, the hats (ˆ) will no longer be included. All three of these outputs will be represented by an example situation at the LHC working point, $(Q_x, Q_y) = (0.31, 0.32)$, with large beam-beam parameter $\xi_{\text{Tot}} = 0.03$, large chromaticity $Q' = 15$, regular normalised noise $\Delta = 1 \times 10^{-4}$, and zero crossing angle $\theta_{\text{xing}} = 0$.

3.4.1 Emittance growth

One of the effects the code investigates closely is the increase of emittance in both transverse planes separately. An increase in emittance leads to a decrease in luminosity. There are two different types of emittance growth. Close to resonances, the effective Hamiltonian diverges, and subsequently the actions are strongly perturbed. This leads to an almost immediate and possibly large emittance growth. A different important measure is the long-term emittance growth rate, $\dot{\epsilon}$, after the initial readjustment. To monitor the long-term growth rate, a linear regression curve of the beam emittance is computed, starting at turn $T_{\text{sim}} = 5 \times 10^5$. The evolution of the emittance for the example configuration is displayed in Fig. 3.7. The initial emittance growth of a few percent is visible, and the regression curve for each transverse emittance growth rate is plotted on top of the evolution. The emittance growth rates in both planes are larger than $\dot{\epsilon}_0 = 1 \times 10^{-8}$ /turn, as was expected from the noise alone. For simplicity, the average transverse emittance growth rate will be referred to as

$$\dot{\epsilon}_\perp = \frac{\dot{\epsilon}_x + \dot{\epsilon}_y}{2} \,, \tag{3.13}$$

which would be $\dot{\epsilon}_\perp = 3.23 \times 10^{-8}$ /turn in the example.

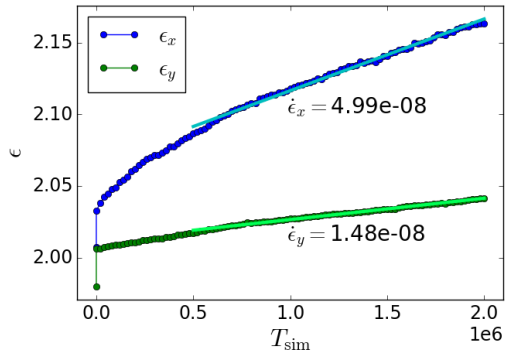

Figure 3.7: Example of evolution of beam emittance in both transverse planes, ϵ_x and ϵ_y. The beam emittance has been calculated for multiple snapshots every $T_{\text{mid}} = 2 \times 10^4$ turns. The growth rate has been calculated as described in Sec. 3.4.1. The beam emittances are given based on normalised coordinates as in Eq. (3.2), being $\epsilon = 2$ for a perfect Gaussian distribution. The straight lines in the lighter shade of blue and green correspond to the linear regressions performed to calculate the emittance growth rates.

The emittance growth rate is mostly dependent on the diffusion of the particles at low amplitudes in the core of the bunch. The convergence of the emittance growth rate with N_{mp} have been calculated for the Gaussian IC and the regionally uniform IC, which were both presented in Sec. 3.3. The average and the standard deviation from $\dot{\epsilon}_0$ has been calculated based on 40 independent growth rates for each N_{mp}. The relative errors from the expected growth rate are displayed in Fig. 3.8. The deviation between the calculated and expected emittance growth rate is, according to the central limit theorem, normally distributed with a standard deviation depending on the number of macroparticles as $\sigma = C/\sqrt{N_{\text{mp}}}$. A 1σ trend line has been plotted alongside the relative errors.

For $N_{\text{mp}} = 1 \times 10^5$ macroparticles, the Gaussian distribution has a 1σ relative error of 5%, while the regionally uniform distribution has a 1σ relative error of 15%.

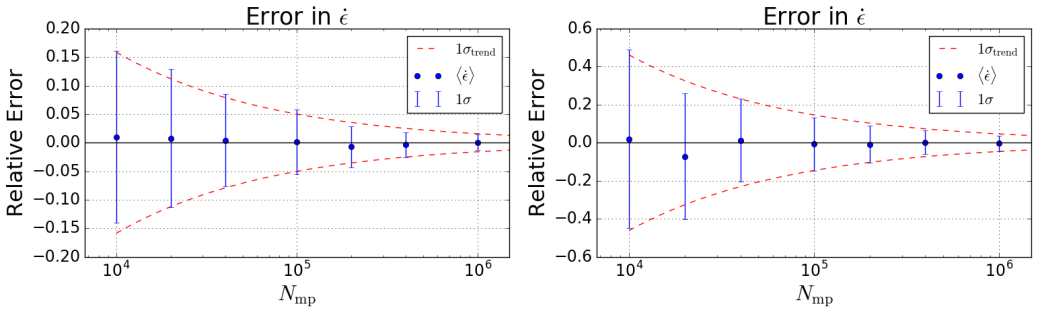

(a) Gaussian IC.

(b) Regionally uniform IC.

Figure 3.8: Convergence of relative error in measurements of the emittance growth rate, $\dot{\epsilon}$, for a configuration with only the noise of $\Delta = 1 \times 10^{-4}$. The relative error has been calculated separately for the Gaussian IC in (**a**) and the regionally uniform IC in (**b**).

The calculation of convergence of the emittance growth rate was repeated for a configuration at the LHC working point $(Q_x, Q_y) = (0.31, 0.32)$, also including a large beam-beam parameter $\xi_{\text{Tot}} = 0.03$ divided over two IPs, and a large chromaticity, $Q' = 15$, in addition to the noise. The emittance growth rate is larger in this configuration than when only the noise is included. The relative errors of the emittance growth rates are for this configuration calculated relative to the average emittance growth rate calculated with $N_{\text{mp}} = 1 \times 10^6$ macroparticles. The relative errors are plotted in Fig. 3.9. For $N_{\text{mp}} = 1 \times 10^5$ macroparticles, the Gaussian distribution has a 1σ relative error of approximately 16%, while the regionally uniform distribution has a 1σ relative error of 5%. It seems that the emittance growth rate is better modelled by the regionally uniform distribution for this configuration. Both ICs are reasonably accurate in calculating the emittance growth rate for both considered configurations.

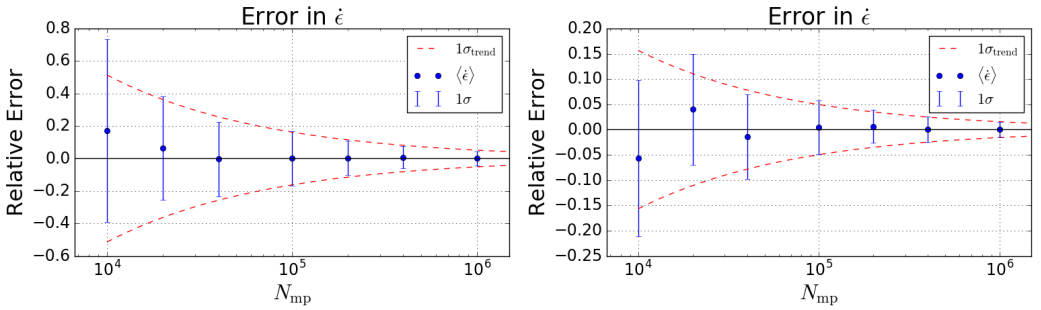

(a) Gaussian IC.

(b) Regionally uniform IC.

Figure 3.9: Convergence of relative error in measurements of the emittance growth rate, $\dot{\epsilon}$, for a configuration with $(Q_x, Q_y) = (0.31, 0.32)$, $\Delta = 1 \times 10^{-4}$, $\xi_{\text{Tot}} = 0.03$ and $Q' = 15$. The relative error has been calculated separately for the Gaussian IC in (**a**) and the regionally uniform IC in (**b**).

3.4.2 Beam loss

Loss of particles from the beam is another effect that reduces luminosity. CABIN does not take into account luminosity burn-off, only losses from particles going to too high amplitudes, reaching the collimation system. There are two separate types of beam losses to large amplitudes. The instantaneous beam loss transports particles beyond the limit within a few couple of turns. One cause of this is that particles can be initialised beyond the limit. These losses can in operation be greatly limited by matching the beam correctly to the machine, but there are almost inevitably some losses in transitions. Particles that are strongly perturbed by resonances can also be lost instantaneously. These losses may be reduced by choosing suitable machine tunes that will put the beam far from strong resonances. Nevertheless, for large beam-beam parameters, some instantaneous losses when the beams are brought into collision may be unavoidable. After the initial losses, the long-term diffusion can also make particles drift out. These losses are partly unavoidable without any damping mechanisms, and keeping them low is a main objective in the design and operation of a collider. The long-term loss rate of particles is calculated based on the conserved intensity for each snapshot. The loss rates are calculated as the relative decrease from the initial intensity, by a linear regression starting at turn $T = 5 \times 10^5$. This gives a better estimate for how long the beam will stay in the machine, than if the instantaneous losses were included.

A particle in a real machine is lost at large amplitudes because it hits the collimation system. In the LHC this is typically at a transverse radius of $R_M = 6\sigma_\epsilon$, where σ_ϵ is the transverse sigma corresponding to the operational emittance of the beams. In CABIN, the transverse radius is checked once per turn, and if it is ever beyond a given limit R, it is considered lost forever. The particle is still tracked to study the emittance growth to larger amplitudes. The intensity below the machine limit, R_M, and a beam limit, $R_B = 5\sigma_\Sigma$, are displayed in Fig. 3.10. Here σ_Σ is the beam size of the strong beam in the simulation. Many particles are lost beyond R_B that appear to stop between the two limits. This is probably because the strength of the beam-beam interaction decreases fast for larger amplitudes, as was detailed in Fig. 2.6. Nonlinearities due to the magnets in a real lattice cause stronger deflections at larger amplitudes. Thus, it has been assumed that particles being transported to R_B, are likely to be lost within a small number of turns. Hence, the results presented later refer to the loss rate from the beam (LR_{Beam}) beyond R_B, and not the unsuitable loss rate from the machine (LR_{LHC}) beyond R_M. The values are scaled to represent loss rates per hour in a ring with revolution frequency $f_{\text{rev}} = 11.245\,\text{kHz}$, such as the LHC. If the beams are flat, the limits are

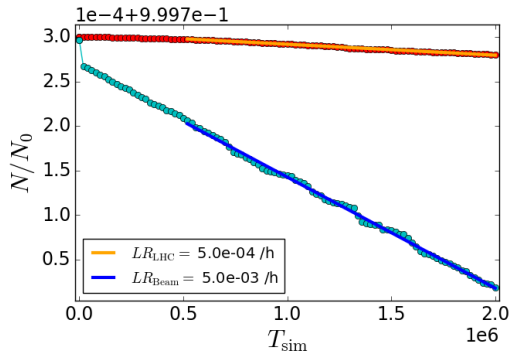

Figure 3.10: Example of evolution of bunch intensity, relative to the initial intensity, N_0. The intensity has been stored every $T_{\text{mid}} = 2 \times 10^4$ turns. The loss rates have been calculated as described in Sec. 3.4.2. The orange and dark blue straight lines represent the linear regression from which the loss rate is found.

taken proportional to the relevant σ, giving an elliptical collimation. In order to fully describe the diffusion of the particles from R_B to the actual collimator position, a complete nonlinear model of the magnetic lattice should be implemented, but this is beyond the scope of this study.

The beam loss rate is mostly dependent on the particles in the tail of the bunch. The convergence of the beam loss rate with N_{mp} has been calculated for the Gaussian IC and the regionally uniform IC, which were both presented in Sec. 3.3. For a configuration only including a noise of rms amplitude $\Delta = 1 \times 10^{-4}$, there is no analytical loss rate. The average loss rates have been calculated based on 20 independent values for each N_{mp}. The standard deviations have been calculated relative to the average loss rate calculated for $N_{\text{mp}} = 1 \times 10^6$ macroparticles, which was approximately $0.04\%/\text{h}$ for both ICs. The relative errors from this loss rate are plotted in Fig. 3.11. For $N_{\text{mp}} = 1 \times 10^5$ macroparticles, the Gaussian distribution has a 1σ relative error of approximately 86%, while the regionally uniform distribution has a 1σ relative error of 8%. The large error for the Gaussian IC is caused by the lack of particles initialised at large amplitudes.

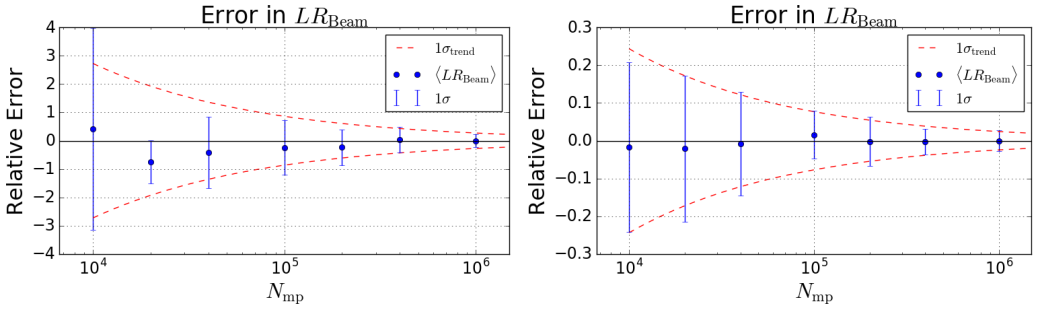

(a) Gaussian IC. **(b)** Regionally uniform IC.

Figure 3.11: Convergence of relative error in measurements of the beam loss rate, LR_{Beam}, for a configuration with a noise of $\Delta = 1 \times 10^{-4}$ only. The relative error has been calculated separately for the Gaussian IC in (**a**) and the regionally uniform IC in (**b**).

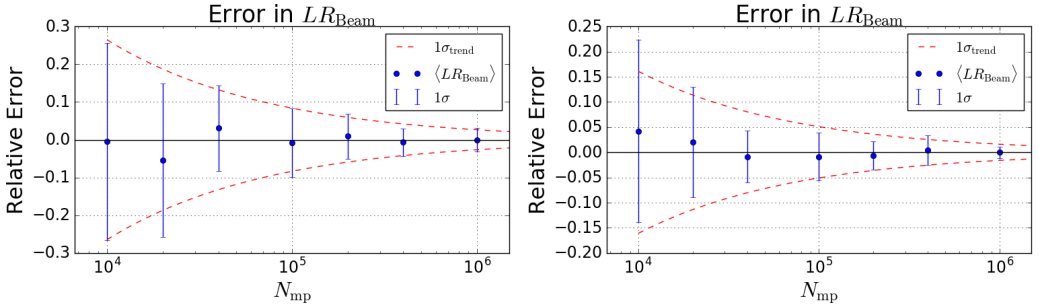

(a) Gaussian IC. **(b)** Regionally uniform IC.

Figure 3.12: Convergence of relative error in measurements of the beam loss rate, LR_{Beam}, for a configuration with $(Q_x, Q_y) = (0.31, 0.32)$, $\Delta = 1 \times 10^{-4}$, $\xi_{\text{Tot}} = 0.03$ and $Q' = 15$. The relative error has been calculated separately for the Gaussian IC in (**a**) and the regionally uniform IC in (**b**).

The convergence of the beam loss rate can be repeated for a configuration at the LHC working point $(Q_x, Q_y) = (0.31, 0.32)$, also including a large beam-beam parameter, $\xi_{\text{Tot}} = 0.03$, divided over two IPs, and a large chromaticity, $Q' = 15$, in addition to the noise. The beam loss rate is larger in this configuration than when only the noise is included. The error was also for this configuration calculated relative to the average loss rate for $N_{\text{mp}} = 1 \times 10^6$ macroparticles, which was $4\%/\text{h}$ for both ICs. The relative errors from this growth rate are plotted in Fig. 3.12. For $N_{\text{mp}} = 1 \times 10^5$ macroparticles, the Gaussian distribution has a 1σ relative error of approximately 8%, while the regionally uniform distribution has a 1σ relative error of 5%. Both ICs are reasonably accurate for this configuration with a relatively large loss rate. However, the Gaussian IC is strongly inaccurate for configurations that would give small loss rates. That is the main reason why the regionally uniform distribution will be applied for the beam quality simulations in Ch. 4.

3.4.3 Noise affected dynamic aperture

All the particles in the example configuration that are lost from the machine beyond R_M, and from the beam beyond R_B, are marked by a red cross in Fig. 3.13. This includes particles of all longitudinal amplitudes. It is, as from the intensity evolution, clearly visible that many particles lost beyond R_B never make it beyond R_M. In this example, the first lost particle beyond both limits is at a transverse amplitude of $r = 2.35\sigma_\Sigma$. This number cannot be linked directly to the loss rate. Furthermore, it does not value the seemingly good stability at large vertical amplitudes and small horizontal amplitudes for this configuration. It only gives a measure on how deep into the bunch the resonances are strongly affecting the motion of particles.

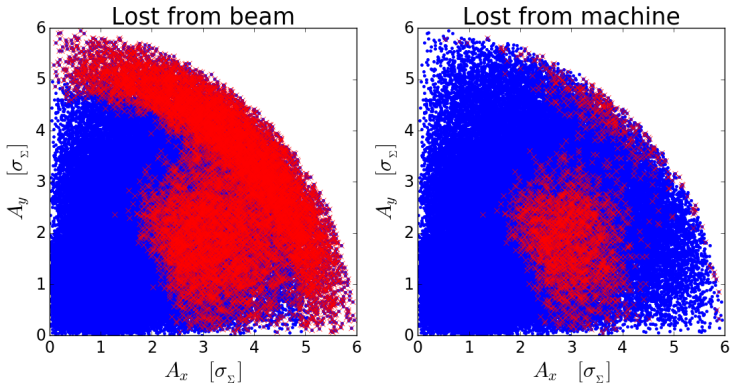

Figure 3.13: Example of which particles are lost from the bunch during a simulation. The initial positions in (A_x, A_y) space are displayed as blue points. All particles lost beyond a limit are marked by a red cross. The left plot displays the particles lost beyond $R_B = 5\sigma_\Sigma$. The right plot displays the particles lost beyond $R_M = 6\sigma_\epsilon$. The limits were defined in Sec. 3.4.2.

The dynamic aperture (DA) is the largest radius of the innermost region in (x, y) space where the motion in an accelerator is stable [41]. Particles initialised in this region will remain stable for ever.

$$r(0) < DA \qquad \Rightarrow \qquad r(T \to \infty) < \alpha < \infty \,, \tag{3.14}$$

where $r = \sqrt{A_x^2 + A_y^2}$ and α is any positive, finite length. In practice, one cannot study stability as the particle amplitude remaining finite until infinity. One can discuss short-term DA, for which the particles remain stable for 10^3 to 10^4 turns, and long-term DA, for which the particles remain

stable for 10^7 to 10^9 turns. The motion is less stable for larger longitudinal amplitude. Therefore, one should only consider particles with longitudinal amplitude below a certain limit.

CABIN studies the effect of the beam-beam interaction, coupled with a Gaussian noise, making the calculation somewhat different from other studies. Therefore, the dynamic aperture equivalent in CABIN is called the noise affected dynamic aperture (*NADA*). First of all, the noise will make all particles drift to infinity given enough turns. To be able to study the *NADA* simultaneously with the emittance growth and beam losses, the code considers a particle as stable if it is not lost within T_{Tot}, being 2×10^6 turns for the results presented later. Second of all, the beam-beam interaction is weaker at larger amplitudes, making particles stay between R_B and R_M. This stability region is likely to be altered by other mechanisms, in particular the interaction with nonlinear errors of the magnetic lattice. *NADA* is in this thesis defined as the smallest radius of the particles initialised below $A_s = 2.5\sigma_s$ that are lost beyond R_B. These values are intended as a diagnostic tool to compare different configurations studied with CABIN, but are not directly comparable to *DA* in other studies.

How fast the *NADA* converges with respect to N_{mp} could be tested similarly to the convergence for the emittance growth rate and the loss rate. The *NADA* is however not dependent on the IC as a whole, but rather on where the individual macroparticles are initialised. Thus, the average *NADA* has been found to decrease as N_{mp} increases, unlike the emittance growth rate and the beam loss rate. For $N_{\text{mp}} = 1 \times 10^5$ macroparticles in the regionally uniform IC, the standard deviation is less than 6% for the configurations used in the previous convergence studies.

3.5 Frequency Map Analysis

The beam quality simulations introduced in Sec. 3.4 enables CABIN to quantitatively study the evolution of measurable quantities. The underlying mechanisms driving the beam quality degradation are not always clear from these outputs alone. Analytical considerations, as introduced in Ch. 2, are often limited in complexity and to leading order. Due to nonlinearities, numerical diagnostic tools are needed as well. One such tool that has been implemented in CABIN is frequency map analysis (FMA). FMA is a method that can qualitatively visualise the detrimental effects of beam-beam interactions, based on the evolution of the tunes of individual particles [42].

For a configuration only including the linear lattice for zero chromaticity, all particles have tunes (Q_x, Q_y). Due to the nonlinear beam-beam interaction, the tunes of each particle j are shifted to (Q_{xj}, Q_{yj}) separately, as was detailed in Fig. 2.10. The action of a particle may increase close to a resonance, leading to a change of the tune. Hence, it is of interest to monitor the tunes of individual particles closely, both to know which resonances may be excited, and because the change in tune can indicate the severity of the diffusion close to a given resonance. One can calculate a tune diffusivity, D_j, for each particle, based on how much the tunes change per turn

$$D_j = \log_{10} \sqrt{\left(\frac{\mathrm{d}Q_{xj}}{\mathrm{d}T}\right)^2 + \left(\frac{\mathrm{d}Q_{yj}}{\mathrm{d}T}\right)^2} \tag{3.15}$$

where T is the turn number. The change per turn can be calculated as a linear regression based on the different tune measurements. The tune diffusivity is then used as a colour scale for each particle individually, presented as a footprint in tune space, (Q_x, Q_y), or in initial amplitude space, (A_x, A_y). In the results that will be presented later, the diffusivity constant, D_j in Eq. (3.15), is calculated for $N_{\text{mp}} = 4 \times 10^4$ macroparticles. These are initially distributed in a quadratic, uniform IC in the first quadrant of the (x, y) plane, with $s(T = 0) = 1$, unless stated otherwise. To focus on the effect of the beam-beam interactions, these simulations will be run with zero noise.

The tunes may be drifting, or they may oscillate around a mean, as would be expected for a nonzero chromaticity. The tune oscillation with chromaticity has a period of $1/Q_s$ turns. By measuring each tune based on data from more than $1/Q_s$ turns, the periodic tune variations due to the chromaticity will be reduced. By calculating the diffusivity based on multiple tunes, the calculation is less sensitive to periodic variations caused by either chromaticity or other sources. On the other hand, the tune calculations are slow, favouring less points. As a compromise, the tune diffusivity will be calculated as the slope of a linear regression of $n_Q = 10$ tunes spaced by $T_{\text{mid}} = 1 \times 10^4$ turns. This combination has been found through a convergence study.

3.5.1 Tune calculations

The tunes can be calculated using a FFT. However, the FFT can only calculate tunes of resolution $1/T_Q$ where T_Q is the number of turns used for the calculation. It has been required that the tune is calculated with high precision, based on a low number of turns. This is necessary to reduce storage requirements and to locate the post-processed value at a single turn instead of spread over a series of turns. To achieve higher precision in the tune measurements, an envelope of the FFT can be applied to find an intermediate frequency. There are codes developed at CERN that do this. PySussix is a python wrapper for a multi-purpose code written in Fortran [43, 44]. PySussix can find the tune, but multiple unrelated operations are performed simultaneously, which greatly reduces the performance. Another code, named HARPY, contains functions that only aim at finding the correct tune [45]. A comparison of the speed and accuracy of these three methods has been done, and the results are presented in Fig. 3.14. The codes have attempted to find the tune of the sine function $\sin(2\pi QT)$, where T are integers incrementing with 1, representing the turns. Each code tried calculating 150 different tunes Q, which were randomly distributed on the interval $(0, 0.5)$. In summary, the FFT performs as expected with an error decreasing as $1/T_Q$. Both PySussix and HARPY are more precise, the errors for both decrease faster than $1/T_Q^2$. HARPY is about a factor 100 times faster than PySussix, and is the chosen code for calculating the tunes, using $T_Q = 2^n$, where $n \geq 10$. For most results presented later, $n = 12$ ($T_Q = 4096$), unless stated otherwise.

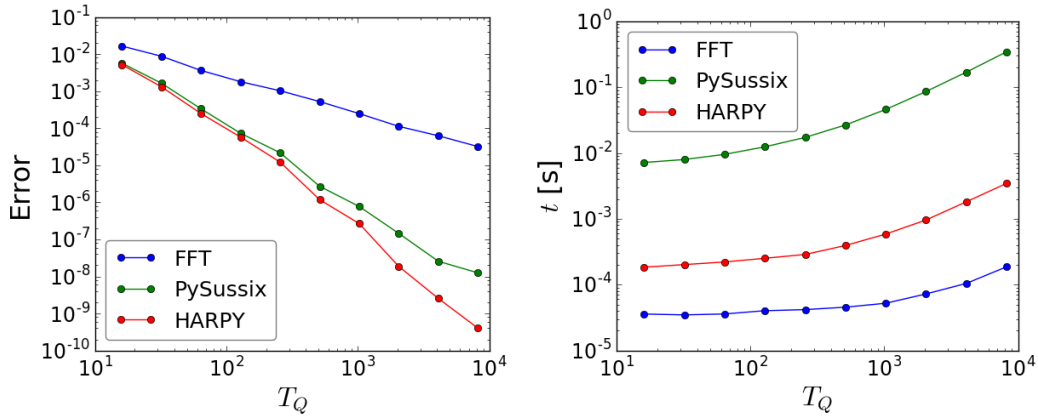

(a) **(b)**

Figure 3.14: Plot comparing the ability of FFT, PySussix [43] and HARPY [45] to calculate tunes. (**a**) displays the absolute error of the tune calculations. (**b**) displays the required time to calculate a single tune. T_Q are the number of points used to calculate the tunes, all are powers of 2. 150 tunes have been calculated for each T_Q for each method.

The detuning with amplitude due to the beam-beam interaction from a round, strong beam has been addressed analytically in 1D to the first order. Requiring that $A_y = 0$, the beam-beam tune shift ΔQ_x is given by Eq. (2.65). This was extended to include horizontal and vertical separation between the beams. Comparison to tunes calculated from tracking data by use of HARPY is done in Fig. 3.15. The simulations have been done with a small beam-beam parameter, $\xi = 0.001$, to reduce the effect of possible resonances, and to make the first order assumption valid. The tunes have been calculated based on $T_Q = 4096$ turns. There is a good agreement between the analytically predicted tune shifts and the tune shifts calculated using HARPY on tracked data.

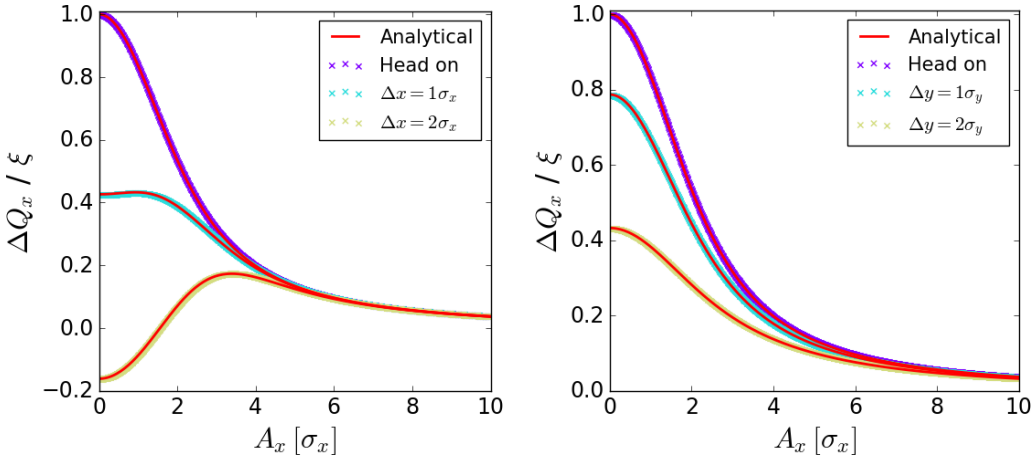

Figure 3.15: Horizontal tune shift, ΔQ_x, induced by the HO beam-beam interaction on a 1D beam distributed along the x axis. (**a**) displays the tune shift for separation between the beams in the horizontal direction. (**b**) displays the tune shift for separation between the beams in the vertical direction. The red curves labelled "Analytical", have been calculated for each separation separately.

Chapter 4

RESULTS AND DISCUSSION

Results acquired from application of CABIN will be presented and discussed in this chapter. Different parameters are varied in the following sections, to see the impact on the dynamics of the particles in the weak beam. Beam quality simulations will be run for each configuration as explained in Sec. 3.4. To explain the behaviour expressed by these simulations, a subset of interesting configurations will be simulated without noise to produce FMAs, as explained in Sec. 3.5. Unless otherwise specified, the parameters are given by Tab. 3.1.

Many configurations will be tested in this chapter. The different configurations will be compared based on certain outputs from CABIN, which will be explained shortly here. A more thorough explanation was given in Sec. 3.4. LR_{Beam} is the loss rate of particles per hour, calculated for the LHC revolution frequency, $11.245\,\mathrm{kHz}$. The particles are counted as lost if they go to higher transverse amplitudes than $R_B = 5\sigma_\Sigma$, where σ_Σ is the transverse beam size of the strong beam. *NADA* is the smallest transverse radius among the particles that are lost in the simulation, which where initialised with a limited longitudinal amplitude, $A_s \leq 2.5\sigma_s$. The maximum value is $5\sigma_\Sigma$, and larger is better. This value is partially correlated to the loss rate. $\dot{\epsilon}_\perp$ is the average transverse long-term emittance growth rate. For the beam quality simulations, the noise alone will cause a normalised emittance growth rate of $\dot{\epsilon}_0 = 1 \times 10^{-8}\,/\mathrm{turn}$. If the measured emittance growth rate for a certain configuration is within 10% of $\dot{\epsilon}_0$, the beam-beam interaction is considered not to have had additional detrimental effects.

4.1 Search for Working Point

The tunes caused by the linear lattice alone, (Q_x, Q_y), often referred to as the working point, have large implications on the beam quality. Due to the nonlinear beam-beam interaction, many resonances may affect the beam, visualised by the resonance lines in Fig. 2.13. In addition, the beam-beam interaction causes a tune-spread among the particles in the bunch, of horizontal and vertical width, given by Eq. (2.85). The total beam-beam tune shift is relatively small in the LHC today, and the working point of $(Q_x, Q_y) = (0.31, 0.32)$ has proven itself over many years to preserve the beam quality sufficiently well. Future upgrades will however bring with them a larger beam-beam tune shift, as this is necessary to achieve a higher luminosity.

In this section is a working point scan performed in (Q_x, Q_y) space, to look for other, possibly more suitable, working points for larger beam-beam tune shifts. The tested working points are between the 4th order and 6th order resonances, including the LHC working point, and in the tune

area below the half integer resonance. The latter was tested due to the lack of low order lines in Fig. 2.13. The scans are performed with a tune resolution of 0.0025. Because there is complete symmetry between the tracking of horizontal and vertical phase space in CABIN, only the upper half of the diagonal has been calculated. For the opposite combination of Q_x and Q_y, the loss rate has been copied, while the horizontal and vertical emittance growth rates have been exchanged. All simulations are run for a total beam-beam tune shift of $\Delta Q_{\mathrm{Tot}}(\phi_{\mathrm{PIW}}) = 0.03$, combined with a large chromaticity, $Q' = 15$, and a considerable Piwinski angle, $\phi_{\mathrm{PIW}} = 0.9$, corresponding to a full crossing angle of $\theta_{\mathrm{xing}} = 300\,\mu\mathrm{rad}$. This is considered similar to the worst-case scenario for the FCC-hh, based on the values presented in Tab. 3.1. The crossing angle is chosen nonzero to also include odd resonances in order to remain in a pessimistic scenario.

The tune scan on the interval $Q_q \in [0.255, 0.345]$, in both transverse tunes, is presented in Fig. 4.1. The working point dependence is similar for the loss rate and the emittance growth rate. There is generally better preservation of the beam quality with a working point on or close to the coupling resonance, $Q_x = Q_y$. This dependence is also found in the LHC, as will be covered in Sec. 4.7. However, instabilities can develop for working points too close to the diagonal. CABIN does not properly model the effect of the coupling resonance as it does not include coherent instabilities or magnetic errors from the lattice. While it is not excluded that such working points can be used, a proper demonstration is required. To be conservative, it is assumed in the following that a finite tune separation of $|Q_x - Q_y| \geq 0.01$ is needed, as for the LHC. The working point with the lowest beam loss rate and emittance growth rate in this tune area, at least this far from the diagonal in tune space, is $(Q_x, Q_y) = (0.315, 0.325)$.

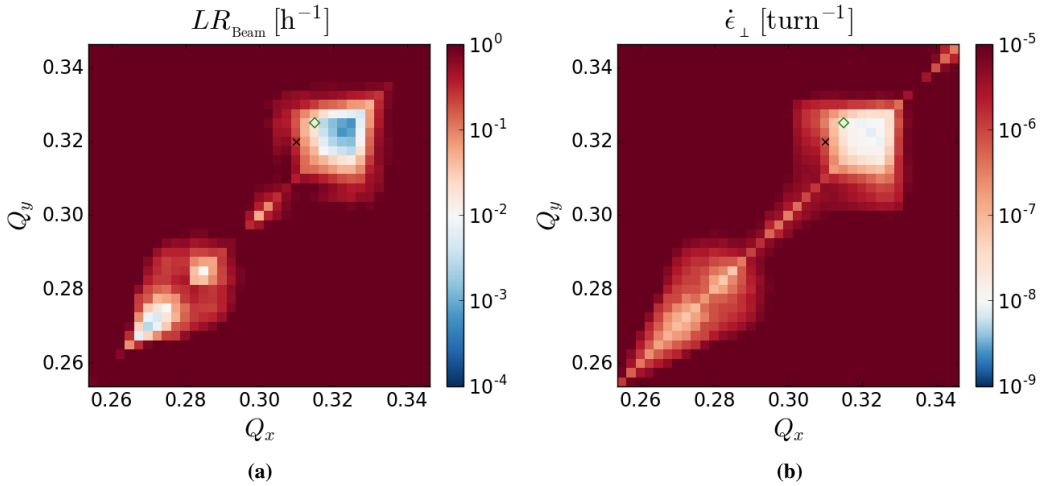

Figure 4.1: Scan in (Q_x, Q_y) space, for $\Delta Q_{\mathrm{Tot}}(\phi_{\mathrm{PIW}}) = 0.03$, $\beta_q^* = 40\,\mathrm{cm}$, $\phi_{\mathrm{PIW}} = 0.9$ and $Q' = 15$. (**a**) displays the loss rate per hour and (**b**) displays the emittance growth rate per turn, calculated as explained in Sec. 3.4. The black cross ($\times$) marks the LHC working point, $(Q_x, Q_y) = (0.31, 0.32)$. The green diamond ($\diamond$) marks the suggested working point for this configuration, $(Q_x, Q_y) = (0.315, 0.325)$.

The tune scan on the interval $Q_q \in [0.45, 0.505]$, in both transverse tunes, is presented in Fig. 4.2. The working point dependence is similar for both the loss rate and the emittance growth rate. There is, also according to this tune scan, generally better preservation of the beam quality with a working point on or close to the coupling resonance, $Q_x = Q_y$. The working point with best preservation of beam quality in this tune area, requiring again that $|Q_x - Q_y| \geq 0.01$, is

$(Q_x, Q_y) = (0.475, 0.485)$. Close to the half-integer resonance, dipole errors and non-ideal optics can be difficult to correct for and control. However, modern correction techniques suggest that such working points may be attainable [46]. The dipolar component of the beam-beam interaction can cause the entire bunch to be lost immediately, if either the horizontal or vertical tune is larger than, yet close to, 0.5. This is marked by the white crosses on blue background in Fig. 4.2a. There are two working points far from the diagonal where the average emittance growth rates are approximately equal to $\dot{\epsilon}_0 = 1 \times 10^{-8}$ /turn in this tune scan. The loss rates are too large for these working points to be considered for a collider. Further inspection shows that there is a large initial emittance growth in one plane followed by a strong mixing of the horizontal and vertical emittance, even if the average long-term growth rate is limited. The initial emittance growth corresponds to a considerable change in the beam size, making the beam significantly different from the initial Gaussian distribution, and making the assumption of a fixed distribution for the strong bunch invalid.

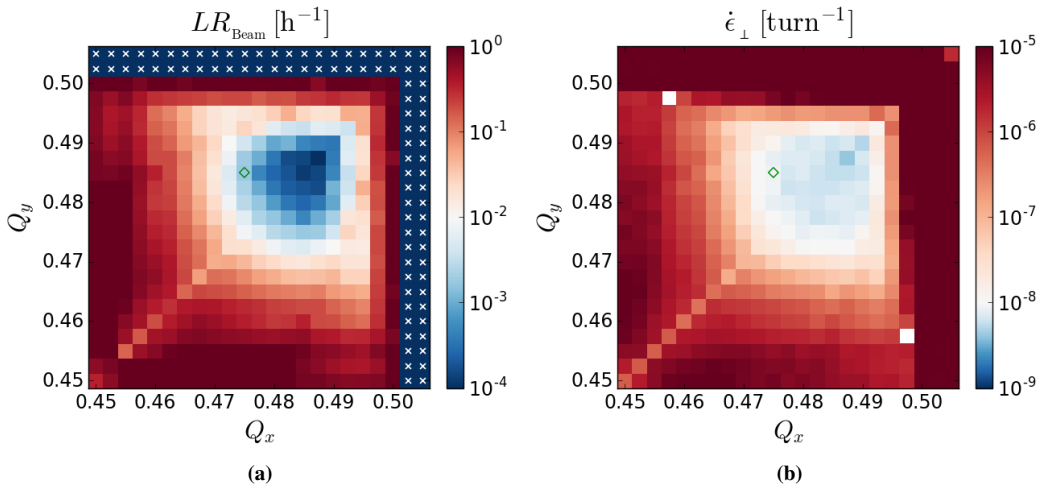

Figure 4.2: Scan in (Q_x, Q_y) space, for $\Delta Q_{\text{Tot}}(\phi_{\text{PIW}}) = 0.03$, $\beta_q^* = 40\,\text{cm}$, $\phi_{\text{PIW}} = 0.9$ and $Q' = 15$. (**a**) displays the loss rate per hour and (**b**) displays the emittance growth rate per turn, calculated as explained in Sec. 3.4. At the working points marked by blue squares with white crosses in (**a**), the entire beam was lost before the long-term loss rate could be calculated. The green diamond (◇) marks a suggested working point in this tune area, $(Q_x, Q_y) = (0.475, 0.485)$.

The footprint of the bunch in (Q_x, Q_y) space is wider, in addition to longer, with a larger beam-beam parameter. It could therefore be argued that the difference between the tunes in the alternative working points should be larger than $|Q_x - Q_y| = 0.01$. This has not been done in the following sections for multiple reasons. As discussed above, CABIN does not model the effect of the coupling resonance properly. To compare to the LHC working point, it is better to keep the tune separation equal. Another big cause of the footprint width in circular colliders, are the parasitic long-range interactions that CABIN does not model yet. The LR effects are expected to become weaker in the FCC-hh due to the reduction of the transverse emittance, and thus the relative tune width will be smaller. The small tune separation remains a possible good choice also for scenarios with larger beam-beam parameters [36].

Two working points have been found above to give better preservation of beam quality than the LHC working point. That is because the simulations are run for a configuration with stronger beam-beam interactions than what is common in the LHC. To emphasise this point, a tune scan is done for different configurations along the diagonal from $(Q_x, Q_y) = (0.305, 0.315)$ to $(0.32, 0.33)$. The

results are given in Fig. 4.3, where the vertical tune, Q_y, is 0.01 larger than Q_x, which is given by the x axis. The red curve corresponds to the tune scans discussed above, for which the best working point again is found close to $Q_x = 0.315$. A horizontal tune $Q_x \geq 0.315$ seems to be optimal also without the crossing angle. For a smaller beam-beam tune shift, $\Delta Q_{\mathrm{Tot}}(\phi_{\mathrm{PIW}}) = 0.01$, it is however calculated a smaller loss rate and a larger *NADA* for the LHC working point, with a nonzero crossing angle. The causes of the difference in beam quality preservation between large and small tune shift, and between zero and nonzero crossing angle, will be discussed in more detail later. The importance of this remark is that the optimum working point is highly dependent on the configuration.

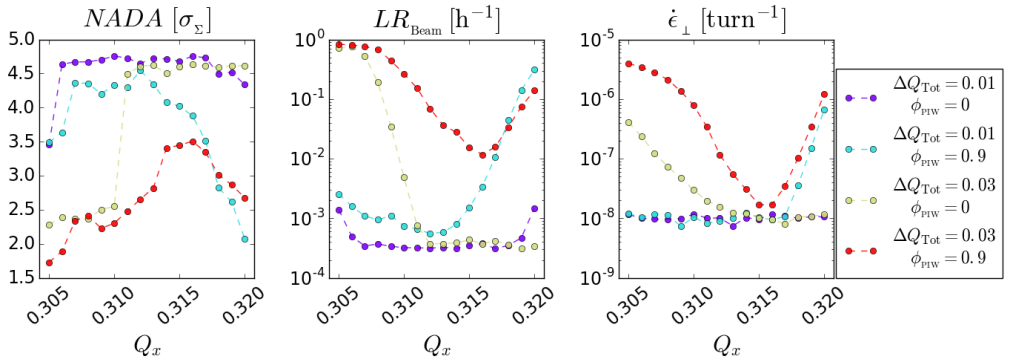

Figure 4.3: Beam quality reduction for different configurations given by the legend, varying ϕ_{PIW} and $\Delta Q_{\mathrm{Tot}}(\phi_{\mathrm{PIW}})$. All configurations include a large chromaticity, $Q' = 15$. The outputs *NADA*, LR_{Beam} and $\dot{\epsilon}_\perp$ have been calculated as expressed in Sec. 3.4. The results are presented as functions of the working point, and the vertical tune, Q_y, is for each horizontal tune equal to $Q_x + 0.01$.

4.2 Crossing Angle

In circular colliders with several bunches, the beams generally collide with a nonzero crossing angle, so that parasitic collisions with the opposing beam are long-range and therefore less detrimental to the beam quality. A nonzero crossing angle introduces mixing between the longitudinal and transverse planes, leading to additional resonances. In addition, a nonzero crossing angle reduces the luminosity at the IP. This section studies the effect of varying the crossing angle for the main head-on interaction only, the effect of the parasitic interactions is not included. Beam quality simulations for round beams have been run for each of the following studies, with Piwinski angles $\phi_{\mathrm{PIW}} \in \{0, 0.1, 0.3, 0.6, 1, 1.5, 2\}$, and beam-beam parameters $\xi_{\mathrm{Tot}} \in \{0.01, 0.02, 0.03, 0.04, 0.05\}$, from which the effective maximum beam-beam tune shifts can be calculated by Eq. (2.84).

The results from a crossing angle scan for the machine tunes of $(Q_x, Q_y) = (0.31, 0.32)$, and zero chromaticity, are presented as functions of ϕ_{PIW} in Fig. 4.4a. The beam quality remains fairly good in the core for $\xi_{\mathrm{Tot}} \leq 0.03$ and zero crossing angle, as seen by the emittance growth rate, and in the tail for $\xi_{\mathrm{Tot}} \leq 0.04$, as seen by the loss rate. The large *NADA* also signifies that the particles are not transported from deep within the bunch to be lost. As the angle increases from $\phi_{\mathrm{PIW}} = 0$ to 0.6, the general behaviour based on all three outputs is that the detrimental effects gradually become stronger, strongly dependent on ξ_{Tot}. The preservation of the beam quality reaches a minimum within the interval $\phi_{\mathrm{PIW}} \in [0.6, 1]$. For larger angles, the beam quality preservation begins to improve as the crossing angle increases further from $\phi_{\mathrm{PIW}} = 1$ to 2. The same results are plotted as functions of $\Delta Q_{\mathrm{Tot}}(\phi_{\mathrm{PIW}})$ in Fig. 4.4b. From this plot, it seems that the additional detrimental effects caused

by the crossing angle saturates around $\phi_{\text{PIW}} \approx 1$, and the apparent improvement when the crossing angle increases further is due to the reduction of the effective beam-beam tune shift.

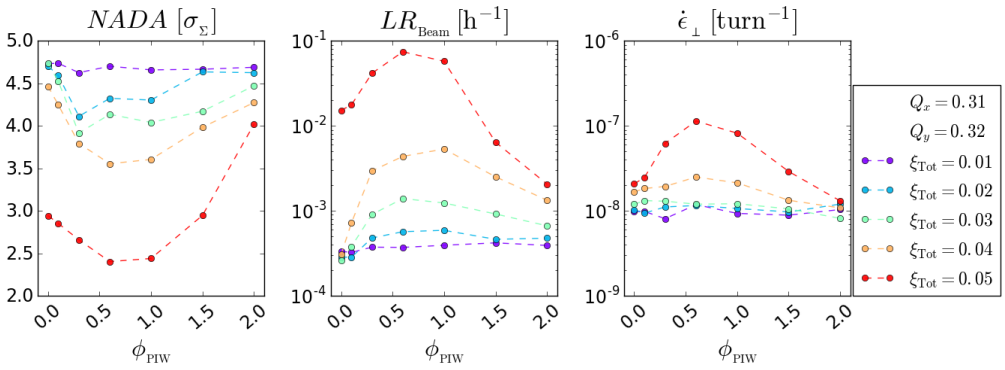

(a) $Q' = 0$.

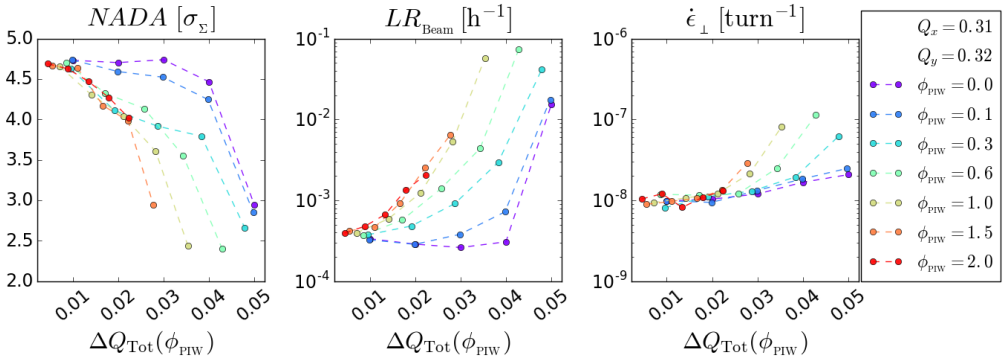

(b) $Q' = 0$.

Figure 4.4: Beam quality reduction for different combinations of ϕ_{PIW} and ξ_{Tot}, when $Q_x = 0.31$, $Q_y = 0.32$, $Q' = 0$ and $\beta_q^* = 0.4\,\text{m}$. The outputs $NADA$, LR_{Beam} and $\dot{\epsilon}_\perp$ have been calculated as expressed in Sec. 3.4. (**a**) presents the outputs as functions of ϕ_{PIW}. (**b**) presents the outputs as functions of $\Delta Q_{\text{Tot}}(\phi_{\text{PIW}})$.

The behaviour for $\phi_{\text{PIW}} = 0$ can in part be understood based on the first three FMAs in Fig. 4.5. For $\xi_{\text{Tot}} = 0.03$, the particle trajectories are affected by the 10th order resonances and weakly by the 16th order, but there is only weak overlap between different resonances. For $\xi_{\text{Tot}} = 0.04$, the 10th order resonances cause higher diffusion coefficients, and they overlap with the coupling resonance at low particle amplitudes. This may explain the slightly larger emittance growth rate without the high loss rates. For $\xi_{\text{Tot}} = 0.05$, the 10th order resonances affect the entire width of the footprint, and they overlap now strongly with both the 16th order resonances and the coupling resonance. There is a strong overlap also for particles of larger transverse amplitudes, which might explain the substantial increase in the loss rate for this configuration.

The additional problems with an increasing angle, when $\phi_{\text{PIW}} < 1$, is qualitatively predictable, because with the crossing angle, the beam-beam interaction drives odd resonances as well. The 13th order resonance is active in this configuration, as displayed in the FMA in Fig. 4.5d, and it affects predominantly particles at large transverse amplitudes. This resonance may contribute to the large loss rates of particles from the tail compared to the moderate emittance growth rates of the particles

in the core for a nonzero crossing angle. The synchro-betatron resonances parallel to the coupling resonance, i.e. for nonzero m in $Q_x - Q_y + m \cdot Q_s = 0$, also have a higher diffusion coefficient than for zero crossing angle. This FMA was produced for a small angle of $\phi_{\text{PIW}} = 0.1$, because the picture became distorted beyond clear understanding for larger angles. The improvement of the beam quality preservation, when increasing the Piwinski angle further beyond 1, was justified earlier as an effect of the reduction of the beam-beam tune shift. This effect is detailed in the FMA in Fig.4.5e, for $\phi_{\text{PIW}} = 2$. The footprint fits between the dominant resonance lines of lowest order. Even though the footprint crosses the 10th order resonance lines at $Q_x = 0.3$, this resonance is not significant, as it is only affecting the particles of lowest transverse amplitude. Because the effects of larger crossing angle seem to be strongly connected to the reduced tune shift, the following results in this section are only given as functions of $\Delta Q_{\text{Tot}}(\phi_{\text{PIW}})$.

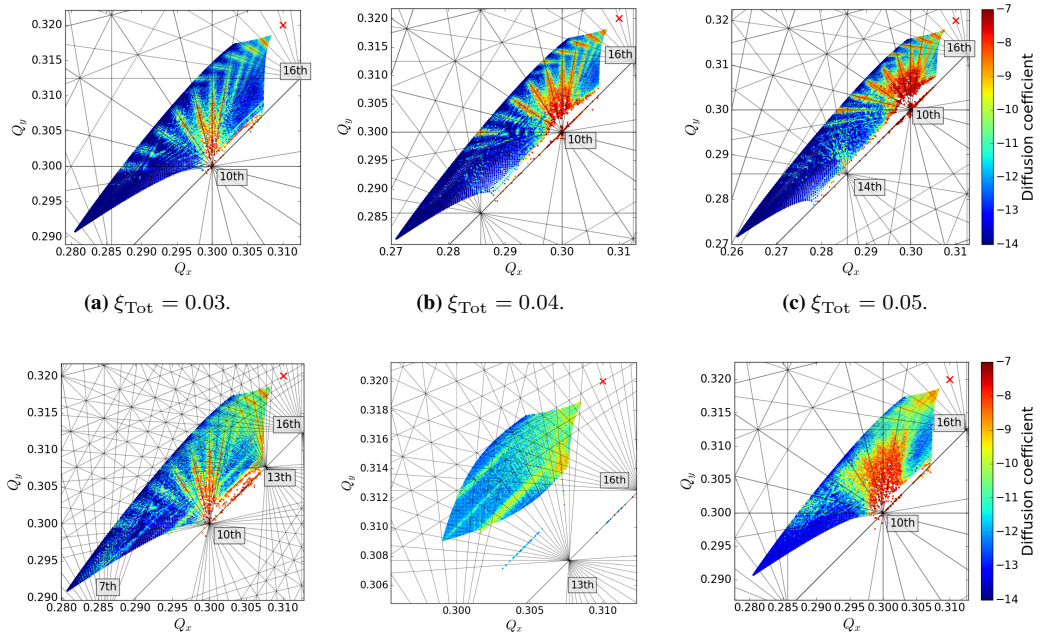

(a) $\xi_{\text{Tot}} = 0.03$. **(b)** $\xi_{\text{Tot}} = 0.04$. **(c)** $\xi_{\text{Tot}} = 0.05$.

(d) $\xi_{\text{Tot}} = 0.03$, $\phi_{\text{PIW}} = 0.1$. **(e)** $\xi_{\text{Tot}} = 0.03$, $\phi_{\text{PIW}} = 2$. **(f)** $\xi_{\text{Tot}} = 0.03$, $Q' = 15$.

Figure 4.5: FMAs illustrating effects of increased beam-beam parameter, Piwinski angle and chromaticity for a working point of $(Q_x, Q_y) = (0.31, 0.32)$, related to the beam quality study in Fig. 4.4 and Fig. 4.6. $\phi_{\text{PIW}} = 0$ and $Q' = 0$, unless otherwise specified in the subfigures captions. The red cross in each subfigure is the working point in the simulations. Possible resonance lines up to the 16th order have been plotted on top of the tune footprint in each figure. A few labels were added to guide the reader. (**a**), (**b**), (**c**) displays the effect on the FMA for increasing beam-beam parameter. (**d**) displays a FMA when the crossing angle is weakly nonzero. (**e**) displays a FMA for a large crossing angle. (**f**) displays a FMA when the chromaticity is nonzero.

Chromaticity is often needed in modern colliders to mitigate collective instabilities. The crossing angle scan for the machine tunes of $(Q_x, Q_y) = (0.31, 0.32)$ was therefore repeated with a large chromaticity, $Q' = 15$, as is currently needed in the LHC, and the results are presented as functions of $\Delta Q_{\text{Tot}}(\phi_{\text{PIW}})$ in Fig. 4.6. This is thus directly comparable to Fig. 4.4b, from which the only difference is the nonzero chromaticity. The most evident effect is that the beam quality is worse preserved for small angles, $\phi_{\text{PIW}} \leq 0.1$, and large beam-beam tune shifts, $\xi_{\text{Tot}} \geq 0.02$. In fact, the

detrimental effects are worse with a nonzero chromaticity for all tested configurations. The peak LR_{Beam} has increased from $LR_{\mathrm{Beam}}(Q'=0) \leq 10\%/\mathrm{h}$ to $100\%/\mathrm{h}$, the peak emittance growth rate has increased from $\dot{\epsilon}_{\perp}(Q'=0) \leq 1\times10^{-7}\,/\mathrm{turn}$ to $5\times10^{-6}\,/\mathrm{turn}$, and the minimal *NADA* had decreased from $NADA(Q'=0) \geq 2.4\sigma_{\Sigma}$ to $1.3\sigma_{\Sigma}$. The beam quality preservation is still dependent on the angle, and the impact of the additional detrimental effects saturates around $\phi_{\mathrm{PIW}} \approx 1$.

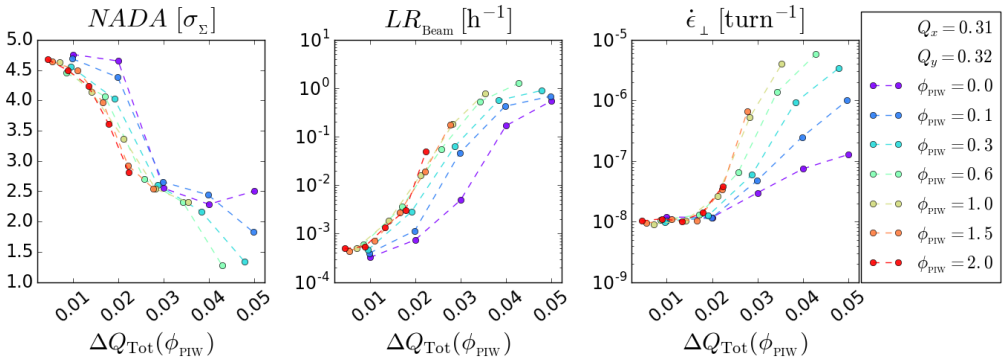

Figure 4.6: Beam quality reduction for different combinations of ϕ_{PIW} and ξ_{Tot}, when $Q_x = 0.31$, $Q_y = 0.32$, $Q' = 15$ and $\beta_q^* = 0.4\,\mathrm{m}$. The outputs *NADA*, LR_{Beam} and $\dot{\epsilon}_{\perp}$ have been calculated as expressed in Sec. 3.4. The outputs are presented as functions of $\Delta Q_{\mathrm{Tot}}(\phi_{\mathrm{PIW}})$.

The chromaticity has the effect that the tune of a particle oscillates in tune space, parallel to the diagonal, $Q_x = Q_y$, if Q' is equal in both planes. Effectively, particles far from resonance lines become affected by resonances, which is visible in the FMA in Fig. 4.5f, where the diffusion coefficient is large for a wider area around each plotted resonance line, than it was in the FMA in Fig. 4.5a. This oscillation is dependent on the energy variation, causing a mixing between the longitudinal and transverse planes, activating synchro-betatron resonances. The introduction of the longitudinal dof is able to increase the diffusion rate through Arnold diffusion. That is why the beam quality is so much less preserved for small Piwinski angles, $\phi_{\mathrm{PIW}} \leq 0.1$, compared to the case of zero chromaticity. The chromaticity does however not activate the odd resonances, as the crossing angle did, since it does not introduce a transverse asymmetry to the interaction. Furthermore, the effect of the chromaticity is caused by the lattice and not by the beam-beam interaction. These points may explain why there still is an increase in detrimental effects towards a saturation as the angle increases towards $\phi_{\mathrm{PIW}} \approx 1$.

The LHC is currently operating at the working point of $(Q_x, Q_y) = (0.31, 0.32)$, which preserves the beam quality well for small ξ_{Tot}. For larger ξ_{Tot} it was found in Sec. 4.1 that two alternative working points, $(0.315, 0.325)$ and $(0.475, 0.485)$, may give better preservation of the beam quality. The results from a crossing angle scan at the shifted working point, $(0.315, 0.325)$, are presented as functions of $\Delta Q_{\mathrm{Tot}}(\phi_{\mathrm{PIW}})$ in Fig. 4.7. The chromaticity is nonzero in these simulations, $Q' = 15$. There are multiple notable trends compared to the corresponding scan at the LHC working point. The beam quality is much better preserved for small angles, $\phi_{\mathrm{PIW}} \leq 0.1$, even for large beam-beam tune shifts, $\Delta Q_{\mathrm{Tot}}(\phi_{\mathrm{PIW}}) \leq 0.04$. For $\phi_{\mathrm{PIW}} \geq 0.3$ there is a sharp increase in LR_{Beam} and decrease in *NADA*. All three outputs support that this working point might be better than the LHC working point, except for the configurations with $\Delta Q_{\mathrm{Tot}}(\phi_{\mathrm{PIW}}) \leq 0.02$ and $\phi_{\mathrm{PIW}} \geq 0.3$, which indeed are the most relevant to describe the configurations in the LHC today.

With the shift of working point, other resonances may be important to understand the dynamics. The FMA for $\xi_{\mathrm{Tot}} = 0.04$, $Q' = 15$ and $\phi_{\mathrm{PIW}} = 0$ is presented in Fig. 4.8a. The 10th order resonance now affects particles at lower amplitude than at the LHC working point, and affects these less. The

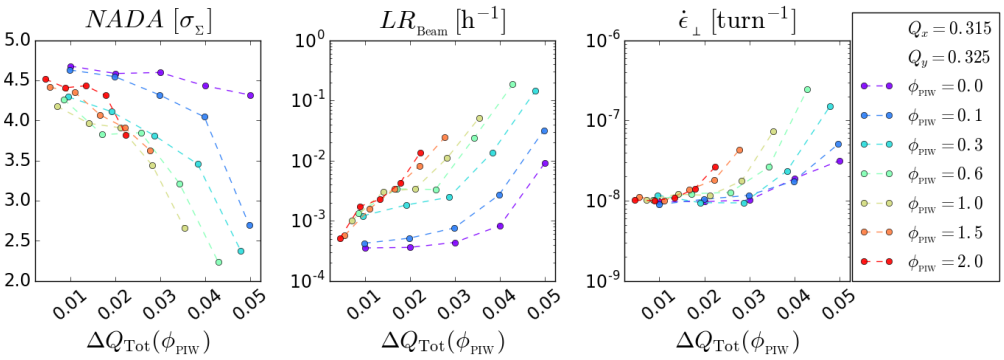

Figure 4.7: Beam quality reduction for different combinations of ϕ_{PIW} and ξ_{Tot}, when $Q_x = 0.315$, $Q_y = 0.325$, $Q' = 15$ and $\beta_q^* = 0.4\,\mathrm{m}$. The outputs $NADA$, LR_{Beam} and $\dot{\epsilon}_\perp$ have been calculated as expressed in Sec. 3.4. The outputs are presented as functions of $\Delta Q_{\mathrm{Tot}}(\phi_{\mathrm{PIW}})$.

16th order resonance is also active, but it affects mostly particles of low vertical amplitude that are not affected by the 10th order resonances simultaneously. This may explain why the beam quality is much better for this configuration at this working point. Note that the beam-beam tune shift is not equal to ξ_{Tot} for zero crossing angle. The nonzero longitudinal amplitude affects the maximum beam-beam tune shift. For a nonzero angle of $\phi_{\mathrm{PIW}} = 0.3$, the FMA changes significantly, as displayed in Fig. 4.8b. In addition to the 10th and 16th order resonances, also the 9th and 13th order resonances are active, and they overlap with the 16th order resonances for particles at large transverse amplitude. This is why there is a clear distinction between the cases of zero and nonzero crossing angle, based on the values for LR_{Beam} and $NADA$. The 9th, 13th and 16th order resonances are overlapping close to the working point, and will affect the footprint also for smaller $\Delta Q_{\mathrm{Tot}}(\phi_{\mathrm{PIW}})$. This is probably why this working point appears slightly worse for smaller ξ_{Tot} and large ϕ_{PIW}, than the LHC working point does.

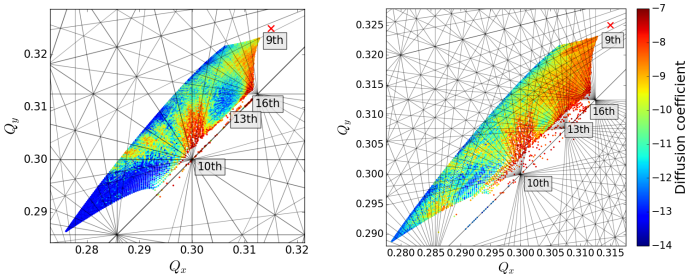

(a) $\xi_{\mathrm{Tot}} = 0.04$, $\phi_{\mathrm{PIW}} = 0$. **(b)** $\xi_{\mathrm{Tot}} = 0.04$, $\phi_{\mathrm{PIW}} = 0.3$.

Figure 4.8: FMAs illustrating activation of synchro-betatron resonances due to large chromaticity, $Q' = 15$, and odd resonances due to the crossing angle, for a working point of $(Q_x, Q_y) = (0.315, 0.325)$, related to the beam quality study in Fig. 4.7. The red cross in each subfigure is the working point in the simulations. Possible resonance lines up to the 18th order in (**a**) and 16th order in (**b**) have been plotted on top of the tune footprint in each figure. A few labels were added to guide the reader.

The results from a crossing angle scan for the machine tunes of $(Q_x, Q_y) = (0.475, 0.485)$, close to the half-integer resonance, for nonzero chromaticity, $Q' = 15$, are presented in Fig. 4.9 as functions of $\Delta Q_{\mathrm{Tot}}(\phi_{\mathrm{PIW}})$. A strange effect is that, for $\phi_{\mathrm{PIW}} = 0$, the beam quality seems better preserved for a stronger beam-beam interaction. The emittance growth rate is larger than expected from noise alone in 4 out of these 35 simulations, i.e. the presence of the beam-beam interaction appears to improve the situation in the core. This has been found to be an effect of the approximations in the model and is further discussed below. For tune shifts $\Delta Q_{\mathrm{Tot}}(\phi_{\mathrm{PIW}}) \leq 0.02$, the loss rate is larger for smaller crossing angles, which has not been observed at the two other working points. For larger tune shifts, the beam quality is again better preserved for a smaller crossing angle. Detrimental effects begin to reduce the beam quality for $\Delta Q_{\mathrm{Tot}}(\phi_{\mathrm{PIW}}) > 0.03$ and $\phi_{\mathrm{PIW}} \geq 0.6$. Nevertheless, this working point gives by far the best preservation of beam quality for the considered configurations.

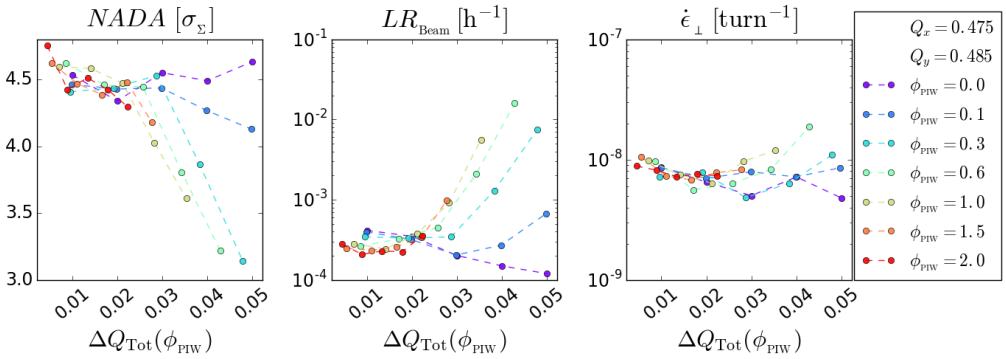

Figure 4.9: Beam quality reduction for different combinations of ϕ_{PIW} and ξ_{Tot}, when $Q_x = 0.475$, $Q_y = 0.485$, $Q' = 15$ and $\beta_q^* = 0.4\,\mathrm{m}$. The outputs $NADA$, LR_{Beam} and $\dot{\epsilon}_\perp$ have been calculated as expressed in Sec. 3.4. The outputs are presented as functions of $\Delta Q_{\mathrm{Tot}}(\phi_{\mathrm{PIW}})$.

The dependence on ξ_{Tot} and ϕ_{PIW} at a working point close to the half-integer resonance, is more challenging to understand than at the previous two working points. This is due to the vicinity of the half-integer resonance. The effect of reduced emittance growth rate for increasing ξ_{Tot} is particularly peculiar. The Poincaré section at the location where the noise is applied and collimation is performed, is slightly elongated along the p_x axis in the presence of strong beam-beam interaction, as displayed in Fig. 4.10. This distortion of phase space makes the effective diffusion weaker than if the distribution would be circular. Because the noise is meant to represent effects occurring at all places around the lattice, the reduced $\dot{\epsilon}_\perp$ is thus an artefact of the method. Indeed, the amplitude of the noise is generated relative to the initial beam divergence, and should be adjusted in configurations where the beam divergence is strongly affected by the nonlinearity. However, this effect is small, and the fact that the beam-beam interaction does not worsen the situation more than it does, demonstrates the good preservation of beam quality for this working point.

The results for machine tunes of $(Q_x, Q_y) = (0.475, 0.485)$ are affected by being so close to the half-integer resonance. The effect that a larger ϕ_{PIW} preserves better the beam quality for $\Delta Q_{\mathrm{Tot}}(\phi_{\mathrm{PIW}}) \leq 0.02$, remains to be understood. The extraordinary good behaviour for $\xi_{\mathrm{Tot}} = 0.05$ and zero crossing angle can be understood by the FMA of this configuration, displayed in Fig. 4.11a. There are only a few resonance lines that affect the footprint, whereof the 10th order resonance and the coupling resonance are measured to be the strongest, but there is no overlap between resonances. From the set of resonance lines up to order 17, that have been plotted on top of the footprint, there is in fact no possible overlap of low order resonances. The physics change for a nonzero crossing angle of $\phi_{\mathrm{PIW}} = 0.3$, as seen in the FMA in Fig. 4.11b. The odd resonances may affect this configuration,

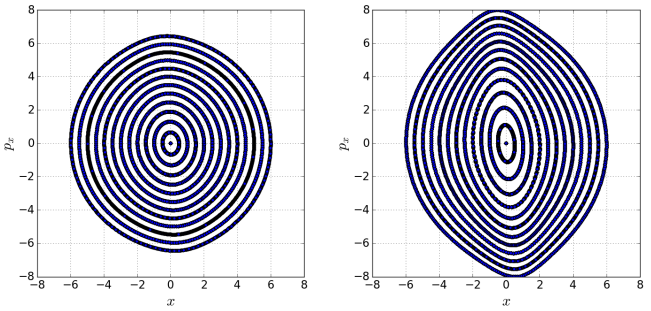

(a) $\xi_{\mathrm{Tot}} = 0.01$. **(b)** $\xi_{\mathrm{Tot}} = 0.05$.

Figure 4.10: Poincaré sections for $Q_x = 0.475$, for particles initially distributed along the x axis. Axes given in units of standard deviation.

which indeed they do. The 13th, 15th and 17th resonances all overlap with the resonances already present without the crossing angle. This causes the reduced preservation of beam quality that was measured for this configuration with a nonzero crossing angle. The beam quality was also found to remain good up to $\xi_{\mathrm{Tot}} = 0.03$ for $\phi_{\mathrm{PIW}} = 0.3$. The FMA of this configuration is displayed in Fig. 4.11c. As with the larger tune shift, the 15th and 17th order resonances are still active, but they cause much smaller diffusion coefficients for this combination, and it is again mainly the 10th order resonance that affects this footprint. The FMAs discussed here have all been made with zero chromaticity, $Q' = 0$, because the important effects were hidden behind a blur of large diffusion coefficients when the chromaticity was included. The beam-beam tune shift is smaller than ξ_{Tot} because of the half integer resonance.

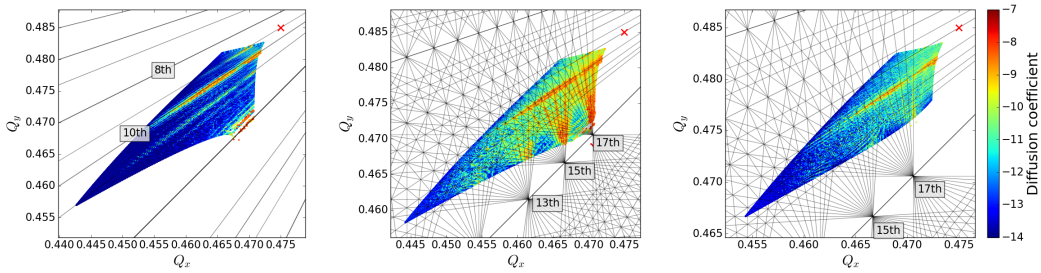

(a) $\xi_{\mathrm{Tot}} = 0.05$, $\phi_{\mathrm{PIW}} = 0$. **(b)** $\xi_{\mathrm{Tot}} = 0.05$, $\phi_{\mathrm{PIW}} = 0.3$. **(c)** $\xi_{\mathrm{Tot}} = 0.03$, $\phi_{\mathrm{PIW}} = 0.3$.

Figure 4.11: FMAs illustrating the activated resonances with and without a crossing angle for a working point of $(Q_x, Q_y) = (0.475, 0.485)$, without chromaticity, related to the beam quality study in Fig. 4.9. The red cross in each subfigure is the working point in the simulations. Possible resonance lines up to the 17th order have been plotted on top of the tune footprint in each figure. A few labels were added to guide the reader.

The results for the additional working points have only been presented with a strong chromaticity, $Q' = 15$, as this is both more realistic and pessimistic. It is a more relevant scenario to test, if one wants to find if either of these working points might be better suited than the current LHC working point, for a larger beam-beam parameter. The simulations have also been run with zero chromaticity. For $(Q_x, Q_y) = (0.315, 0.325)$ and $Q' = 0$, the worst values were found to be $NADA \geq 3.2$,

$LR_{\mathrm{Beam}} \leq 2 \times 10^{-2}\,\mathrm{h}^{-1}$, $\dot{\epsilon}_{\perp} \leq 2 \times 10^{-8}\,/\mathrm{turn}$, and in general better or similar to the corresponding simulations at the LHC working point. For $(Q_x, Q_y) = (0.475, 0.485)$ and $Q' = 0$, the worst values were found to be $\mathit{NADA} \geq 4.2$, $LR_{\mathrm{Beam}} \leq 5 \times 10^{-3}\,\mathrm{h}^{-1}$, $\dot{\epsilon}_{\perp} \leq 1 \times 10^{-8}\,/\mathrm{turn}$, and in general always better than for the corresponding simulations at the LHC working point.

The effect of a nonzero crossing angle has been studied in this section. The crossing angle activates odd betatron resonances, and causes a greater mixing between the longitudinal and transverse dof, leading to a worse preservation of the beam quality. The crossing angle also reduces the total beam-beam tune shift, which improves the preservation of beam quality. The second alternative working point, $(0.475, 0.485)$, is affected by few resonances for zero crossing angle, but odd resonances activated by a nonzero crossing angle affect the beam for large beam-beam tune shifts.

4.3 Hourglass Effect

The β function varies as a parabola close to the IPs, as given by Eq. (2.1). The transverse beam size therefore also varies over the beam-beam interaction, a variation called the hourglass effect. This variation is weak for configurations where $\sigma_s/\beta_q^* \ll 1$. For round beams, the total beam-beam tune shift is to first order independent of the value of β_q^*. The luminosity is however directly dependent on the transverse beam size, as given by Eq. (2.27), and a smaller β_q^* is preferred to achieve a higher luminosity. Squeezing β_q^* to small values is therefore done in all modern colliders, making the hourglass effect important as a side effect. Beam quality simulations for round beams have been run for the following studies with $\beta_q^* \in \{2.5, 4, 8, 10, 12, 14, 20, 30, 40, 60, 80, 160, 400\}$ cm, and nominal beam-beam parameters $\xi_{\mathrm{Tot}} \in \{0.01, 0.02, 0.03, 0.04, 0.05\}$. The simulations are run with $\sigma_s = 8\,\mathrm{cm}$ and zero crossing angle, making the total beam-beam tune shift approximately equal to ξ_{Tot}. The outputs from CABIN will be given as functions of σ_s/β_q^*, being smallest for the largest β_q^* and vice versa.

The results from a β_q^* scan at the LHC working point, $(Q_x, Q_y) = (0.31, 0.32)$, with zero chromaticity, are presented as functions of σ_s/β_q^* in Fig. 4.12a. The beam quality preservation is generally good, except for at large beam-beam parameters, $\xi_{\mathrm{Tot}} \geq 0.04$. A change occurs for $\sigma_s/\beta_q^* \geq 1$, for which the loss rates and emittance growth rates are increasing, and the *NADA* is decreasing. For $\xi_{\mathrm{Tot}} = 0.05$, there is a local optimum in all three outputs for $\sigma_s/\beta_q^* = 2/3$.

For small values of σ_s/β_q^* and zero crossing angle, the beam-beam interaction is the same for particles in the front and in the back of a bunch, i.e. the beam-beam interaction is therefore independent of the longitudinal dof. For large values of σ_s/β_q^*, the interaction depends strongly on the longitudinal position of the particle in the bunch. With more dof, the diffusion is in general larger, in agreement with the trend for large σ_s/β_q^* in Fig. 4.12a. This is further supported by the FMAs in Fig. 4.13. For $\beta_q^* = 4\,\mathrm{m}$, the 10th order resonance affects the motion of the particles strongly. The 14th and 16th order resonances are also noticeable. The FMA for $\beta_q^* = 2.5\,\mathrm{cm}$ displays that more particles are affected close to each resonance line in tune space. This is because the strong hourglass effect has caused significant mixing with the longitudinal dof, activating and driving the synchro-betatron resonances. Especially important for this working point are perhaps the resonance lines parallel to the coupling resonance, $Q_x = Q_y$. In addition, the particles far from any resonance line have a higher diffusion coefficient for the smallest β_q^*. That is why a stronger hourglass effect causes larger diffusion, both for particles at large and small transverse amplitudes. As a side note, the large σ_s/β_q^* has slightly increased the maximum tune shift. This behaviour is not within the scope of this thesis.

As discussed in Sec. 4.2, chromaticity is often needed in modern colliders to mitigate collective instabilities. The β_q^* scan for the LHC working point, $(Q_x, Q_y) = (0.31, 0.32)$, has been redone with a large chromaticity, $Q' = 15$, and the results are presented in Fig. 4.12b. With the nonzero chromaticity, the beam quality is significantly worse preserved for all configurations with

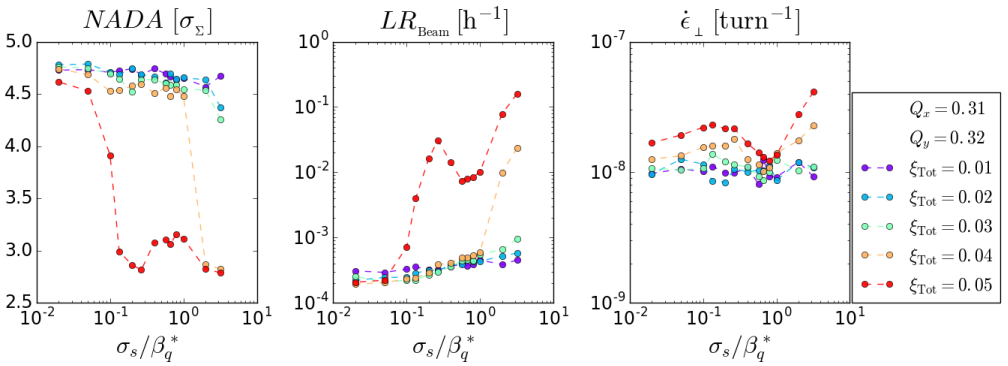

(a) $Q' = 0$.

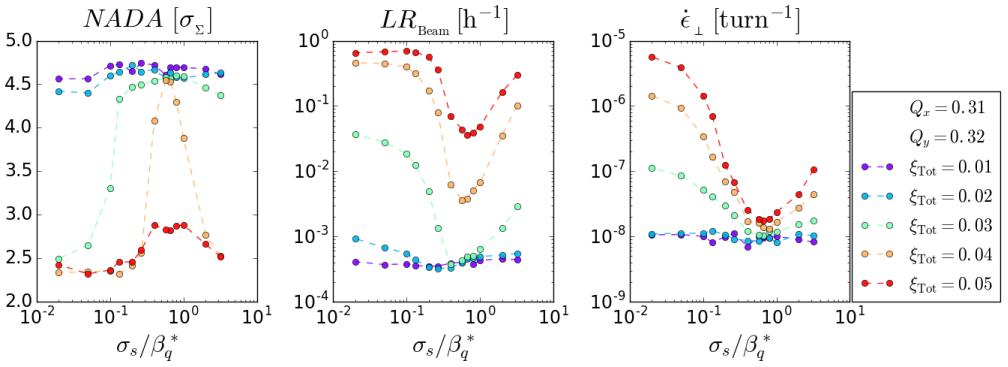

(b) $Q' = 15$.

Figure 4.12: Beam quality reduction for different combinations of β_q^* and ξ_{Tot}, when $Q_x = 0.31$, $Q_y = 0.32$, and $\phi_{\mathrm{PIW}} = 0$. The outputs *NADA*, LR_{Beam} and $\dot{\epsilon}_\perp$ have been calculated as expressed in Sec. 3.4 and presented as functions of σ_s/β_q^*. The chromaticity is $Q' = 0$ for the scan in (**a**), and 15 for the scan in (**b**).

$\xi_{\mathrm{Tot}} \geq 0.03$. The *NADA* has decreased and the emittance growth rate and beam loss rate have increased substantially by many orders of magnitude for large β_q^*, corresponding to a small σ_s/β_q^*. Also for large σ_s/β_q^*, the beam quality is worse preserved, but to a much weaker extent. This results in an optimum σ_s/β_q^* of approximately $2/3$, limited by the chromaticity from below and the hourglass effect from above. Configurations with smaller beam-beam parameters, $\xi_{\mathrm{Tot}} \leq 0.02$, do not have a strong dependence on σ_s/β_q^*. All these simulations seem negligibly affected by the beam-beam interaction.

The chromaticity causes a strong dependence of the tune on the longitudinal phase space. This activates the synchro-betatron resonances, driven by the beam-beam interaction, making the particles in tune space close to resonance lines affected. This is visualised by the FMA for $\beta_q^* = 4\,\mathrm{m}$ in Fig. 4.14a. The 10th and 16th order resonances have a strong impact, and the 14th order resonance is noticeable. That is why the beam quality is worse preserved for nonzero chromaticity and $\sigma_s/\beta_q^* \ll 1$. This behaviour was also expected for more significant hourglass effect. Instead, it seems that when the hourglass effect becomes significant, it reduces the strength of some resonances that strongly affect the dynamics in the presence of chromaticity, visualised by the FMA for $\beta_q^* = 12\,\mathrm{cm}$ in Fig. 4.14b. In comparison to the FMA for negligible hourglass effect, the dif-

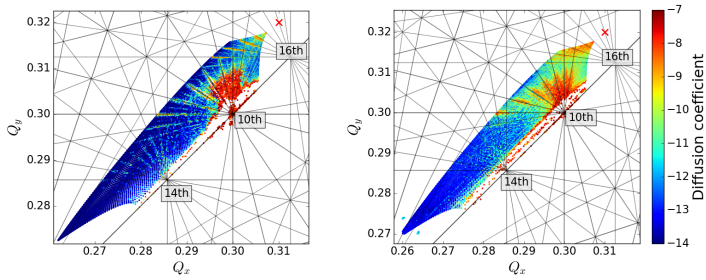

(a) $\beta_q^* = 4\,\mathrm{m}$. **(b)** $\beta_q^* = 2.5\,\mathrm{cm}$.

Figure 4.13: FMAs illustrating the effect of synchro-betatron resonances due to the hourglass effect and chromaticity, for a working point of $(Q_x, Q_y) = (0.31, 0.32)$, related to the beam quality study in Fig. 4.12a. Both simulations are run with zero chromaticity and a large beam-beam parameter, $\xi_{\mathrm{Tot}} = 0.05$. The red cross in each subfigure is the working point in the simulations. Possible resonance lines up to the 16th order have been added, in addition to a few labels meant to guide the reader.

fusion coefficients close to the resonance lines have for a significant hourglass effect been reduced substantially and the effect of the 14th order resonance is barely visible. The dynamical process causing this behaviour remains to be fully understood. Yet the hypothesis is supported by both the beam quality simulations and FMAs. The particles far from any resonance line have however a larger diffusion coefficient for significant hourglass effect. For even larger σ_s/β_q^*, the resonances driven by the hourglass effect will cause detrimental behaviour of the beam quality on its own. As noted above, this ability of the hourglass effect to battle the deterioration caused by the chromaticity, while also causing deterioration on its own, causes an optimum σ_s/β_q^*. These FMAs have been calculated with a smaller chromaticity, $Q' = 5$, because the chromaticity used in the beam quality simulations distorted the FMAs beyond the clear understanding needed for this discussion.

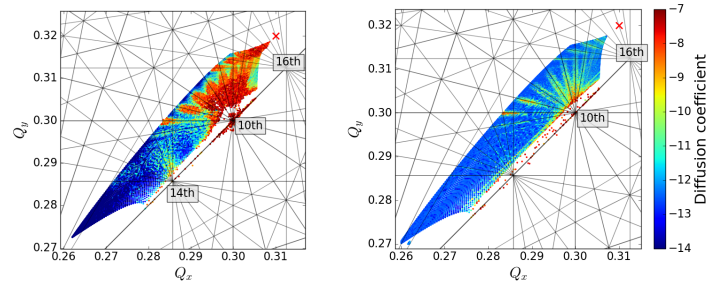

(a) $\beta_q^* = 4\,\mathrm{m}$. **(b)** $\beta_q^* = 12\,\mathrm{cm}$.

Figure 4.14: FMAs illustrating the effect of synchro-betatron resonances due to the hourglass effect, for a working point of $(Q_x, Q_y) = (0.31, 0.32)$, related to the beam quality study in Fig. 4.12b. Both simulations are run with a nonzero chromaticity, $Q' = 5$, and large beam-beam parameter, $\xi_{\mathrm{Tot}} = 0.05$. The red cross in each subfigure is the working point in the simulations. Possible resonance lines up to the 16th order have been added, including a few labels meant to guide the reader.

The results from a β_q^* scan with large chromaticity, $Q' = 15$, for the first alternative working point, $(Q_x, Q_y) = (0.315, 0.325)$, are presented as functions of σ_s/β_q^* in Fig. 4.15. The preservation of beam quality seems better for every presented configuration for this working point then at the LHC working point. The same results were also found for zero crossing angle in Sec. 4.2, because the odd resonances are not activated. The beam quality is worst preserved for the smallest value of σ_s/β_q^*, due to the chromaticity, as it was at the LHC working point. There is a weak trend that the *NADA* decreases and the growth and loss rates increase for σ_s/β_q^* larger than 1, caused by the hourglass effect. The combination of these to trends introduces an optimum σ_s/β_q^*, for β_q^* in the interval $[10, 30]$ cm. The interval for this optimum β_q^* is wider for this alternative working point than it was for the LHC working point.

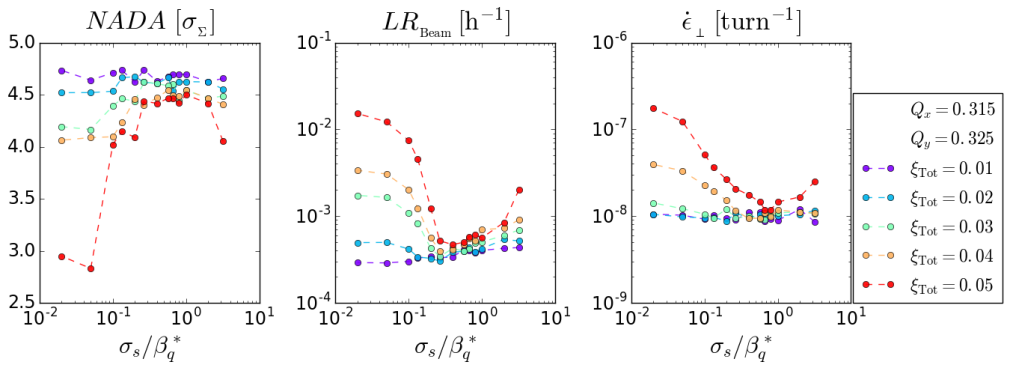

Figure 4.15: Beam quality reduction for different combinations of β_q^* and ξ_{Tot}, when $Q_x = 0.315$, $Q_y = 0.325$, $Q' = 15$ and $\phi_{\mathrm{PIW}} = 0$. The outputs *NADA*, LR_{Beam} and $\dot{\epsilon}_\perp$ have been calculated as expressed in Sec. 3.4. The outputs are presented as functions of σ_s/β_q^*.

The results from a β_q^* scan with large chromaticity, $Q' = 15$, for the second alternative working point, $(Q_x, Q_y) = (0.475, 0.485)$, are presented as functions of σ_s/β_q^* in Fig. 4.16. The preservation of beam quality is better for every presented configuration for this working point than at the LHC working point, except for when the beam-beam parameter is small, $\xi_{\mathrm{Tot}} \leq 0.02$, and σ_s/β_q^* is large. For $\sigma_s/\beta_q^* \geq 0.4$, the loss rate increases and the *NADA* decreases significantly, more than the corresponding values for $(Q_x, Q_y) = (0.315, 0.325)$, but the emittance growth rate remains close to the value expected from noise alone, $\dot{\epsilon}_0 = 1 \times 10^{-8}$ /turn. The low emittance growth rate, $\dot{\epsilon}_\perp < \dot{\epsilon}_0$, was partially explained in Sec. 4.2. The preservation of beam quality is close to optimal for $\sigma_s/\beta_q^* < 0.4$. The good preservation for negligible hourglass effect reduces the visibility of a possible local optimum in the interval $\beta_q^* \in [20, 30]$ cm for small beam-beam parameters, $\xi_{\mathrm{Tot}} \leq 0.02$.

The general good behaviour at the alternative working point $(Q_x, Q_y) = (0.475, 0.485)$ for zero crossing angle, was already found in Sec. 4.2. FMAs for $\xi_{\mathrm{Tot}} = 0.03$ and zero chromaticity are given in Fig. 4.17. For negligible hourglass effect, $\beta_q^* = 4$ m, there are no resonance lines crossing in the relevant tune area, the 10th order resonance is the strongest. The total beam-beam tune shift is smaller than ξ_{Tot}. The resonances are affecting the footprint. For a strong hourglass effect, $\beta_q^* = 2.5$ cm, the beam-beam tune shift is closer to ξ_{Tot}. The 10th order resonance is strong, but so are the synchro-betatron resonances parallel to the coupling resonance. These are crossing for particles at large amplitude, possibly causing the large loss rate and small *NADA*, combined with a small emittance growth rate. In addition, the strong hourglass effect causes slightly increased diffusion coefficients for particles far from any of the considered resonance lines.

The hourglass effect does become noticeable both in FMAs and in beam quality simulations as $\sigma_s/\beta_q^* \geq 1$. It drives synchro-betatron resonances, and generally reduces the beam quality. In this

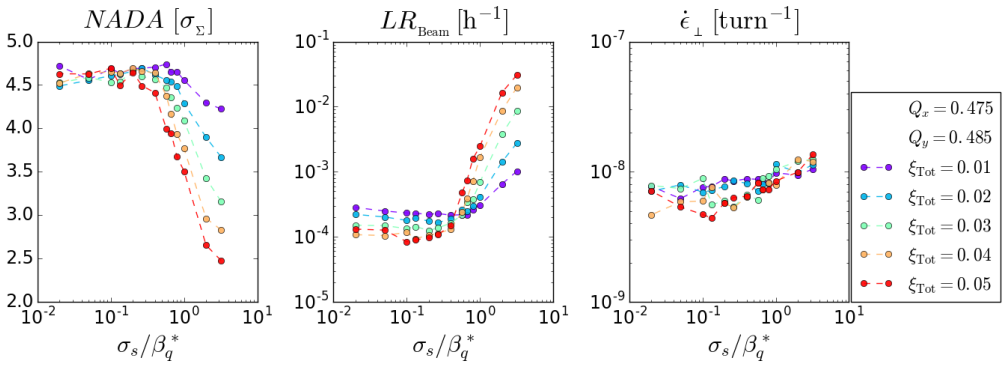

Figure 4.16: Beam quality reduction for different combinations of β_q^* and ξ_{Tot}, when $Q_x = 0.475$, $Q_y = 0.485$, $Q' = 15$ and $\phi_{\mathrm{PIW}} = 0$. The outputs $NADA$, LR_{Beam} and $\dot{\epsilon}_\perp$ have been calculated as expressed in Sec. 3.4. The outputs are presented as functions of σ_s/β_q^*.

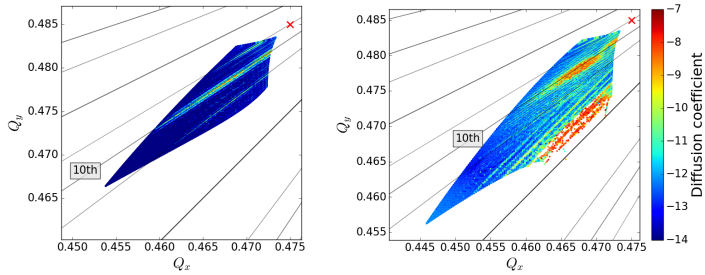

(a) $\beta_q^* = 4\,\mathrm{m}$. **(b)** $\beta_q^* = 2.5\,\mathrm{cm}$.

Figure 4.17: FMAs illustrating the effect of synchro-betatron resonances due to the hourglass effect, for a working point of $(Q_x, Q_y) = (0.475, 0.485)$, related to the beam quality study in Fig. 4.16. Both simulations are run with zero chromaticity and large beam-beam parameter, $\xi_{\mathrm{Tot}} = 0.03$. The red cross in each subfigure is the working point in the simulations. Possible resonance lines up to the 16th order have been added, including a few labels meant to guide the reader.

section, it has on the other hand been found that the dependence on s of the beam-beam interaction, i.e the hourglass effect, manages to limit the detrimental effects caused by the chromaticity. This creates an optimal intermediate value for σ_s/β_q^*, dependent on the working point and beam-beam parameter. The study in this section has not taken into account the combined effect of including a crossing angle. That is done in Sec. 4.6, studying the dependence on chromaticity.

4.4 Separation

There are 4 IPs where the beams can collide in the LHC, hosting experiments with different luminosity requirements (ATLAS, LHCb, CMS, ALICE). It is convenient to control the luminosity at the different IPs, so that the experiments can share the same beam. Such convenience will likely be needed also in future projects. This can be achieved by separating the beams at the IP in the plane transverse to the crossing angle, i.e. if the beams are crossing horizontally, they are separated vertically. The crossing scheme in these simulations is both with and without crossing angle HV

(horizontal in the first IP, vertical in the other), and the separation scheme is thus VH. Improving the beam quality preservation by separating the beams transversally works in principle because the beam-beam interaction is weaker at larger amplitudes. That is why the collimation in CABIN is done at $5\sigma_\Sigma$, where σ_Σ is the transverse beam size of the strong beam in the relevant direction. It was displayed in Fig. 2.9 that a separation of $10\sigma_\Sigma$ reduces the beam-beam tune shift for particles of zero transverse amplitude by a factor 50.

To not reduce the luminosity to zero, the relevant separations are of only a few σ_Σ. Such separations change the nonlinear force completely, and it is therefore necessary to do numerical simulations to find out if the separation has a beneficial impact on the beam quality preservation. At larger separations, it is assumed that the impact of the beam-beam interaction will decrease. Beam quality simulations for round beams have been run for each of the following studies, with separations $\Delta x_\perp \in \{0, 0.25, ..., 2, 3, ..., 10\} \cdot \sigma_\Sigma$, large chromaticity, $Q' = 15$, and nominal beam-beam parameters $\xi_{\mathrm{Tot}} \in \{0.01, 0.02, 0.03, 0.04, 0.05\}$. The goal of this study is both to see the impact of a small separation, and to see how large separation is needed to make the impact of the beam-beam interaction negligible.

The results for a separation scan with zero crossing angle, are presented as functions of the separation $\Delta x_\perp$ in Fig. 4.18a. For a separation of $4\sigma_\Sigma$, the emittance growth rate for all beam-beam parameters has converged to the value expected from noise alone, $\dot{\epsilon}_0 = 1 \times 10^{-8}$ /turn. For a separation of $6\sigma_\Sigma$, the beam loss rate and the *NADA* have converged to good values. At lower amplitudes, the loss rate and emittance growth rate both oscillate with local peaks at separations of approximately $0.5\sigma_\Sigma$ and $1.5\sigma_\Sigma$. This is in agreement with an earlier study [47]. The emittance growth rate does not increase for a small offset for small beam-beam parameters, $\xi_{\mathrm{Tot}} < 0.03$. The loss rate increases by approximately a factor 7 for $\xi_{\mathrm{Tot}} = 0.02$ as the separation increases from 0 to $0.75\sigma_\Sigma$.

The same scan was repeated with a nonzero Piwinski angle, $\phi_{\mathrm{PIW}} = 1$, and the results are presented as functions of the separation in Fig. 4.18b. The emittance growth rate converges at approximately $\Delta x_\perp = 4\sigma_\Sigma$, and the loss rate and *NADA* converges at $6\sigma_\Sigma$. For small separations, the worst beam quality preservation occurs on the interval $\Delta x_\perp \in [0.25, 1.5] \cdot \sigma_\Sigma$. The behaviour in this interval is smoother with a nonzero crossing angle, and the increased deterioration is small compared to zero separation.

The worse preservation of beam quality at low, nonzero separation, is due to the activation of odd resonances, as visualised by the FMA in Fig. 4.19a. Both the 7th and the 13th order resonances affect the motion of the particles. The 7th order resonance does not affect the particles for $\xi_{\mathrm{Tot}} = 0.03$, because the tune shift from the working point is not large enough, which is why the emittance growth rate is not larger for a small separation for this beam-beam parameter. Because the resonances are partially activated by the nonzero Piwinski angle as well, as was visualised by the FMAs (**b**) and (**d**) in Fig. 4.5, a small separation is less detrimental if the bunches are already colliding with a crossing angle. The oscillating behaviour for a small separation with zero crossing angle may be interpreted as the effect of specific resonances acting on different parts of the beam distribution due to the strongly varying shape of the tune footprint, exemplified in Fig. 4.19. The details of this behaviour are outside the scope of this thesis.

The emittance growth rate is largely caused by the diffusion of particles in the core, while the loss rate and *NADA* reflects what happens at large amplitudes. Consider again the shape of the force from a round beam of transverse beam size σ_r in Fig. 2.6. For a transverse separation of $5\sigma_r$, the particles of approximately zero transverse amplitude always experience the weak force at $5\sigma_r$, independent of the betatron phase. The particles at large transverse amplitudes up to $5\sigma_r$ will oscillate between 0 and $10\sigma_r$, experiencing at times the strongly nonlinear force in the core of the strong beam. This explains the convergence of emittance growth rate at a lower transverse separation than the convergence of the loss rate and the *NADA*. The beam-beam tune shift is greatly

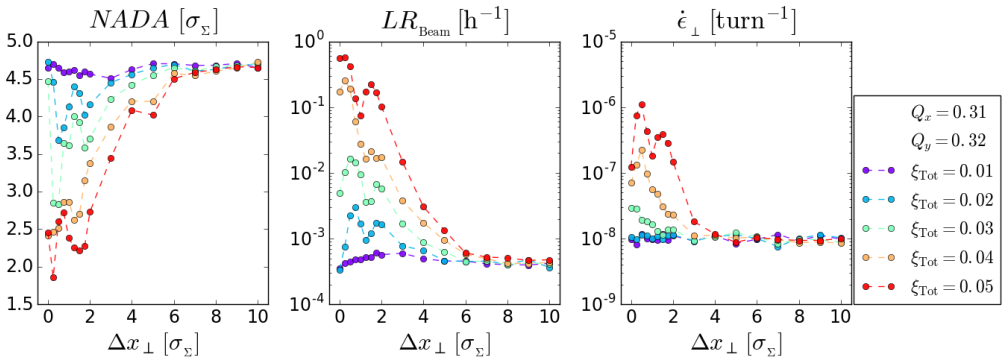

(a) $\phi_{\mathrm{PIW}} = 0.$

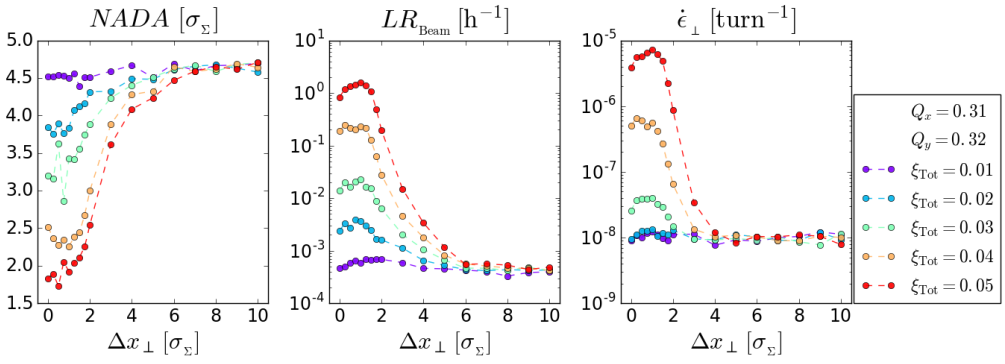

(b) $\phi_{\mathrm{PIW}} = 1.$

Figure 4.18: Beam quality reduction for multiple combinations of a transverse separation at the IPs, $\Delta x_\perp$, and ξ_{Tot}, when $Q_x = 0.31$, $Q_y = 0.32$, $\beta_q^* = 40\,\mathrm{cm}$ and $Q' = 15$. The outputs *NADA*, LR_{Beam} and $\dot{\epsilon}_\perp$ have been calculated as expressed in Sec. 3.4. The outputs are presented as functions of $\Delta x_\perp$.

reduced for a separation of $4\sigma_\Sigma$, as visualised in the FMA in Fig. 4.19b, and is of opposite sign of the beam-beam parameter for the particles of lowest amplitude, in agreement with Fig. 2.9. To see what amplitudes are affected by resonances, the diffusion coefficients have also been given as functions of the initial transverse amplitude in Fig. 4.19c. The resonances affect only particles at large transverse amplitudes, in agreement with the negligible effect on the emittance growth rate. For larger separation, the beam-beam tune shift decreases further, and the resonances affect only particles at even larger amplitudes, causing the *NADA* and the loss rate to converge.

It has been found that a separation of $4\sigma_\Sigma$ almost cancels the impact of the beam-beam interaction on particles of zero transverse amplitude in the core of the bunch. Similarly, a separation of $6\sigma_\Sigma$ almost cancels the impact of the beam-beam interaction on particles in the tail of the bunch. Separations are used to reduce the luminosity in an experiment. A separation of less than 2σ, does not necessarily improve the beam quality. If a small separation is needed to achieve the required reduction of luminosity, one could suggest achieving this reduction by increasing the crossing angle instead. Increasing the crossing angle would improve the beam quality, given that it increases from an already significant value, as detailed in Sec. 4.2.

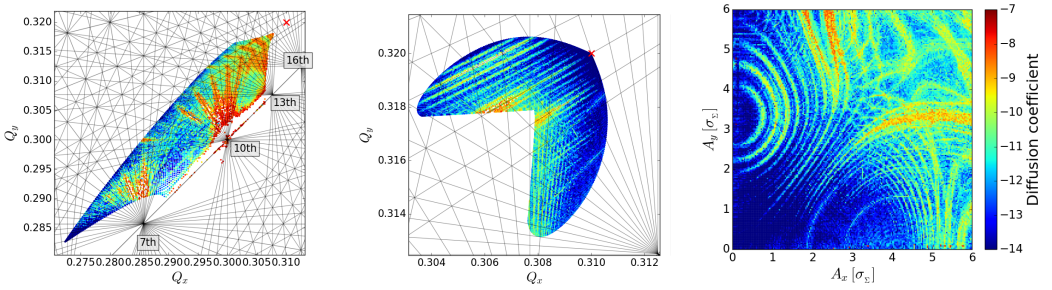

(a) $\Delta x_\perp = 0.25\sigma_\Sigma$. **(b)** $\Delta x_\perp = 4\sigma_\Sigma$. **(c)** $\Delta x_\perp = 4\sigma_\Sigma$.

Figure 4.19: FMAs illustrating the activated resonances and size of tune footprint with small and large transverse separation, $\Delta x_\perp$, for a working point of $(Q_x, Q_y) = (0.31, 0.32)$. Both simulations are run with zero chromaticity and large beam-beam parameter, $\xi_{\mathrm{Tot}} = 0.04$. (**a**) displays the FMA for a small separation. (**b**) displays the FMA for a large separation, and the same values are plotted in initial amplitude space, (A_x, A_y), in (**c**). The red cross in the tune plots is the working point in the simulations. Possible resonance lines up to the 16th order have been plotted on top of the tune footprints. A few resonance labels were added in (**a**) to guide the reader.

4.5 Intermediate Phase Advance

The working point has a strong impact on the preservation of beam quality, as studied extensively in Sec. 4.1. The tune in either transverse plane is the average phase advance per turn. The focus in this section is the impact of the intermediate phase advance between the two IPs in the model. A study found analytically for 2D phase space that certain resonances could be cancelled by setting $\mu_1 = \pi/2$ [6]. However, a phase error of more than 0.001 could be sufficient to lose the cancellation effect. From a symmetry perspective, it was also suggested that the intermediate phase advance $\mu_1 = \mu/2$ could cancel resonances. A phase difference, $|\mu_1 - \mu_2| = 0.0002$, was found to completely destroy the cancellation. Another study claimed that the best beam quality preservation was experienced with the symmetric phase advance, without commenting on the required accuracy [10].

Beam quality simulations have been run for configurations with different intermediate phase advances, $\Delta\mu_1 \in \{-0.03, -0.025, -0.02, -0.018, ..., 0.02, 0.025, 0.03\} \cdot 2\pi$, close to the phase advances introduced above, nominal beam-beam parameters $\xi_{\mathrm{Tot}} \in \{0.03, 0.04, 0.05\}$, and large chromaticity, $Q' = 15$. The difference, $\Delta\mu_1$, from the design phase advance, $\pi/2$ or $\mu/2$, is kept equal in the horizontal and vertical plane. Because the goal is to study how much the beam quality preservation improves, and how accurately the intermediate phase advance must be set, only the largest beam-beam parameters have been simulated. Only the results at the LHC working point, $(0.31, 0.32)$, will be presented. FMAs for zero intermediate phase advance for this configuration with $\xi_{\mathrm{Tot}} = 0.03$, and both zero and nonzero crossing angle, are repeated in Fig. 4.20. The 10th and 16th order resonances are disturbing the particle motion for zero crossing angle, while for nonzero crossing angle, the odd 7th and 13th order resonances are also activated. These are the resonances one wants to suppress for the LHC working point.

The results from a scan in intermediate phase advance close to $\mu/2$ for zero crossing angle, are presented as functions of $\mu_1 - \mu/2$ in Fig. 4.21. The best preservation of beam quality is achieved when $\mu_1 = \mu_2$. The emittance growth rate decreases to $\dot{\epsilon}_0 = 1 \times 10^{-8}$ /turn, expected from noise alone, and similarly the loss rate and *NADA* reach excellent values. The accuracy in μ_1 needed to achieve this improvement seems dependent on the beam-beam parameter, larger ξ_{Tot} requires a more accurate intermediate phase advance to achieve the full improvement.

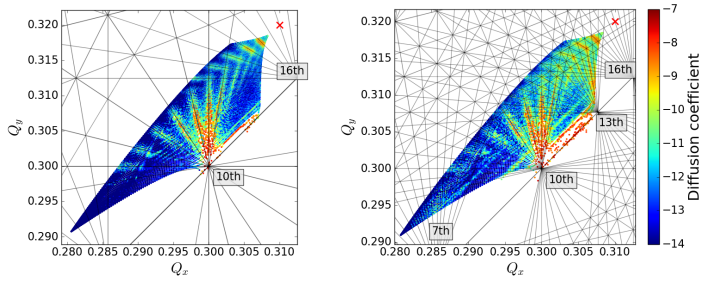

(a) $\phi_{\text{PIW}} = 0$. **(b)** $\phi_{\text{PIW}} = 0.1$.

Figure 4.20: FMAs illustrating resonances for zero intermediate phase advance, $\mu_1 = 0$, for a working point of $(Q_x, Q_y) = (0.31, 0.32)$, $Q' = 0$ and $\xi_{\text{Tot}} = 0.03$. The red cross in each subfigure is the working point in the simulations. Possible resonance lines up to the 16th order have been added. A few labels were added to guide the reader.

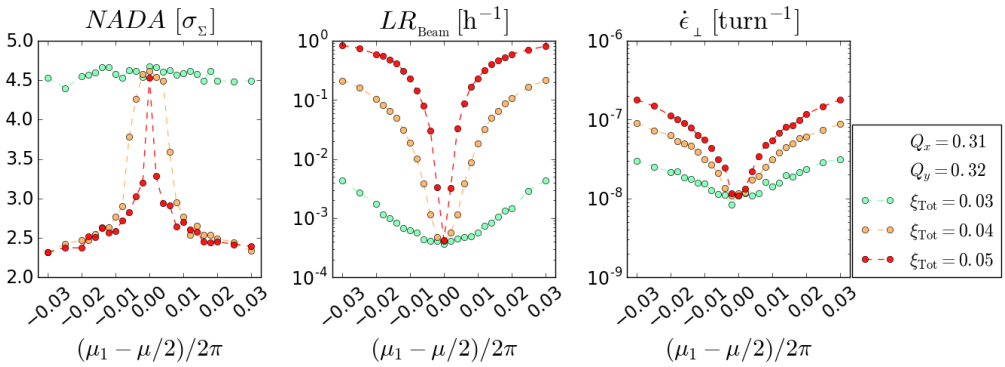

Figure 4.21: Beam quality improvement for intermediate phase advance close to $\mu/2$, for different values of ξ_{Tot}, when $Q_x = 0.31$, $Q_y = 0.32$, $\phi_{\text{PIW}} = 0$ and $Q' = 15$. The outputs $NADA$, LR_{Beam} and $\dot{\epsilon}_\perp$ have been calculated as expressed in Sec. 3.4. The outputs are presented as functions of the intermediate phase advance.

The beam quality was preserved very well for $\mu_1 = \mu_2$, which is supported by the FMA in Fig. 4.22a. There are few resonances affecting the particles. This improvement can be understood from a symmetry argument. With equal phase advances, and equal modelling of the beam-beam interaction in the two IPs, the model represents effectively a collider with a single IP at a working point at $(Q_x, Q_y) = (0.155, 0.16)$. The total beam-beam tune shift would then be half of what it is in the original configuration. This configuration has been simulated, and the FMA is presented in Fig. 4.22b, supporting the argument. Both simulations have been run with the same synchrotron tune, $Q_s = 0.002$, explaining the discrepancy close to the coupling resonance. For a nonzero chromaticity, the FMAs are effectively unchanged. The 10th and 16th order resonances affect the motion of the particles for $|\mu_1 - \mu_2| = 0.0002$, as visible in the FMA in Fig. 4.22c. The beam quality simulations are less sensitive to the phase error than what the resonance coefficients are.

The scan in intermediate phase advance close to $\mu/2$ has been repeated with a nonzero crossing angle, $\phi_{\text{PIW}} = 1$. The results are presented as functions of $\mu_1 - \mu/2$ in Fig. 4.23. The best preservation of beam quality is again achieved when $\mu_1 = \mu_2$. The improvement on the emittance growth

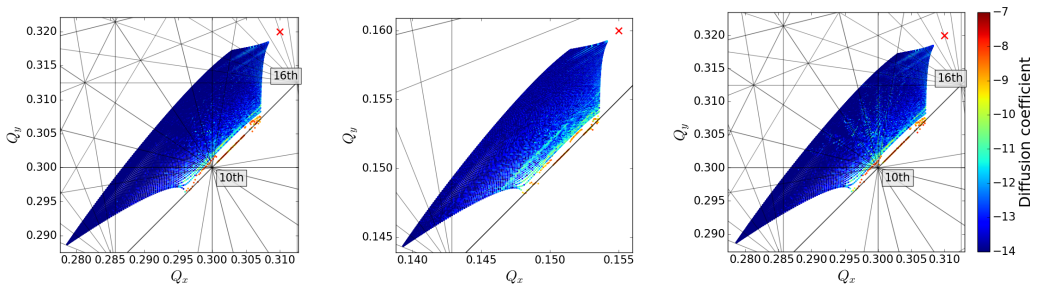

(a) $\mu_1 = \mu/2$. **(b)** 1 IP. **(c)** $|\mu_1 - \mu_2| = 0.0002$.

Figure 4.22: FMAs illustrating cancelling of resonances using an intermediate phase advance close to $\mu_1 = \mu/2$, for a working point of $(Q_x, Q_y) = (0.31, 0.32)$, $\phi_{\text{PIW}} = 0$, $Q' = 0$ and $\xi_{\text{Tot}} = 0.03$. The red cross in each subfigure is the working point in the simulations. Possible resonance lines up to the 16th order have been added, in addition to a few labels meant to guide the reader. $\mu_1 = \mu/2$ in (**a**). (**b**) is run with a single IP at half the machine tunes, $(0.155, 0.16)$. A small phase error is introduced in (**c**).

rate and loss rate is approximately a factor 4, but only for $\xi_{\text{Tot}} \geq 0.04$. Compared to the scan with zero crossing angle, the improvement by using the intermediate phase advance $\mu/2$ is significantly reduced for this crossing angle.

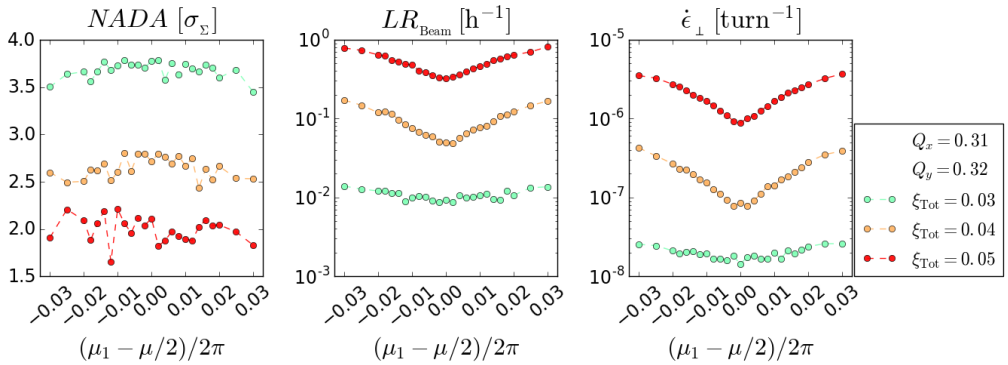

Figure 4.23: Beam quality improvement for intermediate phase advance close to $\mu/2$, for different values of ξ_{Tot}, when $Q_x = 0.31$, $Q_y = 0.32$, $\phi_{\text{PIW}} = 1$ and $Q' = 15$. The outputs $NADA$, LR_{Beam} and $\dot{\epsilon}_\perp$ have been calculated as expressed in Sec. 3.4. The outputs are presented as functions of the intermediate phase advance.

The improvement from using the intermediate phase advance $\mu/2$ was significantly reduced when a nonzero crossing angle was included. It was found in Sec. 4.2 that a nonzero crossing angle activates odd resonances. Furthermore, with one horizontal and one vertical crossing, the symmetry is broken and therefore the lattice is no longer equivalent to a shorter lattice with a single IP. This argumentation is supported by the FMA in Fig. 4.24. The effect of the 10th order resonance is still strongly reduced, and the 16th order is invisible. The 7th and 13th order resonances do not seem affected by the symmetric intermediate phase advance. Hence, the improvement from use of this intermediate phase advance is limited.

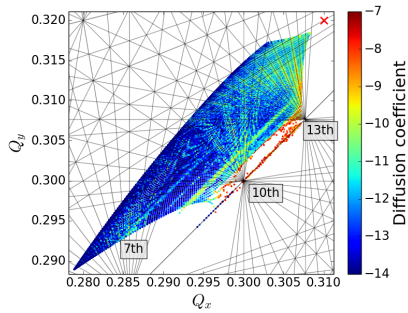

Figure 4.24: FMA illustrating cancelling of resonances using the intermediate phase advance $\mu_1 = \mu/2$, for a working point of $(Q_x, Q_y) = (0.31, 0.32)$, $\phi_{\text{PIW}} = 0.1$, $Q' = 0$ and $\xi_{\text{Tot}} = 0.03$. The red cross marks the working point in the simulation. Possible resonance lines up to the 15th order have been added, in addition to a few labels meant to guide the reader.

The results from a scan in intermediate phase advance close to $\pi/2$, for zero crossing angle, are presented as functions of $\mu_1 - \pi/2$ in Fig. 4.25. The best preservation of beam quality is achieved when $\mu_1 = 0.512 \cdot \pi$, not at $\mu_1 = \pi/2$. The optimum phase advance has been found to be dependent on the working point. The emittance growth rate decreases to $\dot{\epsilon}_0 = 1 \times 10^{-8}$ /turn, expected from noise alone, and similarly the loss rate and *NADA* also reach excellent values. The accuracy needed to achieve this improvement seems dependent on the beam-beam parameter, larger ξ_{Tot} requires a more accurate μ_1 to achieve the full improvement.

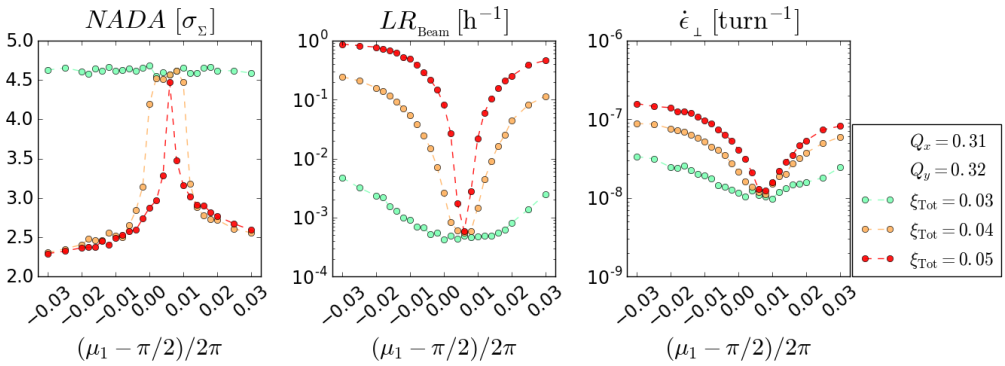

Figure 4.25: Beam quality improvement for intermediate phase advance close to $\pi/2$, for different values of ξ_{Tot}, when $Q_x = 0.31$, $Q_y = 0.32$, $\phi_{\text{PIW}} = 0$ and $Q' = 15$. The outputs *NADA*, LR_{Beam} and $\dot{\epsilon}_\perp$ have been calculated as expressed in Sec. 3.4. The outputs are presented as functions of the intermediate phase advance.

The theory applied to achieve the resonance cancelling condition, $\mu_1 = \pi/2$, was for a 2D transverse phase space only. That is, either horizontal or vertical, not both. The derivation was also to first order only, assuming that the beam-beam interaction was weak. This assumption has possibly been broken by the beam-beam parameters considered in this section. The choice $\mu_1 = \pi/2$ was supposed to cancel resonances of order $\{2, 6, 10, 14, 18, ...\}$. It was found in part 1 of this project that individual resonances were cancelled effectively by intermediate phase advances chosen in this manner [1]. For resonances dependent on both transverse phase space planes, it seems that $\pi/2$ is not the optimal choice. This is supported by the FMAs in Fig. 4.26. The 10th order resonance has

less impact on the motion of the particles for $\mu_1 = \pi/2$ than for zero intermediate phase advance, but the impact is even weaker for $\mu_1 = 0.512 \cdot \pi$. There are still moderate diffusion coefficients close to the 10th order resonance lines, partly because the 20th order resonance cannot be cancelled by this method. The cancellation of the resonances is not as good as with the symmetric phase advance. However, it is important to keep in mind that the FMA can only give a qualitative understanding of the beam dynamics, and in particular the impact of the resonances on the beam quality. Compared to the symmetric phase advance, the beam quality simulations did show an equally good improvement in preservation of beam quality, and similar required accuracy in maintaining μ_1.

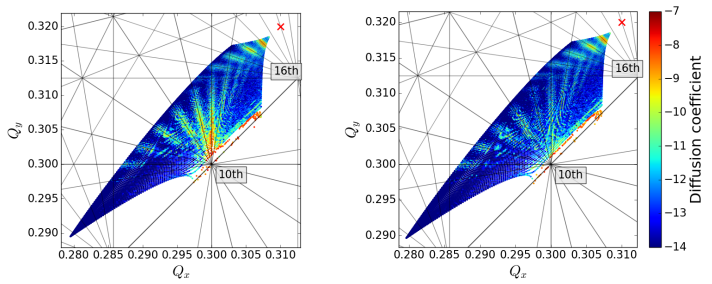

(a) $\mu_1 = \pi/2$. **(b)** $\mu_1 = 0.512 \cdot \pi$.

Figure 4.26: FMAs illustrating cancelling of resonances using an intermediate phase advance close to $\mu_1 = \pi/2$, for a working point of $(Q_x, Q_y) = (0.31, 0.32)$, $\phi_{\text{PIW}} = 0$, $Q' = 0$ and $\xi_{\text{Tot}} = 0.03$. The red cross in each subfigure is the working point in the simulations. Possible resonance lines up to the 16th order have been added, in addition to a few labels meant to guide the reader.

The scan in intermediate phase advance close to $\pi/2$ has been repeated with a nonzero crossing angle, $\phi_{\text{PIW}} = 1$. The results are presented as functions of $\mu_1 - \pi/2$ in Fig. 4.27. There is an optimum intermediate phase advance, but it is slightly larger than $\pi/2$, as it was for zero crossing angle. The improvement due to the phase advance is only detectable for $\xi_{\text{Tot}} \geq 0.04$. For these beam-beam parameters the emittance growth rate and loss rate is approximately a factor 2 smaller, while the *NADA* remains unchanged. Compared to the scan with zero crossing angle, the improvement by using the optimum intermediate phase advance $0.512 \cdot \pi$ is insignificant for this crossing angle. The improvement was better for nonzero crossing angle with the symmetric intermediate phase advance, $\mu/2$.

The modest improvement from using $\mu_1 \approx \pi/2$ can be understood based on similar arguments as discussed above. The choice of intermediate phase advance does not affect the odd resonances. The tunes close to $\pi/2$ only reduce the effect of the 10th order resonance, not the 7th, 13th or 16th. This is supported by the FMAs for a small crossing angle in Fig. 4.28. The impact of the 10th order resonance is reduced modestly by an intermediate phase advance $\pi/2$, but it is reduced better by $0.512 \cdot \pi$. The 13th and 16th order resonances are still overlapping for particles at large amplitudes. However, even if there is an improvement visible in these FMAs for $\xi_{\text{Tot}} = 0.03$, there is no improvement for these intermediate phase advances according to the beam quality simulations.

In this section, it has been shown that a smart choice of intermediate phase advance can reduce the effect of certain resonances from the LHC working point, $(Q_x, Q_y) = (0.31, 0.32)$. Similar behaviours have been found for the alternative working points $(0.315, 0.325)$ and $(0.475, 0.485)$. The postulated intermediate phase advance $\mu/2$ was an optimum, while $\pi/2$ is slightly inaccurate according to the simulations. The strict requirement on the accuracy in setting $\mu_1 = \mu_2$ based on resonance coefficients [6], has been reproduced with FMAs. It has however been found that even though the resonances are activated, they may not affect the beam quality substantially. The

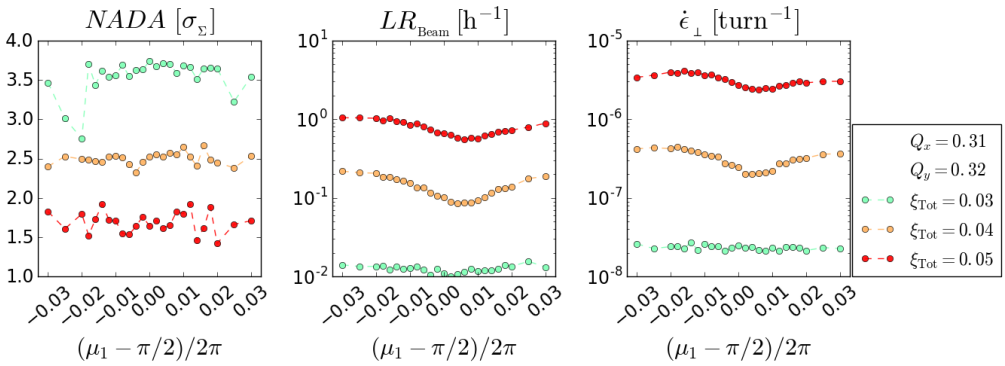

Figure 4.27: Beam quality improvement for intermediate phase advance close to $\pi/2$, for different values of ξ_{Tot}, when $Q_x = 0.31$, $Q_y = 0.32$, $\phi_{\mathrm{PIW}} = 1$ and $Q' = 15$. The outputs $NADA$, LR_{Beam} and $\dot{\epsilon}_\perp$ have been calculated as expressed in Sec. 3.4. The outputs are presented as functions of the intermediate phase advance.

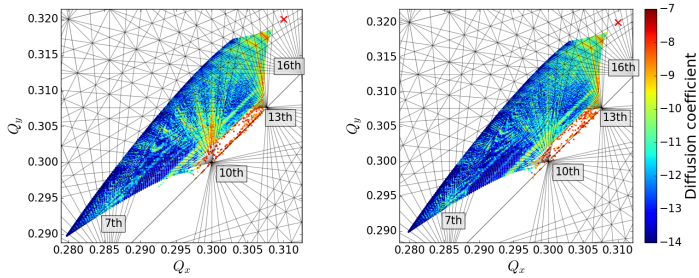

(a) $\mu_1 = \pi/2$. **(b)** $\mu_1 = 0.512 \cdot \pi$

Figure 4.28: FMAs illustrating cancelling of resonances using an intermediate phase advance close to $\mu_1 = \pi/2$, for a working point of $(Q_x, Q_y) = (0.31, 0.32)$, $\phi_{\mathrm{PIW}} = 0.1$ $Q' = 0$ and $\xi_{\mathrm{Tot}} = 0.03$. The red cross in each subfigure is the working point in the simulations. Possible resonance lines up to the 16th order have been added, in addition to a few labels meant to guide the reader.

required precision is several orders of magnitude less strict, $\Delta\mu_1 \sim 0.01$, based on beam quality simulations, although it is strongly dependent on the beam-beam parameter. If one were to use this method in a collider, one would likely require continuous monitoring of the intermediate phase advance while the machine is running. The introduction of odd resonances from crossing angles, and most likely also from a small separation or long-range interactions, cannot be overcome by setting the intermediate phase advance. Hence the preservation of beam quality is improved only marginally for realistic configurations in current circular hadron colliders.

4.6 Chromaticity

Chromaticity is often needed in modern colliders to mitigate collective instabilities. It has been found in previous sections that the chromaticity causes a strong mixing between the longitudinal and transverse coordinates, activating synchro-betatron resonances parallel to the betatron resonance lines in tune space. This increases the number of particles affected by each resonance. It

has also been found that a moderate hourglass effect seems to reduce the detrimental effects caused by the chromaticity. In this section, the quantitative dependence on chromaticity will be tested for negligible and moderate hourglass effect with zero and nonzero crossing angle. Beam quality simulations for round beams have been run for each of the following studies at the LHC working point, $(Q_x, Q_y) = (0.31, 0.32)$, with $Q' \in \{0, 1.25, ..., 5, 7.5, ..., 20\}$, and nominal beam-beam parameters $\xi_{\mathrm{Tot}} \in \{0.01, 0.02, 0.03, 0.04, 0.05\}$.

The results from a chromaticity scan with negligible hourglass effect, $\sigma_s/\beta_q^* = 0.02$, and zero crossing angle, $\phi_{\mathrm{PIW}} = 0$, are presented as functions of Q' in Fig. 4.29. It seems that the emittance growth rate increases approximately exponentially with the chromaticity. The loss rate also increases fast from a threshold chromaticity, dependent on the beam-beam parameter, to an apparent maximum value of approximately $70\%\ \mathrm{h}^{-1}$. Similarly, the *NADA* decreases fast from a threshold chromaticity. In the simulations with largest loss rate, approximately 7% of the weak beam is lost. The weak-strong model is approaching its limit of validity.

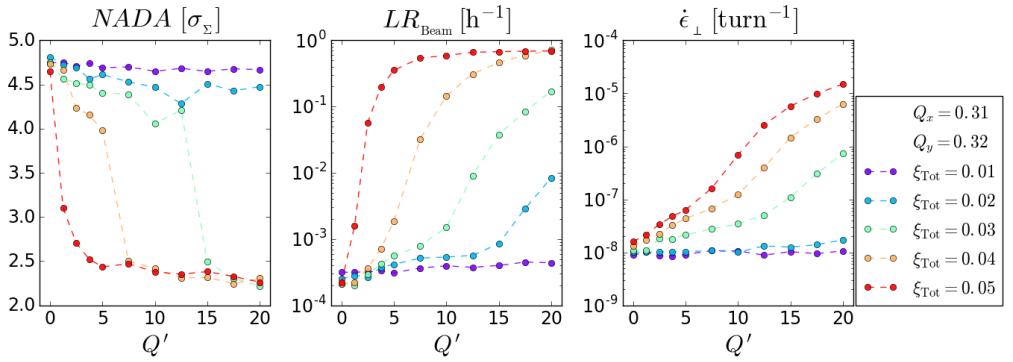

Figure 4.29: Beam quality reduction for multiple combinations of the chromaticity, Q', and the beam-beam parameter, ξ_{Tot}, when $Q_x = 0.31$, $Q_y = 0.32$, $\beta_q^* = 4\,\mathrm{m}$ and $\phi_{\mathrm{PIW}} = 0$. The outputs *NADA*, LR_{Beam} and $\dot{\epsilon}_\perp$ have been calculated as expressed in Sec. 3.4. The outputs are presented as functions of Q'.

The chromaticity scan with zero crossing angle, $\phi_{\mathrm{PIW}} = 0$, was repeated with a significant hourglass effect, $\sigma_s/\beta_q^* = 2/3$, and the results are presented as functions of Q' in Fig. 4.30. The emittance growth rate seems again approximately exponential, but growing much slower with Q' than for a negligible hourglass effect. The *NADA* and loss rate also behave similarly for large chromaticities as with negligible hourglass effect, with a fast decrease and increase respectively towards a limit after a threshold chromaticity, dependent on the beam-beam parameter. The difference is that the onset of detrimental effects begins at larger chromaticity for a certain beam-beam parameter. For moderate beam-beam parameters, $\xi_{\mathrm{Tot}} \leq 0.03$, and as large chromaticity as is usual in the LHC, $Q' = 15$, there seems to be no increase in detrimental effects beyond what is caused by the noise alone. For the largest beam-beam parameter, $\xi_{\mathrm{Tot}} = 0.05$, there also seems to be a cancellation of the detrimental effects caused by the hourglass effect at $Q' = 0$, for a small nonzero chromaticity. This behaviour produces an optimum chromaticity, being approximately $Q' = 3.75$ for this configuration.

The crossing angle and the odd resonances that it activates has been found to reduce the preservation of beam quality. Especially the resonance cancellation by smart choice of intermediate phase advance was rendered practically worthless when the crossing angle was included in Sec. 4.5. The scans of chromaticity have thus been repeated with a significant crossing angle, $\phi_{\mathrm{PIW}} = 1$. The scan with negligible hourglass effect, $\sigma_s/\beta_q^* = 0.02$, is presented in Fig.4.31. Compared to the scan with

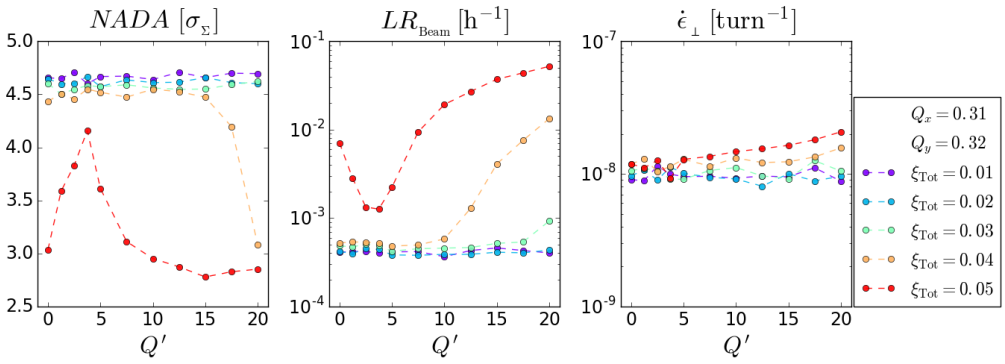

Figure 4.30: Beam quality reduction for multiple combinations of the chromaticity, Q', and the beam-beam parameter, ξ_{Tot}, when $Q_x = 0.31$, $Q_y = 0.32$, $\beta_q^* = 12\,\mathrm{cm}$ and $\phi_{\mathrm{PIW}} = 0$. The outputs $NADA$, LR_{Beam} and $\dot{\epsilon}_\perp$ have been calculated as expressed in Sec. 3.4. The outputs are presented as functions of Q'.

zero crossing angle and negligible hourglass effect, it seems that for small chromaticities, the beam quality is preserved worse with the crossing angle, while for large chromaticities, it is preserved better. One clear difference is that for $\xi_{\mathrm{Tot}} = 0.03$, there is no significant emittance growth rate even for the largest chromaticity. That the preservation is worse for small chromaticities can be understood from knowing that the crossing angle activates the odd resonances and the synchro-betatron resonances. The improvement for large chromaticities can be understood from knowing that the crossing angle also reduces the total beam-beam tune shift.

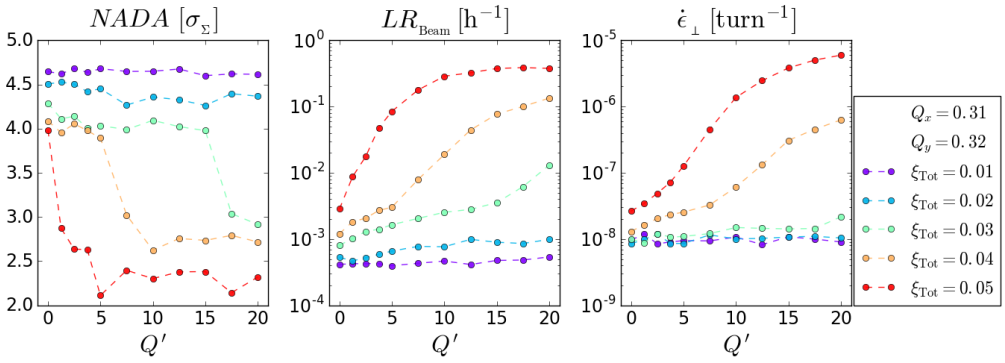

Figure 4.31: Beam quality reduction for multiple combinations of the chromaticity, Q', and the beam-beam parameter, ξ_{Tot}, when $Q_x = 0.31$, $Q_y = 0.32$, $\beta_q^* = 4\,\mathrm{m}$ and $\phi_{\mathrm{PIW}} = 1$. The outputs $NADA$, LR_{Beam} and $\dot{\epsilon}_\perp$ have been calculated as expressed in Sec. 3.4. The outputs are presented as functions of Q'.

The chromaticity scan with large crossing angle, $\phi_{\mathrm{PIW}} = 1$, was repeated with a significant hourglass effect, $\sigma_s/\beta_q^* = 2/3$, and the results are presented as functions of Q' in Fig. 4.32. Note that this Piwinski angle for a smaller value of β_q^* corresponds to a smaller actual crossing angle. The emittance growth rate seems again approximately exponential, but growing much more slowly with Q' than for a negligible hourglass effect. The emittance growth rate for zero chromaticity is largest for this configuration with both the moderate hourglass effect and the crossing angle. The $NADA$

and loss rate behave similarly as without the crossing angle. Both begin to reach worse values after a threshold chromaticity, which depends on the beam-beam parameter. The *NADA* and the loss rate also become worse more slowly than for the negligible hourglass effect. For moderate beam-beam parameters, $\xi_{\mathrm{Tot}} \leq 0.03$, and as large chromaticity as is usual in the LHC, $Q' = 15$, there seems to be only a small increase in detrimental effects beyond what is caused by the noise alone. For the largest beam-beam parameters, $\xi_{\mathrm{Tot}} \geq 0.04$, there also seems like the detrimental effects caused by the hourglass effect and crossing angle when $Q' = 0$, is somewhat reduced when a small nonzero chromaticity is included. This behaviour produces an optimum chromaticity, being approximately $Q' = 2.5$ for this configuration.

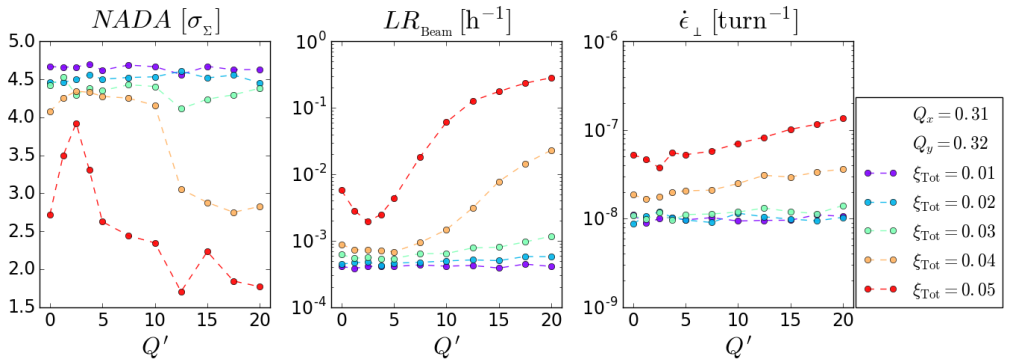

Figure 4.32: Beam quality reduction for multiple combinations of the chromaticity, Q', and the beam-beam parameter, ξ_{Tot}, when $Q_x = 0.31$, $Q_y = 0.32$, $\beta_q^* = 12\,\mathrm{cm}$ and $\phi_{\mathrm{PIW}} = 1$. The outputs *NADA*, LR_{Beam} and $\dot{\epsilon}_\perp$ have been calculated as expressed in Sec. 3.4. The outputs are presented as functions of Q'.

The detrimental effect of chromaticity, and the reduction thereof by a moderate hourglass effect, has been studied in this section. The behaviour is assumed to be linked to how the two effects alternate in affecting the incoherent particles as the latter perform synchrotron rotations. The hourglass effect is felt more strongly for large longitudinal displacement, s, while the chromaticity affects the particles more strongly for large energy deviation, δ. This alternation with the synchrotron motion is assumed to disturb the resonances from building up periodically over time. Exactly how this mechanism works remains to be understood. Unlike the smart choice of phase advance, the improvement from this effect seems to remain after activation of odd resonances with a crossing angle.

4.7 Comparison to LHC

A dedicated experiment was performed in the LHC to study the limitations due to strong head-on beam-beam interactions, and no long-range interactions [48, 49]. The experiment tested collisions at different working points between individual bunches of higher intensity and smaller normalised emittance than the ones produced for regular operation with bunch trains. This resulted in a large total beam-beam tune shift just below 0.02. The experiment found that the loss rate depended strongly on the working point, which was moved along the diagonal close to the LHC working point. The parameters of the LHC were fixed with the standard setup of the 2017 run, except for the different working points. The particles were colliding in IP1 and IP5 only, with alternating full crossing angle of $\theta_{\mathrm{xing}} = 280\,\mu\mathrm{rad}$ with $\beta_q^* = 0.4\,\mathrm{m}$. The chromaticity was moderate, $Q' = 7$. Different sensors were able to measure the horizontal and vertical normalised emittance, and the

intensity of the bunches, as they evolved during the experiment. Based on these values, the beam-beam parameter can be calculated by Eq. (2.47). The necessary values are given in App. E.

The configurations of the bunches that were acted upon by the strongest beam-beam interaction have been simulated by CABIN, and the results will be presented in this section. Each working point was tested in a limited window, making the emittance measurements erroneous. Therefore, only the loss rates will be compared. This experiment was run over two fills in the LHC. The first fill began at $(0.311, 0.318)$, whereupon the tunes were decreased simultaneously parallel to the diagonal, for both the weak and the strong beam. The second fill began at $(0.311, 0.319)$, whereupon the tunes where increased one at a time, only for the weak beam. To use the implementations for the round beam-beam interaction, the average of the horizontal and vertical emittances has been used. To use the 4D implementation, the beam-beam parameter has been reduced by a factor S as in Eq. (2.85).

The loss rates that were measured in the LHC, and are presented in Tab. E.1, are visualised in Fig. 4.33a. The luminosity burn-off has been calculated to be approximately 5%, which has been set as the lower limit of the colour scale. The circles and stars correspond to the first and second fill respectively. Even resonance lines up to 14th order are plotted on top of this tune space, with width proportional to the strength of the resonance coefficient c_n in Eq. (2.58). The loss rate is large for working points close to the 10th order resonance, $Q_x \leq 0.302$. The loss rate is also large in the opposite end, for the working point $(0.317, 0.328)$. This appears to possibly be caused by the 14th order resonance, $4Q_x + 10Q_y = 2$. Because there is a nonzero crossing angle, it could also be caused by the 7th order resonance $2Q_x + 5Q_y = 1$. There are also quite large loss rates close to $(0.309, 0.316)$. This might be caused by a combination of the 13th and 16th order resonances. The smallest loss rate was measured at a working point of $(0.315, 0.324)$. This optimal working point is further up the diagonal than the LHC working point, in agreement with the discussion on optimal working points for larger beam-beam tune shifts in Sec. 4.1. Details of the execution of the experiment can be found in the sources [48, 49].

The configurations were simulated with the round 4D beam-beam implementation in CABIN, using the average emittance of the strong beam and the reduced beam-beam parameter due to the crossing angle. The calculated loss rates are presented in Fig. 4.33b. For the working points close to the 10th order resonance, $Q_x \leq 0.305$, the calculated loss rates are high, comparable to the experimental values. The code calculates high loss rates for working points further from the 10th order resonance than what was measured in the experiment. For larger horizontal tunes, $Q_x > 0.305$, the round 4D beam-beam implementation does not calculate high loss rates for any configuration. Note that the maximum loss rate distinguishable by colour among the simulated values is 8%, which is larger than for the experimental values, after subtraction of the luminosity burn-off.

The configurations were also simulated with the round 6D beam-beam implementation, using the average emittance of the strong beam. The calculated loss rates are presented in Fig. 4.33c. For the working points close to the 10th order resonance at $Q_x \leq 0.305$, the calculated loss rates are high, as they were for the 4D implementation. For larger horizontal tunes, $Q_x > 0.305$, the round 6D beam-beam implementation calculates loss rates similar to the experimental values. The loss rate of $0.05\,\mathrm{h}^{-1}$, in addition to the luminosity burn-off, has been reproduced for the working point $(0.317, 0.328)$. Furthermore, the minimal loss rate has been reproduced at the working point close to $(0.315, 0.323)$. Also, the larger loss rate at $(0.311, 0.319)$, compared to $(0.311, 0.322)$, has been reproduced.

The configuration was also simulated using the not averaged, measured emittances for the strong beam, with the flat 6D beam-beam implementation. The calculated loss rates are presented in Fig. 4.33c. With this implementation, the large loss rates close to the 10th order resonance are measured for even larger horizontal tunes, $Q_x \leq 0.306$. For larger horizontal tunes, $Q_x > 0.306$, the dependence on the working point is similar to the values calculated by the round 6D implementation, and thus also similar to the experimental values. The loss rates for large vertical tunes,

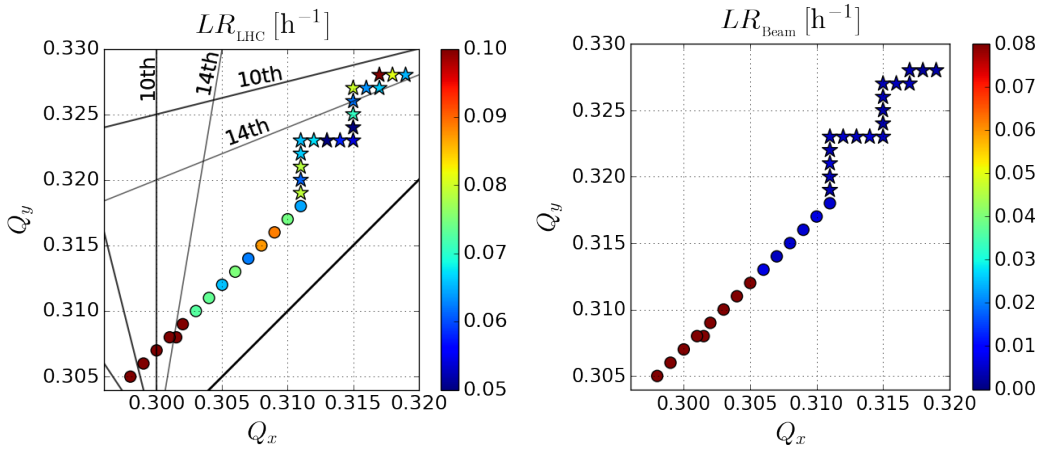

(a) LHC.

(b) 4D Round.

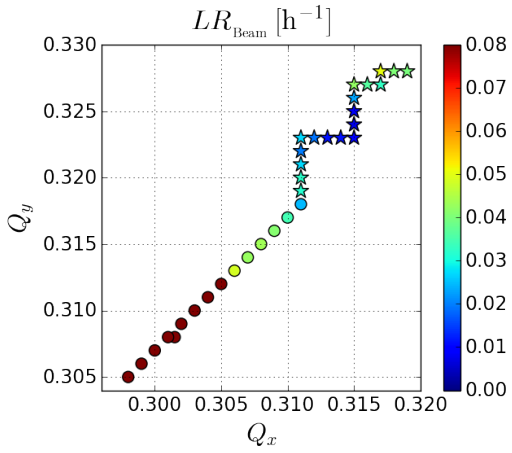

(c) 6D Round.

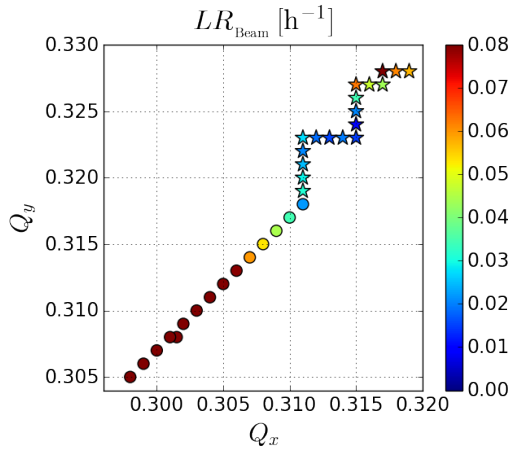

(d) 6D Flat.

Figure 4.33: Loss rates measured in the LHC in (**a**), and loss rates calculated by CABIN for the same configurations using the different implementations of the beam-beam interaction. The luminosity burn-off has been estimated to $5\%\ \mathrm{h}^{-1}$ for these configurations, used as the minimum value of the colour scale of the values measured in the LHC.

$Q_y \geq 0.327$, are larger for the flat implementation than for the round 6D implementation and the experimental values.

Before discussing the results in detail, the main differences between the LHC and the model in CABIN will be repeated. The luminosity burn-off is not included in the code, but it has been taken into account with a shift of the colour scale for the experimental values. The lattice has in the code been reduced to a rotation in phase space, and errors of different sources in the lattice have not been modelled. The normalised noise level in the simulations have been set to $\Delta_q = 10^{-4}$, in units of the beam divergence. This noise level corresponds to a larger emittance growth rate than is common in the LHC. Due to irregularities with the stability feedback system, this noise level is possibly reasonable. With a smaller normalised rms noise level of $10^{-4.5}$, the loss rates are reduced

by a few $\%$, but the general dependence on the working point is kept. Finally, the collimation is done differently in the LHC and in CABIN. The particles are considered lost at a lower transverse amplitude in the code than in the machine, because the effect of the beam-beam interaction falls off quickly for large amplitudes, and because higher order lattice errors have not been implemented.

One clear discrepancy is the high loss rates from the simulations for $Q_x \in [0.303, 0.305]$. It seems like the simulations are affected by the detrimental effects from the 10th order resonances close to $Q_x = 0.3$ at larger horizontal tunes than are measured in the LHC. One cause of this discrepancy could be the difference in collimation, the code counts particles as lost at lower amplitudes than where they actually are lost. Particles at $5\sigma_\Sigma$ have tunes further from the working point than particles at $6\sigma_\Sigma$, as was detailed in Fig. 2.10. Collimating at the larger amplitude has been found to push the limit for large loss rates down to $Q_x = 0.303$, but this also reduces the loss rates in the configurations far from the 10th order resonance to practically zero. Close to the 10th order resonance, it seems that the beam-beam interaction is the limiting factor also at larger amplitudes, but elsewhere the limit of $5\sigma_\Sigma$ is needed. Another possible cause is that the measured emittances in the machine during the experiment were erroneous. The beam-beam tune shift was also measured, and this measurement suggested that the emittances of the strong beam were underestimated by 20% to 30%, which leads to an overestimation of the beam beam-beam tune shifts of beam 1 [48]. The difference between the values calculated with the round and flat beam implementations will be discussed below.

There is a large difference between the loss rates calculated with the 4D implementation and the 6D implementations, for working points with $Q_x > 0.306$. The difference comes from the inability of the 4D implementation to model the effect of the crossing angle and the mixing with the longitudinal dof. This is most clear for the loss rates calculated at the working point $(0.318, 0.323)$, for which the FMAs with the round 4D and 6D implementations are displayed in Fig. 4.34. The FMA simulations were run for the same configurations as the beam quality simulations, but with zero noise and zero chromaticity. Simulations were run for the round 6D implementation with both zero initial longitudinal amplitude, $A_s = 0$, and a significant initial longitudinal amplitude, $A_s = 1\sigma_s$. First of all, the reduction of the beam-beam parameter for the 4D model does reduce the length of the tune footprint, but it also reduces the width of the footprint, as the crossing angle does not do to the same extent. More importantly, in the FMA for the 4D implementation in Fig. 4.34a, the most visible resonances are the 14th, 16th and 18th order resonances, but not one of these produces large diffusion coefficients. The FMA for the 6D implementation with zero longitudinal amplitude in Fig. 4.34b, shows that many odd ordered resonances have been activated by the crossing angle. The 14th and 18th order resonance lines with zero crossing angle are replaced by the 7th and 9th order resonance lines. The 16th order resonance lines are not replaced by 8th order resonance lines, and do not produce larger diffusion coefficients. When the particles have a longitudinal amplitude, the FMA for the 6D implementation in Fig. 4.34c is completely different, due to a stronger mixing with the longitudinal dof. The synchro-betatron resonances parallel to the diagonal cut through the footprint. The low order resonances produce larger diffusion coefficients for particles at large amplitudes, giving large loss rates. Without the crossing angle, there are only even order resonances and no synchro-betatron resonances visible without mixing with the longitudinal plane. The 4D model is thus not able to correctly model the behaviour at these working points, for which the beams can be affected strongly by odd resonances.

There is a small difference between the round and the flat 6D implementations as well. Some of these differences are within the $\sim 10\%$ deviation in the simulation results itself, due tot the limited number of macroparticles. The possibly most crucial difference is in the limit on Q_x for large loss rates close to the 10th order resonance. The difference is in part understandable from the FMAs for the configuration at the working point $(0.306, 0.313)$ with zero chromaticity in Fig. 4.35. The strong beam has a smaller vertical than horizontal normalised emittance, $\epsilon_{n,x2} > \epsilon_{n,y2}$, making the

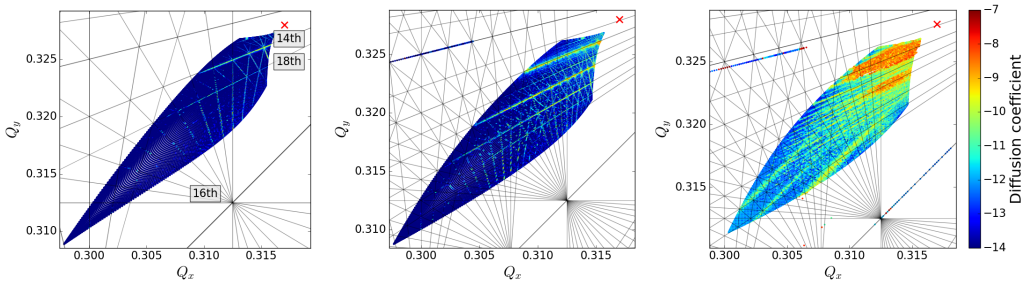

(a) 4D Round, $A_s = 1\sigma_s$. **(b)** 6D Round, $A_s = 0$. **(c)** 6D Round, $A_s = 1\sigma_s$.

Figure 4.34: FMAs illustrating the difference between the effect of the 4D and the 6D implementation of round beam-beam interaction, for a working point of $(Q_x, Q_y) = (0.317, 0.328)$. The red cross in each subfigure is the working point in the simulations. Possible resonance lines up to the 18th order in (**a**) and 16th order in (**b**) and (**c**) have been plotted on top of the tune footprint in each subfigure. A few labels were added in (**a**) to guide the reader.

beam squeezed in the vertical direction and the beam-beam tune shift longer in the vertical tune than in the horizontal tune, in agreement with Eq. (2.47). In effect, the tune footprint with the flat implementation is shifted towards the coupling resonance. The impact on the FMA is limited, but it seems that the 10th order resonance is able to affect more particles for the flat implementation. The total tune shift is also slightly larger for the flat implementation than the round implementation. This is caused by taking an average of the emittances when modifying the values of the strong bunch to be able to use a round beam-beam implementation. The stronger beam-beam interaction with a tune footprint shifted towards the diagonal may explain the difference between the results acquired with the flat and round implementations. If the measured emittances were correct, the flat beam implementation would model the physics most accurately. Due to the large inaccuracy of the measured emittances, it is possible that the values used for the round 6D implementation are closer to the real values during the experiment.

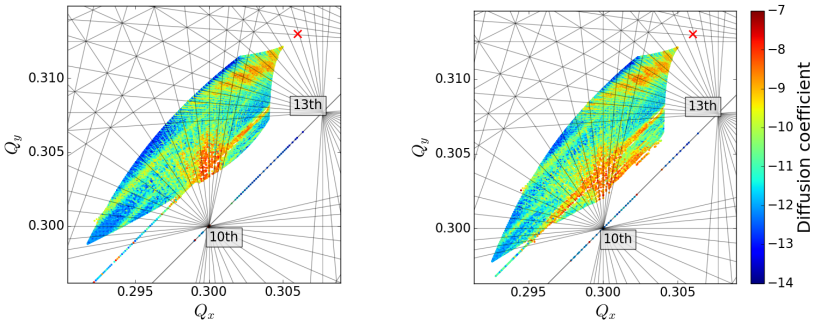

(a) 6D Round. **(b)** 6D Flat.

Figure 4.35: FMAs illustrating the difference between the effect of the round and the flat beam-beam interaction, for a working point of $(Q_x, Q_y) = (0.306, 0.313)$. The red cross in each subfigure is the working point in the simulations. Possible resonance lines up to the 16th order have been plotted on top of the tune footprint in each figure. A few labels were added to guide the reader.

4.8 Maximum Beam-Beam Tune Shift

To achieve higher luminosity, one also has to increase the strength of the beam-beam interaction. The stronger the beam-beam interaction is, the larger the beam-beam tune shift is. One recent paper stated that there is no fundamental limit until $\Delta Q_{\mathrm{Tot}}(\phi_{\mathrm{PIW}}) = 0.2$ for perfect beam-beam interactions between round beams [10]. This is not a realistic limit. Beam quality simulations have been run for different configurations at the LHC working point, $(0.31, 0.32)$, and the alternative working points, $(0.315, 0.325)$ and $(0.475, 0.485)$, in search of a maximum acceptable beam-beam tune shift. The limit will be taken where there appears to be a distinct threshold on the preservation of beam quality, and not linked to a hard limit on either output. Pessimistically, the chromaticity will be set to $Q' = 15$ in these simulations, assumed necessary to prevent coherent instabilities. The beta function will be set to $\beta_q^* = 12\,\mathrm{cm}$, as have been found optimal to reduce the problems caused by this level of chromaticity at the LHC working point. This β_q^* is similar to the design value for the HL-LHC.

The first configuration that will be considered has round beams colliding head-on with zero crossing angle. The intermediate phase advance is set to $\mu_1 = \mu/2$, as was found optimal in Sec. 4.5. This is similar to the configuration considered in [10]. The results are presented as functions of $\Delta Q_{\mathrm{Tot}}(\phi_{\mathrm{PIW}})$ in Fig. 4.36. In this configuration, the maximum acceptable beam-beam tune shift from the LHC working point is approximately $\Delta Q_{\mathrm{Tot}} = 0.26$. Above this limit the *NADA* decreases and the LR_{Beam} increases fast. The preservation of beam quality is not unaltered with this beam-beam tune shift, but it is tolerable. The limit is slightly larger for the first alternative working point $(0.315, 0.325)$ and even larger for the third alternative working point. This configuration is however quite unrealistic. First of all, it is not possible to keep exactly the smart intermediate phase advance $\mu_1 = \mu/2$. The acceptable phase error has been found to decrease for increasing ξ_{Tot}, and was approaching zero for a beam-beam parameter of $\xi_{\mathrm{Tot}} = 0.05$, much smaller than the limits found for this configuration. Second of all, with as large tune shifts as considered as limits here, the tune footprint is approximately cut down the middle by the coupling resonance. It has been stated that the effects modelled in CABIN generally cause less beam deterioration for working points close to the diagonal. However, other instabilities are assumed to cause more problems when incoherent particles have equal horizontal and vertical tunes. Finally, this configuration is not affected by odd resonances. It is unlikely, although not impossible, that this will be achievable in circular colliders.

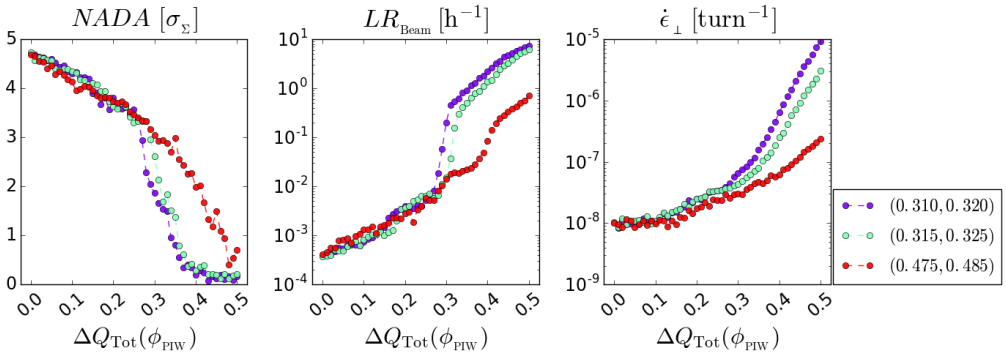

Figure 4.36: Beam quality reduction for increasing beam-beam parameter, ξ_{Tot}, until a threshold is found. Simulations are run for zero crossing angle, large chromaticity, $Q' = 15$, significant hour-glass effect, $\beta_q^* = 12\,\mathrm{cm}$, and smart intermediate phase advance, $\mu_1 = \mu/2$, at the three working points given by the legend. The outputs *NADA*, LR_{Beam} and $\dot{\epsilon}_\perp$ have been calculated as expressed in Sec. 3.4. The outputs are presented as functions of the total beam-beam tune shift, $\Delta Q_{\mathrm{Tot}}(\phi_{\mathrm{PIW}})$.

The idea of using specific intermediate phase advances has been found interesting, but not necessarily realistic. The required accuracy is perhaps impossible to achieve for large beam-beam parameters, $\xi_{\mathrm{Tot}} > 0.05$. The scan for zero crossing angle has thus been repeated with zero intermediate phase advance, and the results are presented as functions of $\Delta Q_{\mathrm{Tot}}(\phi_{\mathrm{PIW}})$ in Fig. 4.37. Without the improvement from the intermediate phase advance, the maximum acceptable beam-beam tune shift from the LHC working point is reduced significantly to approximately $\Delta Q_{\mathrm{Tot}} = 0.043$. Above this limit the loss rate increases rapidly. The limit for the first alternative working point, $(0.315, 0.325)$, is approximately 0.067. The limit is similar for the second alternative working point, $(0.475, 0.485)$, although the limit for this working point is less abrupt. The loss rate increases, but the emittance growth rate is small until $\Delta Q_{\mathrm{Tot}} = 0.25$. This suggests that the particles in the core may be kept even if the tails are lost, for large beam-beam parameters, when operating at $(0.475, 0.485)$.

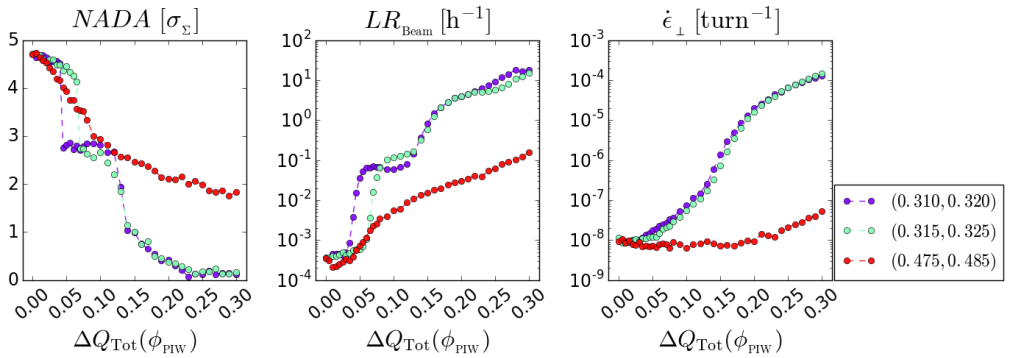

Figure 4.37: Beam quality reduction for increasing beam-beam parameter, ξ_{Tot}, until a threshold is found. Simulations are run for zero crossing angle, large chromaticity, $Q' = 15$, significant hourglass effect, $\beta_q^* = 12\,\mathrm{cm}$, and zero intermediate phase advance, $\mu_1 = 0$, at the three working points given by the legend. The outputs $NADA$, LR_{Beam} and $\dot{\epsilon}_\perp$ have been calculated as expressed in Sec. 3.4. The outputs are presented as functions of the total beam-beam tune shift, $\Delta Q_{\mathrm{Tot}}(\phi_{\mathrm{PIW}})$.

In future colliders, the strength of LR interactions might be weaker and the Piwinski angle might be cancelled by use of crab cavities. Nevertheless, it is unrealistic to assume that odd resonances will be completely suppressed. Therefore, the beam-beam parameter scan has been repeated for a configuration with a significant Piwinski angle, $\phi_{\mathrm{PIW}} = 1$, and zero intermediate phase advance. The results of this scan are presented in Fig. 4.38. The limit at the LHC working point is approximately $\Delta Q_{\mathrm{Tot}} = 0.028$. For the first alternative working point, $(0.315, 0.325)$, there is a slightly decrease in preservation of beam quality for small beam-beam tune shifts, as discussed in Sec. 4.2. The general behaviour is acceptable until $\Delta Q_{\mathrm{Tot}} = 0.036$. For the second alternative working point, the limit is approximately $\Delta Q_{\mathrm{Tot}} = 0.06$.

In this section, we have tried to establish a fundamental limit for the beam-beam tune shift, for realistic scenarios. With use of the clever phase advance $\mu/2$ and no effects driving the odd resonances, there is no fundamental limit on the beam-beam tune shift before $\Delta Q_{\mathrm{Tot}} = 0.26$. This limit is reduced significantly at the LHC working point for zero intermediate phase advance, down to $\Delta Q_{\mathrm{Tot}} = 0.043$, and even further for a nonzero crossing angle, down to $\Delta Q_{\mathrm{Tot}} = 0.028$. The alternative working point, $(0.315, 0.325)$, has been found in Sec. 4.7 to be associated with small loss rates for large beam-beam tune shifts in the LHC. The maximum acceptable beam-beam tune shift from this working point is $\Delta Q_{\mathrm{Tot}} = 0.067$ with zero crossing angle, and $\Delta Q_{\mathrm{Tot}} = 0.036$ with nonzero crossing angle. The last two studies were rerun with $\beta_q^* = 30\,\mathrm{cm}$, the design value for the

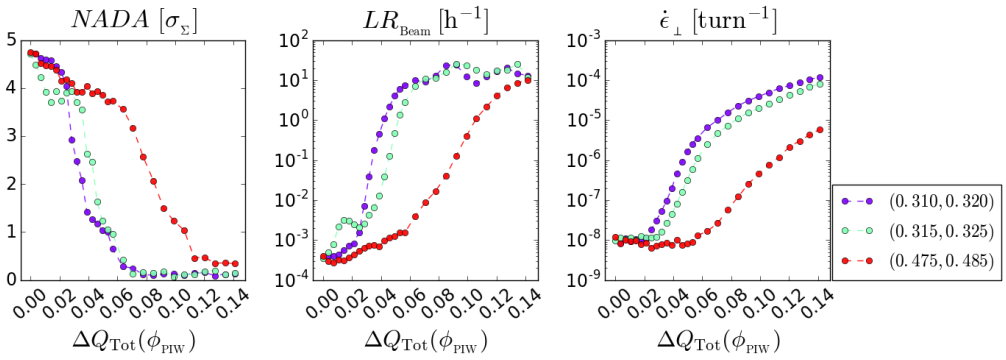

Figure 4.38: Beam quality reduction for increasing beam-beam parameter, ξ_{Tot}, until a threshold is found. Simulations are run with a significant crossing angle, $\phi_{\mathrm{PIW}} = 1$, large chromaticity, $Q' = 15$, significant hourglass effect, $\beta_q^* = 12\,\mathrm{cm}$, and zero intermediate phase advance, $\mu_1 = 0$, at the three working points given by the legend. The outputs $NADA$, LR_{Beam} and $\dot{\epsilon}_\perp$ have been calculated as expressed in Sec. 3.4. The outputs are presented as functions of the total beam-beam tune shift, $\Delta Q_{\mathrm{Tot}}(\phi_{\mathrm{PIW}})$.

FCC-hh. This choice reduced the limit on the tune shift further. All realistic limits for the LHC working point, $(0.31, 0.32)$, and the first alternative working point, $(0.315, 0.325)$, are presented in Tab. 4.1.

Table 4.1: Maximum acceptable beam-beam tune shift, for pessimistic, realistic configurations.

(Q_x, Q_y)	β_q^* [cm]	$\Delta Q_{\mathrm{Tot}}(\phi_{\mathrm{PIW}} = 0)$	$\Delta Q_{\mathrm{Tot}}(\phi_{\mathrm{PIW}} = 1)$
$(0.31, 0.32)$	12	0.043	0.028
$(0.31, 0.32)$	30	0.035	0.018
$(0.315, 0.325)$	12	0.067	0.036
$(0.315, 0.325)$	30	0.060	0.026

The beam-beam tune shift limit at the alternative working point close to the half-integer resonance, $(0.475, 0.485)$, has not been considered realistic in this study. More studies are needed to quantify whether effects not considered in this thesis cause instabilities, optics correction issues or strong diffusivity for this working point, rendering this working point impractical for colliders. The tune shifts in this section have been calculated using Eq. (2.85), which assumes that resonances do not affect the particles. This assumption is not valid for the tune shifts considered here. However, the estimates are approximately correct, especially for smaller beam-beam tune shifts.

Chapter 5

CONCLUSION

The beam-beam interaction widens the tune spectrum of the beam, and drives detrimental resonances. The width of the tune spectrum is proportional to the strength of the beam-beam interaction. In result, strong beam-beam interactions limit the performance of a collider. The object of this thesis has been to study the parametric dependence of detrimental mechanisms related to beam-beam interactions. This has been done extensively by use of new beam quality simulations and FMAs.

In order to accurately quantify the impact on the beam quality, a high-performance tracking code named CABIN has been developed. It is designed to study the beam-beam interaction, which has been implemented by the weak-strong approach for both round and flat beams in both 4D and 6D. The modelling of the beam-beam interaction consumes in general more than 95% of the computation time of the simulations. The implementation using a GPU has reduced the tracking time by approximately 3 orders of magnitude, compared to a single CPU. A new regionally uniform initial distribution has been designed to model the evolution of both the core and the tail of the bunch accurately, while maintaining realistic computing requirements. It represents a 6D Gaussian bunch up to 6σ with the required accuracy, using only $N_{\text{mp}} = 1 \times 10^5$ macroparticles. Especially the relative error of the loss rate measurement has been reduced from 86% to 8%, compared to a Gaussian distribution of the same number of macroparticles. Simulation results produced with this code showed good quantitative agreement with a dedicated experiment done at the LHC, and allowed to identify the role of the crossing angle in the observed loss mechanism.

The impact of the resonances is found to be more severe for particles at larger transverse amplitudes, affected by resonances of lower order, and driven by stronger beam-beam interactions. While perfect head-on interactions only drive betatron resonances of even order, effects that make the beam-beam interaction asymmetric, as a transverse separation or a nonzero crossing angle, drive odd resonances as well. Mixing between the transverse and the longitudinal dimensions, caused by either chromaticity, a nonzero crossing angle or the hourglass effect, activates and drives additional synchro-betatron resonances. More resonances and more degrees of freedom of the motion, have been found to generally cause stronger deterioration of the beam, as expected for a nonlinear dynamical system.

Some effects have been shown to improve the beam quality for a given total beam-beam parameter. The best beam performance has been found for zero crossing angle, as the odd resonances are not activated. The crossing angle is generally nonzero in modern circular colliders, but may be forced zero for the head-on interactions by crab cavities in the HL-LHC and FCC-hh. Thus, the odd synchro-betatron resonances due to the head-on interactions could be suppressed. Increasing the crossing angle further past $\phi_{\text{PIW}} = 1$ also reduces the detrimental effects. This improvement

has been found to be caused by the decrease of the beam-beam tune shift and spread. As a result, the particles in the beam are affected by fewer strong resonances. Nevertheless, this regime is not preferable for operation, since the luminosity is also decreasing for larger crossing angles.

A transverse separation of more than 2σ also improves the beam quality by reducing the beam-beam tune shift. This is done to intentionally reduce the luminosity in a single experiment. However, for a nonzero separation of less than 2σ, the altered nonlinearities can deteriorate the beam quality faster than with zero separation. Using such separations to reduce the luminosity is therefore not an optimal strategy to minimise the impact of the beam-beam interaction on the beam quality.

A few specific configurations were also found to improve the beam quality without reducing the luminosity. A nonzero chromaticity is necessary to avoid coherent instabilities, even if it causes worse long-term beam quality. It has been found that a significant hourglass effect reduces the detrimental effects caused by chromaticity, and vice versa. With a large chromaticity, $Q' = 15$ at the LHC working point, $(0.31, 0.32)$, the optimal strength of the hourglass effect is when $\sigma_s/\beta_q^* \approx 2/3$, corresponding to $\beta_q^* = 12\,\mathrm{cm}$ in the FCC-hh, which is smaller than the current design value.

Enforcing intermediate phase advances of $\mu_1 = \mu/2$ or $\pi/2$, were expected from first order theory to reduce the effect of resonances. The symmetric phase advance, $\mu/2$, improved the performance for all working points. An optimal intermediate phase advance was also found close to $\pi/2$, but it was different from the expected value and found to depend on the working point. Both phase advances improved the beam quality best for zero crossing angle. The effect was marginal for a significant crossing angle, $\phi_{\text{PIW}} = 1$. It was found that the accuracy required to keep the resonance coefficients suppressed was high. However, the effect on the beam quality remained under control with a reduced accuracy that is within reach using modern optics correction methods.

The LHC working point, $(0.31, 0.32)$, has been found to work well for small beam-beam parameters. With a Piwinski angle of $\phi_{\text{PIW}} = 1$, a significant chromaticity, $Q' = 15$, and a beam-beam tune shift equal to the maximum tune shift in the FCC-hh, $\Delta Q_{\text{Tot}} = 0.03$, two alternative working points were found to better preserve the beam quality, $(0.315, 0.325)$ and $(0.475, 0.485)$. The beam quality was generally also found to be better closer to the coupling resonance. A realistic, pessimistic maximum beam-beam tune shift from the LHC working point, is found to be $\Delta Q_{\text{Tot}} = 0.043$ with zero crossing angle. With a Piwinski angle of $\phi_{\text{PIW}} = 1$, this limit is reduced to $\Delta Q_{\text{Tot}} = 0.028$. The limits are larger for the alternative working point, $(0.315, 0.325)$, being $\Delta Q_{\text{Tot}} = 0.067$ and 0.036 respectively. These values correspond to the optimum hourglass effect with $\beta_q^* = 12\,\mathrm{cm}$. For the FCC-hh design parameters, $\beta_q^* = 30\,\mathrm{cm}$ at the LHC working point, the limits for zero and nonzero crossing angle are reduced to $\Delta Q_{\text{Tot}} = 0.035$ and 0.018 respectively. The limit for nonzero crossing angle is significantly smaller than the largest beam-beam tune shift expected in the FCC-hh, which should be taken into consideration in the further development of the collider. In particular, other sources of odd resonances, such as the imperfections of the magnetic lattice or long-range beam-beam interactions, should be further investigated to see if they also reduce the maximum acceptable beam-beam tune shift.

There are several possible extensions of the study presented in this thesis. First of all, the unavoidable long-range interactions should be included. These are expected to drive odd resonances in a similar manner to a separation of the head-on interaction, even if the Piwinski angle of the head-on interactions is reduced to zero by crab-cavities. Second of all, a simplified model of the lattice nonlinearities could be included. These have been expected to continue the diffusion from $5\sigma_\Sigma$, but this has not been checked. Finally, the alternative working points close to the half-integer resonances, represented by $(0.475, 0.485)$, are found to be optimal based on the effects modelled in CABIN. Effects that are not discussed here are known to cause issues for working points in this area of tune space, in particular coherent effects and the correction of the optics. This study supports further investigations of these effects, in order to assess the possibility of using this working point for operation of a circular hadron collider.

BIBLIOGRAPHY

[1] S. V. Furuseth. "GPU-Powered Modelling of Nonlinear Effects due to Head-On Beam-Beam Interactions in High-Energy Hadron Colliders". Specialization project report. Available upon request. https://drive.google.com/file/d/0B20z4gUQ0oa7VUhkXzYzQXVhS2c/view?usp=sharing, 2017. Accessed: 2017-08-12.

[2] CERN. "The CERN accelerator complex". https://cds.cern.ch/record/2197559/files/CCC-v2016.png, 2016. Accessed: 2017-07-15.

[3] O. S. Brüning, P. Collier, P. Lebrun, S. Myers, R. Ostojic, J. Poole, and P. Proudlock. "LHC Design Report". 2004.

[4] W. Herr and T. Pieloni. "Beam-Beam Effects". Proc. CERN Accelerator School, Trondheim, 2013, CERN-2014-009. pages 431–459, 2014.

[5] D. Schulte. "Preliminary Collider Baseline Parameters: Deliverable D1.1". Study: CERN FCC. 2015.

[6] W. Herr and D. Kaltchev. "Effect of phase advance between interaction points in the LHC on the beam-beam interaction". LHC Project Report 1082. 2008.

[7] K. Ohmi, K. Hirata, and N. Toge. "Quasi-strong-strong simulations for beam-beam interactions in KEKB". 5th European Particle Accelerator Conference, Sitges, Barcelona, Spain. pages 1164–1166, 1996.

[8] J. Qiang, M. Furman, R. D. Ryne, W. Fischer, T. Sen, and M. Xiao. "Parallel Strong-Strong/Strong-Weak Simulations of Beam-Beam Interaction in Hadron Accelerators". 693:278–281, December 2003.

[9] Y. Papahilippou and F. Zimmermann. "Weak-strong beam-beam simulations for the Large Hadron Collider". Phys. Rev. ST Accel. Beams 2, 104001. 1999.

[10] K. Ohmi and F. Zimmermann. "Fundamental beam-beam limit from head-on interaction in the Large Hadron Collider". 10.1103/PhysRevSTAB.18.121003. 2015.

[11] A. Wolski. *"Beam Dynamics in High Energy Particle Accelerators"*. Imperial College Press, 2014.

[12] B. Holzer. "Transverse Dynamics". Lect. CERN Accelerator School, Baden. 2004.

[13] V. Kain. “Accelerators”. Summer Student Lecture, CERN. 2017.

[14] A. J. Lichtenberg and M. A. Lieberman. *“Regular and Chaotic Dynamics”*. Springer, 2nd edition, 1992.

[15] Goldstein, Safko, and Poole. *“Classical Mechanics”*. Pearson Education, 3rd edition, 2014.

[16] F. Tecker. “Longitudinal beam dynamics”. Proc. CERN Accelerator School, Trondheim, 2013. 10.5170/CERN-2014-009.1. 2014.

[17] D. Cocq et al. “The Measurement of Chromaticity via a Head-Tail Phase Shift”. CERN SL-98-062 BI. 1998.

[18] A. Verdier. “Chromaticity”. CERN Accelerator School, Greece, 1995. 10.5170/CERN-1995-006.77. 1998.

[19] G. Rumolo. “Beam Instabilities”. Proc. CERN Accelerator School, Trondheim, 2013. 10.5170/CERN-2014-009.199. 2013.

[20] R. Calaga. “Crab Cavities For The LHC Upgrade”. Proc. Chamonix workshop on LHC Performance. 10.5170/CERN-2012-006.363. 2012.

[21] W. Herr et al. “Concept of Luminosity in particle colliders”. CERN Accelerator School, Bulgaria. 2010.

[22] D. Brandt, H. Burkhardt, M. Lamont, S. Myers, and J. Wenninger. “Accelerator Physics at LEP”. CERN-SL-2000-037 DI. 2000.

[23] D. J. Griffiths. *“Introduction to Electrodynamics”*. Pearson Education, 3rd edition, 2008.

[24] M. Bassetti and G. A. Erskine. “Closed expression for the electrical field of a two-dimensional Gaussian charge”. CERN-ISR-TH/80-06. 1980.

[25] W. Herr. “Beam-beam effects”. Pres. CERN Accelerator School, Darmstadt. 2009.

[26] E. Wilson. “Non-linearities and resonances”. 10.5170/CERN-1985-019-V-1.96. 1986.

[27] A. Chao. *“Lecture Notes on Special Topics in Accelerator Physics”*. 2012.

[28] X. Buffat. “Working Point in collision”. Pres. FCC-hh General Design Meeting, 27 May 2015.

[29] CERN. “LHC Optics Web: LHC Run II pp physics optics”, 2017.

[30] K. Hirata. “Don’t Be Afraid of Beam-Beam Interactions With a Large Crossing Angle”. SLAC-PUB-6375. 1994.

[31] K. Hirata, H. Moshammer, and F. Ruggiero. “A Symplectic Beam-Beam Interaction with Energy Change”. SLAC-PUB-10055, KEK Preprint 92-117. 1992.

[32] J. B. García and T. Pieloni. “Status of new input definition of the beam-beam lens in SixTrack”. Pres. 59th HiLumi WP2 Task Leader Meeting, 13 Nov 2015.

[33] CERN. LHC Collimation Working Group. Webpage. `http://lhc-collimation.web.cern.ch/lhc-collimation/`, 2017. Accessed: 2017-07-20.

[34] M. Martini. “Intrabeam scattering”. Pres. CERN Accelerator School, Switzerland. 2015.

[35] A. Wolski. “Low Emittance Rings”. Proc. CERN Accelerator School, Chios, 10.5170/CERN-2014-009.245. 2014.

[36] X. Buffat et al. “Evolution of the beam parameters during luminosity production in the Future Circular Hadron Collider”. Proc. IPAC2016. TUPMW008. 2016.

[37] S. V. Furuseth. “CABIN (Cuda-Accelerated Beam-beam Interaction)” . https://gitlab.cern.ch/sfuruset/CABIN, 2017. Accessed: 2017-08-13.

[38] G. Apollinari et al. “High-Luminosity Large Hadron Collider (HL-LHC) Preliminary Design Report”. CERN-2015-005. 2015.

[39] A. Oeftiger et al. “Review of CPU and GPU Faddeeva Implementations”. Proc. of IPAC2016. WEPOY044. 2016.

[40] Y. Luo and W. Fischer. “Computational challenges for beam-beam simulation for RHIC”. Proceedings of HB2010. WEO2C02. 2010.

[41] W. Scandale. “Dynamic aperture”. CERN Accelerator School, Rhodes. CERN-SL-94-24. 1994.

[42] J. Laskar. “Frequency Map Analysis and Particle Accelerators”. Proc. 2003 Particle Accelerator Conference. 2003.

[43] CERN. “PySussix”. https://github.com/PyCOMPLETE/PySUSSIX, Apr 2016. Accessed: 2016-08-16.

[44] R. Bartolini and F. Schmidt. “SUSSIX: A Computer Code for Frequency Analysis of Non–Linear Betatron Motion”. CERN SL/Note 98-017 (AP). 1998.

[45] J. Vazquez. “HARPY”. https://github.com/pylhc/harpy, July 2017. Accessed: 2016-09-27.

[46] R. Tomás et al. “Record low β beating in the LHC”. Phys. Rev. ST Accel. Beams 15, 091001. 2012.

[47] S. M. White et al. “Optimization of the LHC separation bumps including beam-beam effects”. Proceedings of PAC09. WE6PFP018. 2009.

[48] X. Buffat, S. V. Furuseth, et al. “Limitations due to strong head-on beam-beam interactions”. MD 1434. CERN-ACC-NOTE-2017-0044. 2017.

[49] J. B. García, T. Pieloni, X. Buffat, and S. V. Furuseth. “Beam-beam studies for FCC-hh”. IPAC2017, Copenhagen. TUPVA026. 2017.

[50] A. Einstein. “Investigations on the theory of the Brownian movement”. 1956, (Orig. 1926).

[51] G. W. Amdahl. “Validity of the single-processor approach to achieve large scale computing capabilities”. AFIPS Joint Spring Conference Proceedings. 10.1145/1465482.1465560. pages 483–485, 1967.

[52] NVIDIA. “Tesla C2075”. https://www.nvidia.com/docs/IO/43395/NV-DS-Tesla-C2075.pdf, 2011. Accessed: 2017-07-12.

[53] NVIDIA. “Tesla P100 PCIe”. http://images.nvidia.com/content/tesla/pdf/nvidia-tesla-p100-PCIe-datasheet.pdf, 2016. Accessed: 2017-07-12.

Appendix A

DIFFUSION

Consider a 1D diffusion of the normalised momentum density $n(p_x, t)$ with constant diffusivity D. Fick's law reads in this case

$$\frac{\mathrm{d}n}{\mathrm{d}t} = D\frac{\mathrm{d}^2 n}{\mathrm{d}p_x^2} \,. \tag{A.1}$$

Through insertion one can see that this is solved for a Gaussian initial condition (IC) by

$$n(p_x, t) = \frac{N}{\sqrt{4\pi D(k+t)}} \exp\left[-\frac{p_x^2}{4D(k+t)}\right] , \tag{A.2}$$

where k is a constant defined by the IC. Integrating this distribution over all momentum gives the total number of particles N. Through comparison with a 1D Gaussian, or from performing the calculation, one get that the second moment $\langle p_x^2 \rangle$ increases linearly with time

$$\langle p_x^2 \rangle = 2D(k+t) = \sigma_{p_x}^2 \,, \tag{A.3}$$

where $2Dk = \sigma_{p_x,0}^2$ is the variation at time $t = 0$.

Diffusion can be achieved with a normally distributed kick κ with rms amplitude Δ, on the momentum p_x of each particle in $n(p_x, t)$. The relation between Δ and the diffusivity, D in (A.1), can be expressed as [50]

$$D = \int_{-\infty}^{\infty} \mathrm{d}\kappa \, \frac{\kappa^2}{2\delta t} \frac{1}{\sqrt{2\pi}\Delta} \exp\left[-\frac{\kappa^2}{2\Delta^2}\right] = \frac{\Delta^2}{2\delta t} \,, \tag{A.4}$$

where δt is the time interval between each kick. The amplitude of noise Δ can thus be set to produce a given expected growth rate caused by noise alone.

Consider an example relevant for simulations done in CABIN [37]. Set the rms amplitude of the kick to be $\Delta = \sigma_{p_x,0} \times 10^{-4}$, and assume that the momentum of each particle is kicked once per turn, $\delta t = 1/f_{\mathrm{rev}}$, where f_{rev} is the revolution frequency. The evolution of the second moment of p_x is then

$$\sigma_{p_x}^2 = \sigma_{p_x,0}^2 \cdot (1 + T \times 10^{-8}) \,, \tag{A.5}$$

where T is the turn number, equal to $t \cdot f_{\mathrm{rev}}$. For the normalised Gaussian distribution considered in this thesis, $\sigma_{p_x,0} = 1$. The growth rate of the second moment of p_x is equivalent to the emittance growth rate expected from noise alone, $\dot{\epsilon}_0 = 1 \times 10^{-8}$ /turn. ϵ_0 is the emittance based on normalised coordinates, equal to 2 for a perfect Gaussian distribution.

Appendix B

TESTING CABIN

B.1 Benchmarking

The 6D beam-beam map in CABIN [37] is based on the work done and code written by K. Hirata [30, 31]. Hence the two codes should give the same results. Two major difference is in the calculation of the inverse cumulative Gaussian distribution, necessary for the barycentres of the individual slices, and in the calculation of the complex Faddeeva function, necessary for the kick of each slice. Hirata's code applies a lookup table for the inverse cumulative Gaussian while CABIN applies a built-in function of SciPy (norm.ppf). The difference between the two implementations for values on the interval $[0.005, 0.995]$ oscillates around zero with a rms-error of $\text{err}_{\text{gauinv}} = 4.2 \times 10^{-5}$. Outside of this interval the error increases to $\lim_{x \to \{0,1\}} \text{err}_{\text{gauinv}} = 0.001$. Hirata's code applies a lookup table also for the complex Faddeeva function, while CABIN applies a GPU-implementation [39]. The error of this CUDA-implementation is for most inputs less than $\text{err}_{\text{erf,C}} \lesssim 1 \times 10^{-9}$. The relative error of the lookup-table version of the complex Faddeeva function is shown in Fig. B.1, where the error refers to the discrepancy between the two implementations. The error is for both the real and imaginary outputs in the order of $\text{err}_{\text{erf,H}} \lesssim 1 \times 10^{-7}$ when either input is above ~ 2. The errors are in general a few orders of magnitude greater when both inputs are below ~ 2, especially for the imaginary output. The lookup-function produces for such inputs incorrectly negative imaginary values. The inputs depend on the ratio between the transverse position and the difference between the horizontal and vertical beam sizes, and will thus only be small for particles deep in the core for flat beams where the kick is approximately zero. The following tests will not be affected by this error in the lookup function. Since both of these functions give different results, the difference between the two implementations cannot be expected to be smaller than approximately 10^{-5}.

Hirata's code was initially designed for lepton machines, and contains only the map for flat beams. CABIN is designed for hadron colliders and has thus both an implementation for round beams and for flat beams, the round being faster and thus preferred when valid. The beam-beam map is calculated for 20^3 particles distributed in a 3D grid in $(\hat{x}, \hat{y}, \hat{s})$, where each coordinate is uniformly distributed as $\hat{x}_i = \{0.1, 0.6, ..., 9.6\}$ in normalised coordinates. The error between the two codes is calculated as the rms difference, relative to the maximum kick of Hirata's code, for each of the coordinates separately, not including the longitudinal coordinate s since this is not changed by the beam-beam interaction. The 6D nature of the interaction is most prominent in cases where either σ_s/β_q^* or ϕ_{PIW} or both are significantly nonzero, hence such configurations will be used to benchmark CABIN versus Hirata's code. The tests that follow share the same normalised emittance

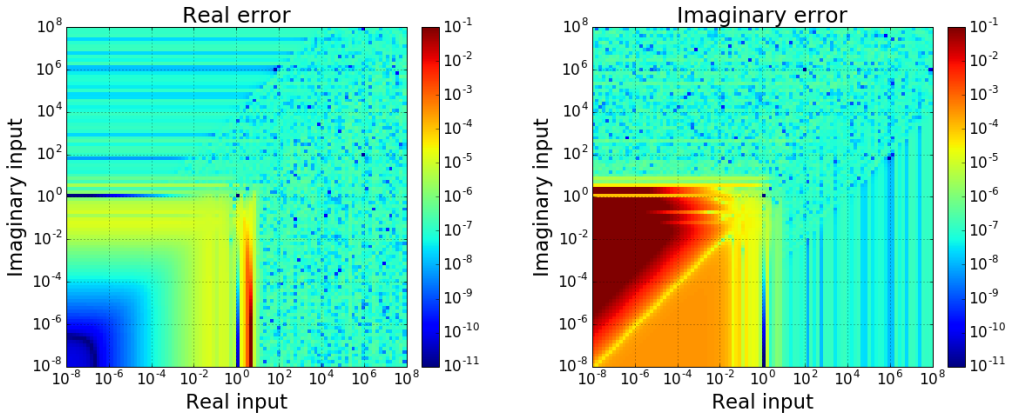

(a) (b)

Figure B.1: Relative error between the implementation of the complex Faddeeva function in Hirata's code and CABIN. (**a**) shows the error in the real output. (**b**) shows the error in the imaginary output.

in both planes and both beams, $\epsilon_{n,x1} = \epsilon_{n,y1} = \epsilon_{n,x2} = \epsilon_{n,y2} = 3\,\mu\mathrm{m}$, and the same longitudinal beam size, $\sigma_s = 8\,\mathrm{cm}$.

The errors for the different coordinates between the round beam implementation in CABIN and Hirata's code is visualised in Fig. B.2a for $\beta_q^* = 1\,\mathrm{cm}$ and horizontal Piwinski angle $\phi_{\mathrm{PIW},x} = 2$. A less extreme configuration is presented in Fig. B.2b, with $\beta_q^* = 40\,\mathrm{cm}$ and horizontal $\phi_{\mathrm{PIW},x} = 1$. The flat beam implementation does not work when considering round beams, and the beam-beam map from Hirata's code has been calculated after slightly increasing β_y^*. All errors presented has been calculated with a moderate number of slices, $N_\mathrm{S} = 31$. The errors do not decrease if more slices are used. The errors in these configurations converge for all coordinates as $\beta_y^* \to \beta_x^*$. The most erroneous coordinate is δ. That might be because this is the coordinate that changes the least, and thus is most vulnerable to numerical error. From comparison also with additional configurations, the errors slightly increase in general as β_q^* decreases or ϕ_{PIW} increases. The errors presented converge to values that all are below or of the same order as the errors in the two lookup-table functions applied in Hirata's code. Hence the round beam implementation in CABIN is in good agreement with the limiting case of Hirata's code. For configurations with even smaller β_q^* the error would continue to increase, but such configurations will require a very high number of slices two be calculated physically accurate and are not feasible for accelerators today as the LHC.

The results for the flat beam implementation are presented in Fig. B.3, where the ratio between the two transverse axes has been controlled by setting $\beta_x^* \neq \beta_y^*$ while keeping the emittances equal. There is no longer need to look for the convergence as $\beta_y^* \to \beta_x^*$ as they are supposed to be different. These calculations have been done with $N_\mathrm{S} = 61$. The dependence of the error as the beams become flatter is shown in Fig. B.3a, for $\beta_y^* = 1\,\mathrm{cm}$ and $\phi_{\mathrm{PIW},x} = 0$. The error increases in these configurations as the beams become rounder. This might be linked to problems with such small values for β_q^*, as discussed above. The dependence of the error is equivalently shown in Fig. B.3b, for $\beta_y^* = 10\,\mathrm{cm}$ and $\phi_{\mathrm{PIW},x} = 2$. With a large crossing angle and a slightly bigger β_y^*, the error now increases as the beams become flatter, possibly linked to the increased error for smaller inputs in the complex Faddeeva function. As for the implementation of the round beam-beam interaction, the

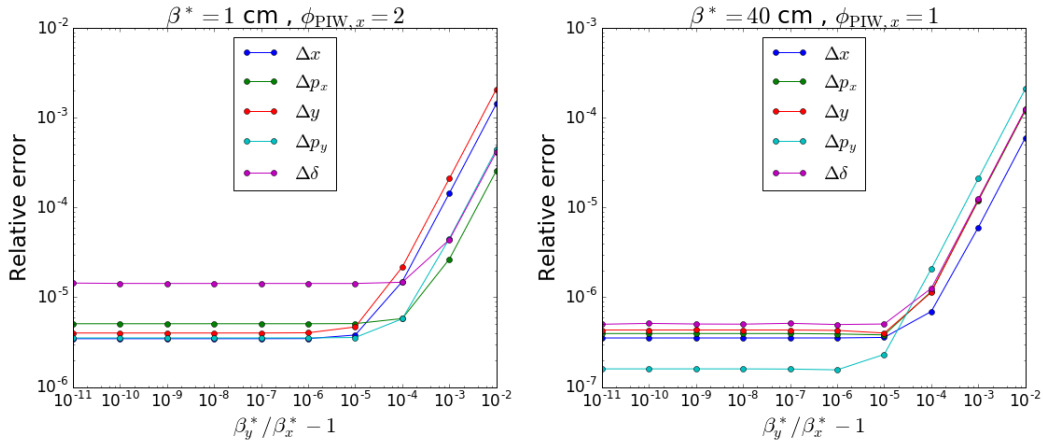

(a) **(b)**

Figure B.2: Relative error between the flat beam-beam map in Hirata's code, as $\beta_y^* \to \beta_x^*$, and the round beam-beam map in CABIN, for each coordinate separately. (**a**) is for $\beta_q^* = 1\,\mathrm{cm}$ and $\phi_{\mathrm{PIW},x} = 2$. (**b**) is for $\beta_q^* = 40\,\mathrm{cm}$ and $\phi_{\mathrm{PIW},x} = 1$.

errors seems to be below or of the same order as the errors in the two lookup-table functions applied in Hirata's code. Therefore, the flat beam implementation is in good agreement with Hirata's code, at least for the configurations of interest.

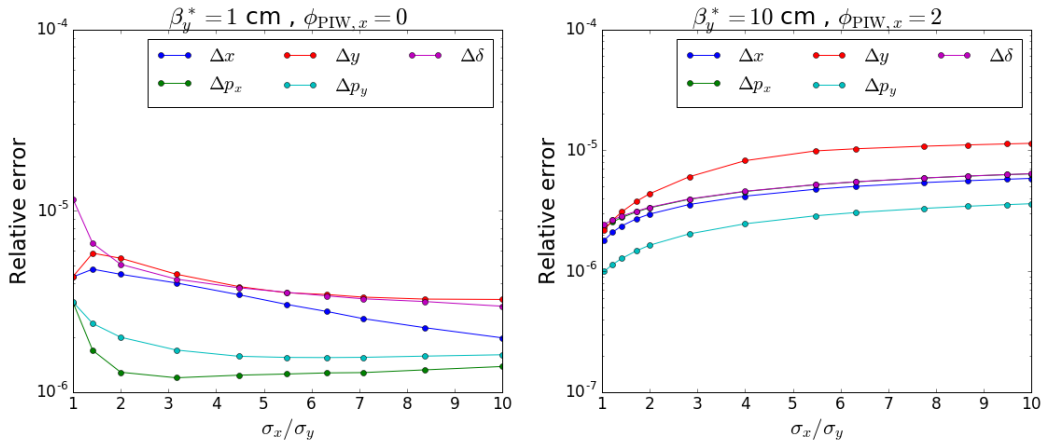

(a) **(b)**

Figure B.3: Relative error between the flat beam-beam map in Hirata's code and CABIN, for different ratios between the two transverse sizes. (**a**) is for $\beta_y^* = 1\,\mathrm{cm}$ and $\phi_{\mathrm{PIW},x} = 0$. (**b**) is for $\beta_y^* = 10\,\mathrm{cm}$ and and $\phi_{\mathrm{PIW},x} = 2$.

B.2 Slice Convergence

The reduction of the continuous 6D beam-beam kick into a series of discrete interactions with longitudinal slices of the other beam, is a generalisation from the 4D model. The 4D model is in comparison the kick of a single slice on only the transverse coordinates, independent of the longitudinal distribution. As the number of slices tends to infinity, $N_\mathrm{S} \to \infty$, this method is equivalent to integration. Due to the smoothness of the Gaussian distribution, a relatively low number of slices is necessary to represent the 6D nature of the beam-beam interaction accurately. Hirata concluded that, for his work, as few as $N_\mathrm{S} = 5$ was sufficient, which he based on the convergence of the transverse beam size [31]. The number of slices necessary should however depend on the crossing angle, ϕ_{PIW}, and the hourglass effect, expressed by the ratio σ_s/β_q^*. In the limit of zero crossing angle and no hourglass effect the 4D model, or $N_\mathrm{S} = 1$, is sufficient, but as these constraints are gradually lifted, the required number of slices should increase. This section studies the convergence with N_S for different configurations, based directly on the beam-beam map.

For each value of N_S, the beam-beam map has been calculated for $N_\text{mp} = 3000$ particles distributed in 3 groups of equal size. Group 1 is a 3D grid in $(\hat{x}, \hat{y}, \hat{s})$, where each coordinate is uniformly distributed as $\hat{x}_i = \{0.1, 1.1, ..., 9.1\}$, group 2 is distributed uniformly only along the $\hat{x}$ axis on the interval $\hat{x} \in (0, 10]$, and group 3 is distributed equivalently along the $\hat{s}$ axis. If there is a nonzero crossing angle, the crossing is in the horizontal plane. The error has been calculated for each coordinate separately, as the rms error relative to the beam-beam map acquired with a large number of slices, $N_\mathrm{S} = 200$. The change is negligible if the assumed correct value is calculated with a larger number of slices as $N_\mathrm{S} = 1000$. Because there is mixing between the positional and translational coordinate in each plane, and also mixing between the planes, the error in one coordinate is not confined, but can transfer to other coordinates as well. The error presented for a certain N_S, $\mathrm{err}_{N_\mathrm{S}}$, is therefore the largest of these errors. The average error is in many cases much smaller than what is presented. The tests that follows share the same normalised emittance in both planes and both beams, $\epsilon_{n,x1} = \epsilon_{n,y1} = \epsilon_{n,x2} = \epsilon_{n,y2} = 3\,\mu\mathrm{m}$, and the same longitudinal beam size, $\sigma_s = 8\,\mathrm{cm}$.

The dependence of error on N_S has been investigated for different values of β_q^* in the round beam scheme with zero crossing angle, and the results are presented in Fig. B.4a. For the largest value of β_q^*, $\sigma_s/\beta_q^* = 0.1$, the error is $\mathrm{err}_{N_\mathrm{S}} = 0.002$ for $N_\mathrm{S} = 1$, implying that the hourglass effect may be considered negligible, depending on the chosen tolerance. As β_q^* is reduced further, the hourglass effect is more important, and the error is larger for the same N_S. For $\beta_q^* = 1\,\mathrm{cm}$ the error is approximately 1% for $N_\mathrm{S} = 50$, and the reduction rate is slow. That is, more slices are needed as expected when σ_s/β_q^* increases. The largest error measured for these configurations is in the change of the energy, $\Delta\delta$, approximately an order of magnitude larger than the second largest error. Fig. B.4b shows how $\Delta\delta$ depends on N_S for particles distributed along the s axis for $\beta_q^* = 2.5\,\mathrm{cm}$, between the limiting cases of $N_\mathrm{S} = 1$ and $N_\mathrm{S} = 200$. The additional values of N_S has been chosen so that $\mathrm{err}_{N_\mathrm{S}} \leq \mathrm{tol}_j$ for different tolerances, tol_j. Remember that $N_\mathrm{S} = 1$ does not correspond directly to the 4D model, unless the requirements for the 4D model to be valid are met. This plot illustrates that already for a tolerance of $\mathrm{tol} = 1\%$, the general behaviour of the function is much better described than with a single slice, and can be considered valid to represent the physics as σ_s/β_q^* reaches correspondingly large values.

The dependence of error on N_S has been investigated for different values of $\phi_{\text{PIW},x}$ in the round beam scheme, and the results are presented in Fig. B.5a. All these calculations have been done with $\beta_q^* = 40\,\mathrm{cm}$, and the values for $\phi_{\text{PIW},x} = 0$ are thus the same as in Fig. B.4a for this β_q^*. For nonzero crossing angles, $\mathrm{err}_{N_\mathrm{S}}$ is several $\%$ when only a single slice is applied, which is understandable since $N_\mathrm{S} = 1$ cannot capture the fact that the strong beam is tilted. Therefore, the effective crossing angle is half of what it is supposed to be. The error reduces quicker for larger N_S for nonzero $\phi_{\text{PIW},x}$

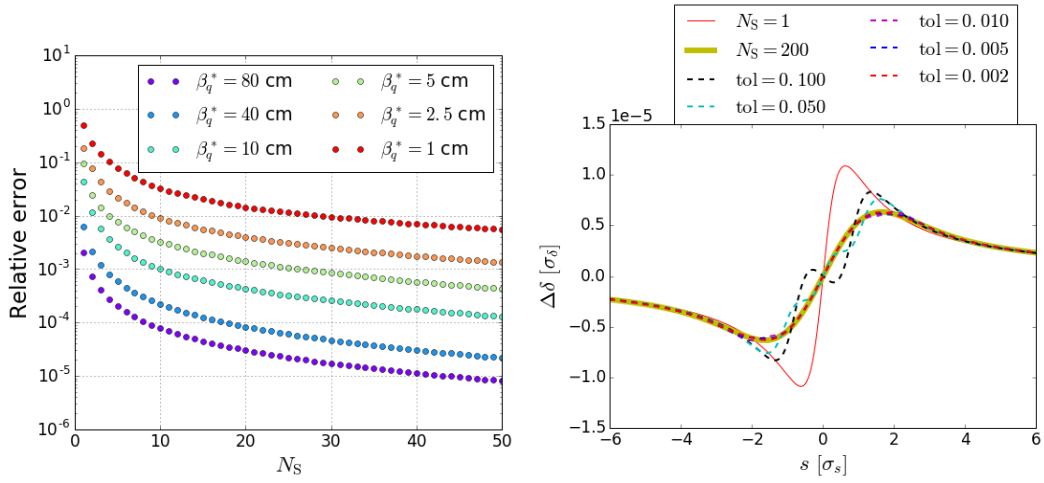

(a) **(b)**

Figure B.4: Dependence on N_S of error in representation of the round beam-beam map. (**a**) displays the dependence of err_{N_S} on different values of β_q^*. (**b**) displays the actual change of δ for different values of N_S, for particles distributed along the s axis, when $\beta_q^* = 2.5\,\mathrm{cm}$ and $\phi_{\mathrm{PIW},x} = 0$. The labelled tolerances (in descending order) correspond to $N_S = \{2, 3, 10, 17, 37\}$.

than for nonzero hourglass effect. Except for at quite large crossing angles and large N_S, the largest error is also for these configurations in the change of δ. However, for nonzero $\phi_{\mathrm{PIW},x}$, this error is of approximately the same order of magnitude as the second largest error. Fig. B.5b shows how Δp_x depends on N_S for particles distributed along the x axis for $\phi_{\mathrm{PIW},x} = 2$, between the limiting cases of $N_S = 1$ and $N_S = 200$. $N_S = 1$ gives transverse kicks for this distribution equivalent to the 4D model. The additional values of N_S has been chosen so that $\mathrm{err}_{N_S} \leq \mathrm{tol}_j$, for different tolerances, tol_j. This plot indicates that already for tolerances of 1%, the effect of the crossing angle is well described, especially compared to when only a single slice is used.

The results presented in this section have shown that the number of slices necessary to achieve a certain tolerance depends strongly on the configuration. For the cases of $(\beta_q^*, \phi_{\mathrm{PIW},x}) = (1\,\mathrm{cm}, 0)$ and $(\beta_q^*, \phi_{\mathrm{PIW},x}) = (40\,\mathrm{cm}, 2)$, applying $N_S = 5$ corresponds to an relative error of 8% and 3% respectively. The error falls of quickly as N_S is increased from 1 to 10, but for larger N_S, the improvement per added slice decreases. Simultaneously, it has been shown that the method describes well the 6D nature of the beam-beam interaction, already for a tolerance of 1%. Finally, I would like to point out that what tolerance to put also depends on what computing resources are available. In CABIN, the tolerance is set to $\mathrm{tol} = 0.2\,\%$ for the simulations presented in this thesis. Calculating what value of N_S is necessary to achieve this tolerance is fast compared to the actual simulation. Thus, CABIN checks this convergence before every simulation, requiring for the round implementation that $\mathrm{err}_{N_S} < 0.2\,\%$ and that $N_S \geq 15$ slices. The configuration with $\beta_q^* = 2.5\,\mathrm{cm}$ will therefore be calculated with $N_S = 48$ slices, while configurations with negligible 6D nature will still be calculated with $N_S = 15$ slices, and hence be modelled more accurately. The flat implementation is slower than the round implementation, as discussed in App. C. The minimum number of slices has thus been reduced to $N_S = 7$ for the flat implementation, still requiring the same tolerance on the error.

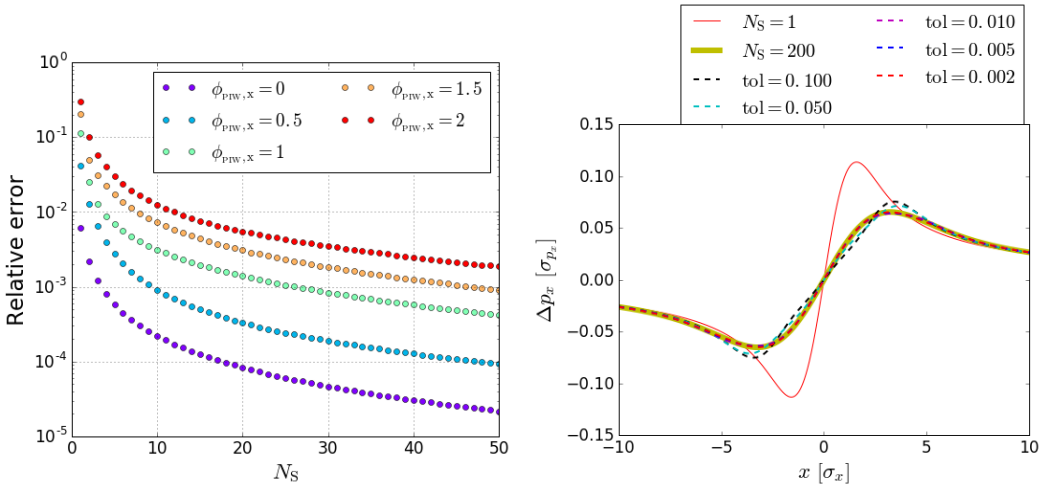

(a) **(b)**

Figure B.5: Dependence on N_S of error in representation of the round beam-beam map. (**a**) displays the dependence of err_{N_S} on different values of $\phi_{\mathrm{PIW},x}$. (**b**) displays the actual change of p_x for different values of N_S, for particles distributed along the x axis, when $\beta_q^* = 40\,\mathrm{cm}$ and $\phi_{\mathrm{PIW},x} = 2$. The labelled tolerances (in descending order) correspond to $N_S = \{3, 4, 13, 22, 48\}$.

Appendix C

SIMULATION TIMINGS

How long time a simulation takes, depends on the ratio between how many calculations have to be made and how many can be made per unit of time. It is not feasible to make a model an exact replication of the physics in synchrotrons. Approximations have to be done, and their validity must be understood. Such approximations reduce the required memory and number of computer operations necessary to complete the simulation. For the timing of a given simulation, the limiting factor is then how many operations that can be performed per second. In this appendix, different options are considered to maximise the efficiency of the implementation of the numerical model.

C.1 From CPU to GPU

The speed of processors increase over time, making it possible today to do what was unthinkable 10 years ago. Given a computer at one point in time, one also has to be able to exploit its abilities to the fullest. While developing CABIN it became clear that a single processor running Python was insufficient. Therefore, a study was initiated to test the speed of different alternatives. The initial alternative was to compare Python and Fortran95. Most of the possible speedup from switching programming language was already achieved using numpy arrays in Python. The second alternative was to implement multiprocessing, using multiple central processing units (CPU) for different parts of the same job. Using M CPUs in parallel gives a theoretical maximum speedup of M on the parallelisable parts of the code, as known from Amdahl's law [51]. The actual speedup is less than M due to additional operations necessary to administer the multiple processes and tasks that cannot be parallelised, which are referred to as overhead in the following. More CPUs still led to a smaller speedup than required.

There is a line of high performance parallel computing that uses graphical processing units (GPU) instead of CPUs. A GPU can perform the same process on multiple threads at the same time. NVIDIA has focused on applying GPUs in scientific programming, using double precision. They have also made a software that can be applied in Python using a wrapper called PyCUDA. The GPU that has been used in this test can run a large number of processes simultaneously, performing calculations on 448 of these processes at a time, at a clock speed which is half of that of the CPUs that have been used. The overhead is however substantial and the speedup of 224 is not achievable. One time-consuming aspect of using a GPU is transfer of memory to and from the GPU. Hence two tests of the GPU were performed. The first test was transferring only a single state of multiple particles onto the GPU, doing tracking on the GPU, and transferring the new state back. This time

is referred to as GPU$_S$, where S stands for small. The second test included the transfer of a memory slot that could contain 2048 values per particle per dimension, necessary for post-processing. This time is referred to as GPU$_L$, where L stands for large. This test has been run on the *liupsgpu* machine at CERN. More hardware information is available in App. D.

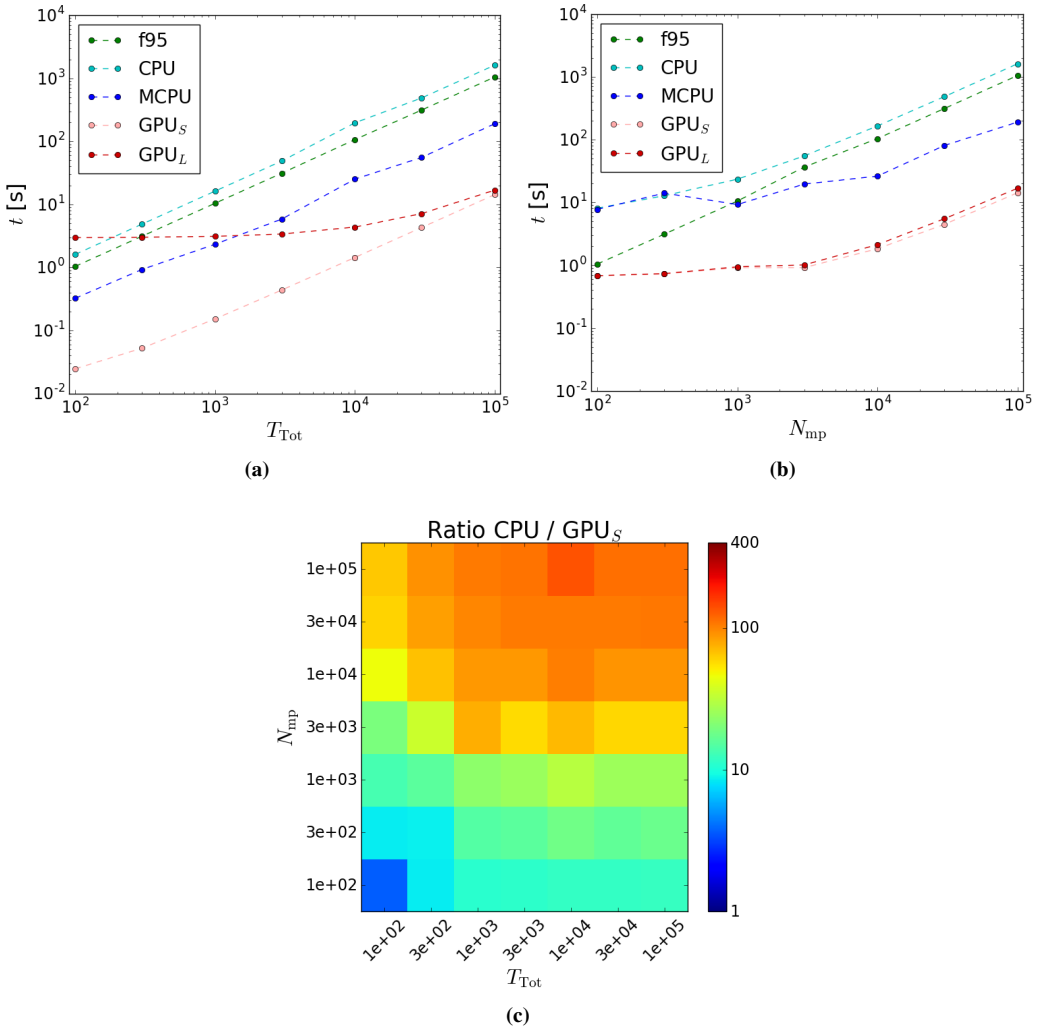

Figure C.1: Results from a computation time study between Fortran95 (f95), Python on 1 CPU (CPU), Python on 10 CPUs (MCPU) and PyCUDA on a GPU with a small (GPU$_S$) and a large (GPU$_L$) memory transfer. (**a**) shows computation time dependence on the total number of turns in the simulation, T_{Tot}, for a given number of macroparticles, $N_{\mathrm{mp}} = 1 \times 10^5$. (**b**) shows computation time dependence on the number of macroparticles, N_{mp}, for a given number of turns, $T_{\mathrm{Tot}} = 1 \times 10^5$. In (**c**) the speedup achieved by the GPU relative to a single CPU is shown for multiple combinations of macroparticles and turns.

All methods were tested on how fast they could track a given number of macroparticles N_{mp}, over a given number of turns T_{Tot}. Each turn the particles were transferred through a linear lattice and affected by two 4D HO beam-beam interactions between round beams in the weak-strong

model. The results from the computation time study are presented in Fig. C.1. Summarised, the GPU used from Python was faster than using $M = 10$ CPUs running Python, which was faster than a single CPU running Fortran95 (f95), which was faster than a single CPU running Python. With the optimal conditions of a large N_{mp} and a large T_{Tot}, the tested GPU gave a speedup of approximately 137 compared to a single CPU, not too far from the theoretical speedup of 224. The speedup of using either a GPU or M CPUs was eradicated for a smaller number of macroparticles, when the speedup of multiprocessing was less than the additional time spent on overhead. Also, the large transfer to and from the GPU dominated the computation time for a lower number of turns.

C.2 Profiling of Beam-Beam Implementations

Both round and flat beams in 4D and 6D has been implemented in CABIN. Therefore, it is of interest to compare the speed of simulations using the different beam-beam implementations. The round beam implementations are readily compared, as they mostly depend on the exponential function whose timing is rather input independent. The main difference between the round and the flat beam implementations is that the flat beam kick is calculated by use of both the exponential and the Faddeeva function. The Faddeeva function is much slower. The flat beam implementations depend strongly on the configuration and the distribution of the particles. When the normalised transverse displacement from the centre of the slice is larger than 10, $\sqrt{\hat{x}^2 + \hat{y}^2} \geq 10$, the Faddeeva function is only calculated once and not twice per particle per interaction. Further time savings occurs in the calculation of the Faddeeva function itself when the absolute value of either the real or the imaginary input to the Faddeeva function is larger than 5.33 or 4.29 respectively. This happens more often when the denominator $\sqrt{\sigma_x^2 - \sigma_y^2}$ is small, i.e. when the flat beam is almost round. The GPU that has been used for the following tests is Nvidia® Tesla™ C2075.

A comparison between computation time of only the beam-beam interaction per particle per interaction, t_{pppi}, is presented in Tab. C.1. The values presented are averages of three iterations of tracking a total of $N_{\text{mp}} = 65536$ particles for $T_{\text{Tot}} = 2 \times 10^4$ turns. The particles have been initially distributed in a 2D-grid in $(\hat{x}, \hat{y})$ space, where each coordinate is distributed uniformly on the interval $\hat{x} \in (10^{-8}, 10]$. In these simulations $\beta_y^* = 0.4\,\text{m}$ and $\phi_{\text{PIW},x} = 0.01$. The time spending for the 6D model has been separated in the time spent per slice, and the 6D overhead, which includes the transformation from normalised to non-normalised coordinates and the required Lorentz boost due to the crossing angle. The separation has been done by measuring the timing for different numbers of slices, $N_{\text{S}} \in \{3, 5, 11, 21\}$, and performing a linear regression. In general, the calculation time for the 4D model is similar but smaller than the time spent on each slice in the 6D model. This is expected as a few more operations are done per slice in the 6D model than in the 4D model, but in general these are not the most time consuming calculations. The 6D overhead calculations are the same for the round and the flat implementation, and these have been found to be similar in the two different configurations. The difference should largely be caused by deviation in the time measurements. The calculation time for flat beams does not change much for a larger β_x^*/β_y^*, but it does begin to reduce as this ratio becomes smaller. For round bunches, the 6D overhead takes as much time as 6 slices, i.e. using 18 slices is only twice as slow as using 6 slices, although the accuracy is much greater. The same is not true for flat bunches, for which the overhead timing is shorter than the timing of a single slice.

A comparison between timings of complete beam quality simulations, t_{sim}, is presented in Tab. C.2. In these simulations, $N_{\text{mp}} = 1 \times 10^5$ macroparticles are distributed uniformly below a 6D radius of 6σ, and tracked for $T_{\text{Tot}} = 2 \times 10^6$ turns. The simulations include all relevant effects implemented in CABIN; 2 IPs per turn of alternate crossings with $\phi_{\text{PIW}} = 0.01$, separated by 2 independent linear phase advances affected by chromaticity making up the entire lattice, a source of

Table C.1: Computation time per particle per beam-beam interaction, t_{pppi}. Comparison between 4D and 6D model, and between the transfer map from a round and a flat beam. The timing for the 6D model has been separated in time per slice and the additional 6D overhead.

t_{pppi}	Round	Flat $\beta_x^* = 1.01 \cdot \beta_y^*$
4D	0.70 ns	28.8 ns
6D overhead	5.45 ns	5.7 ns
6D per slice	0.88 ns	29.1 ns

Gaussian white noise, and collimation of particles at large amplitudes. These timings express well the necessity of knowing when what approximation is valid. Using the 4D model instead of the 6D saves approximately a factor 10 for $N_{\mathrm{S}} = 15$, while being able to use round beams instead of flat beams saves approximately a factor 70 in time, for this particular distribution and configuration. The beam quality simulations runs approximately a factor 8 times faster on the Tesla P100 GPU, which is presented in App. D.

Table C.2: Runtime of complete beam quality simulation with 2 IPs per turn of alternate crossings, 2 independent contributions of phase advance from the lattice including a nonzero chromaticity, and noise. $N_{\mathrm{mp}} = 1 \times 10^5$, $T_{\mathrm{Tot}} = 2 \times 10^6$, $\phi_{\mathrm{PIW}} = 0.01$, $Q' = 2$, noise of $\Delta = 1 \times 10^{-4}$.

t_{sim}	Round	Flat $\beta_x^* = 1.01 \cdot \beta_y^*$
4D	9.8 min	10.8 h
6D ($N_{\mathrm{S}} = 15$)	118 min	94 h

The simulation timings, t_{sim}, should be comparable to the timing expected from the beam-beam interaction alone, $t_{\mathrm{bb}} = 2 \cdot N_{\mathrm{mp}} \cdot T_{\mathrm{Tot}} \cdot t_{\mathrm{pppi}}$. The values for t_{bb} are presented in Tab. C.3. For round 4D beams, $t_{\mathrm{bb}} = 4.7\,\mathrm{min}$, approximately $5\,\mathrm{min}$ less than the timing of the full simulation. This is largely because more effects are included in these simulations than the beam-beam interaction alone, and there is a substantial overhead necessary for organising the simulations, including the memory transfers to and from the GPU. However, both these explanations should be similar for all simulations. The time spending from other sources than the beam-beam interaction is only substantial for the simplest implementation, the round 4D beam-beam interaction. For round 6D beams, t_{bb} is 6% larger than t_{sim}. The discrepancy is likely caused by inaccuracies in the measurements of t_{pppi}, in addition to the small overhead of simulations of approximately $5\,\mathrm{min}$. For flat 4D beams, $t_{\mathrm{bb}} = 3.4 \cdot t_{\mathrm{sim}}$, and for flat 6D beams, $t_{\mathrm{bb}} = 1.9 \cdot t_{\mathrm{sim}}$. These discrepancies are much larger than for round beams. Parts of this discrepancy may be explained by the different simplifications that can be done for the flat beam implementation while simulating. In fact, when the particles are initially distributed in a 2D grid in $(\hat{x}, \hat{y})$ up to a maximum normalised value of 10, the actual simulation time for flat 4D beams is substantially reduced to $t_{\mathrm{sim}} = 2.2\,\mathrm{h} < t_{\mathrm{bb}}$.

In this section, it has been shown that the 6D implementation is more time consuming than the 4D implementation, and that the flat beam implementation is more time consuming than the round beam implementation. It has also been shown that the timing of the flat beam model depends strongly on the distribution, being much slower for particles in the core than for particles in the tails. The previous section compared simulation times when the beam-beam interaction was ap-

Table C.3: Expected timing from beam-beam interaction only, based on t_{pppi} in Tab. C.1, $t_{\mathrm{bb}} = 2 \cdot N_{\mathrm{mp}} \cdot T_{\mathrm{Tot}} \cdot t_{\mathrm{pppi}}$. 2 IPs per turn, $N_{\mathrm{mp}} = 1 \times 10^5$, $T_{\mathrm{Tot}} = 2 \times 10^6$, $\phi_{\mathrm{PIW}} = 0.01$.

t_{bb}	Round	Flat $\beta_x^* = 1.01 \cdot \beta_y^*$
4D	4.7 min	3.2 h
6D ($N_{\mathrm{S}} = 15$)	125 min	49 h

proximated by the round 4D weak-strong model. Hence, the limits on T_{Tot} and N_{mp} for when the speedup of multiprocessing is positive, either by M CPUs or by a GPU, would be lower for the slower configurations including either the 6D map or the flat beam model or both.

Appendix D

COMPUTING RESOURCES

The various computing resources that has been used during the work on this thesis are listed in Tab. D.1. All 4 computers are running some form of Linux. Computer 1 is a standard office desktop from which all work has been done. It does not have a GPU, but has been applied to analyse data and connect to the GPU resources. Computer 2 is a machine that was built for the LHC injectors upgrade project for the Proton Synchrotron (*liups*). It contains more CPU cores than computer 1, and 4 GPUs from 2011. This has been used for all the testing of the GPU-codes, and also quite substantial simulations during the entire project. It is shared by multiple users in the CERN-community, and the availability has been unpredictable.

Towards the end of this project it became clear that the GPU hardware available in computer 2 was insufficient. NTNU provided access to computer 3, the *Idun*-cluster, serviced by their high-performance computing group. Computer 4 is one of the queues on this cluster, containing 9 nodes that each carry 2 Tesla P100 for PCIe-based servers. Getting access to these resources was an upgrade for the master's project, gaining approximately 42 times higher total double precision performance.

Table D.1: Computing resources that have been applied during the master's project.

	Standard desktop	*liupspgu*	*Idun*	*epic*
Computer number	1	2	3	4
OS	Ubuntu 16.04.1 LTS	Ubuntu 14.04.5 LTS	Centos 7	Centos 7
CPU	Intel Core	Intel Xeon	Intel Xeon	Intel Xeon
	i7-6700	E5-2630	E5-2630 v4	E5-2660
CPU cores	8	24	20	40
CPU clock rate	3.40 GHz	2.30 GHz	2.20 GHz	2.60 GHz
CPU L3 cache	8 MB	15 MB	25 MB	25 MB
RAM	8 GB	252 GB	62 GB	252 GB
GPU		Tesla C2075 [52]		Tesla P100 PCIe [53]
CUDA cores		448		3584
RAM		6 GB		16 GB
GPU core clock rate		1.15 GHz		-
Peak FP64 performance		0.515 TFLOPS		4.7 TFLOPS
Memory bandwith		144 GB s^{-1}		732 GB s^{-1}
Number of GPUs		4		9×2

Appendix E

BEAM PARAMETERS IN LHC EXPERIMENT

A dedicated experiment was performed in the LHC to study the limitations due to strong head-on beam-beam interactions, with no impact of long-range interactions [48, 49]. The working point was shifted around in tune space, (Q_x, Q_y), during the experiment. The necessary values to reproduce the behaviour for each working point are given in Tab. E.1, including the emittance in both planes for both bunches, the intensity of the strong bunch and the measured loss rate per hour of the weak bunch. The intensity and emittances given are the averages over the length of the interaction at that working point. The weak bunch is equivalent to bunch 2100 in beam 1, while the strong bunch is equivalent to bunch 2100 in beam 2.

Table E.1: Emittance and intensity measured in the LHC for two bunches colliding with strong beam-beam interactions. The subscripts 1 and 2 correspond to the weak and strong bunch respectively.

(Q_{x1}, Q_{y1})	$\epsilon_{n,x1}$ [µm]	$\epsilon_{n,y1}$ [µm]	$\epsilon_{n,x2}$ [µm]	$\epsilon_{n,y2}$ [µm]	N_2 $[10^{11}]$	$LR_{\mathrm{LHC},1}$ $[\mathrm{h}^{-1}]$
$(0.311, 0.318)$	1.875	2.533	1.884	1.395	1.724	0.064
$(0.310, 0.317)$	1.921	2.574	1.864	1.378	1.720	0.075
$(0.309, 0.316)$	1.873	2.597	1.856	1.377	1.714	0.089
$(0.308, 0.315)$	1.887	2.574	1.843	1.384	1.708	0.087
$(0.307, 0.314)$	1.908	2.528	1.867	1.384	1.693	0.062
$(0.306, 0.313)$	1.922	2.461	1.892	1.369	1.692	0.075
$(0.305, 0.312)$	1.924	2.491	1.870	1.375	1.690	0.066
$(0.304, 0.311)$	1.926	2.498	1.878	1.389	1.688	0.074
$(0.303, 0.310)$	2.029	2.525	1.889	1.378	1.654	0.073
$(0.302, 0.309)$	1.970	2.501	1.859	1.364	1.612	0.151
$(0.301, 0.308)$	1.850	2.437	1.875	1.368	1.606	0.387
$(0.301, 0.308)$	1.833	2.440	1.844	1.360	1.582	0.128
$(0.300, 0.307)$	1.795	2.410	1.765	1.337	1.562	0.101
$(0.299, 0.306)$	1.794	2.416	1.810	1.340	1.557	0.124
$(0.298, 0.305)$	1.775	2.392	1.784	1.326	1.552	0.156
$(0.311, 0.319)$	1.628	2.156	1.650	1.224	1.917	0.079
$(0.311, 0.320)$	1.672	2.129	1.622	1.214	1.915	0.061
$(0.311, 0.321)$	1.702	2.199	1.612	1.245	1.914	0.079
$(0.311, 0.322)$	1.662	2.159	1.646	1.234	1.913	0.066
$(0.311, 0.323)$	1.686	2.172	1.632	1.230	1.909	0.066
$(0.312, 0.323)$	1.669	2.182	1.644	1.236	1.905	0.067
$(0.313, 0.323)$	1.713	2.177	1.662	1.240	1.897	0.050
$(0.314, 0.323)$	1.754	2.296	1.661	1.242	1.896	0.058
$(0.315, 0.323)$	1.706	2.211	1.680	1.244	1.894	0.054
$(0.315, 0.324)$	1.687	2.101	1.679	1.243	1.892	0.050
$(0.315, 0.325)$	1.707	2.162	1.684	1.245	1.889	0.071
$(0.315, 0.326)$	1.661	2.175	1.688	1.236	1.886	0.062
$(0.315, 0.327)$	1.669	2.266	1.709	1.242	1.885	0.080
$(0.316, 0.327)$	1.660	2.274	1.724	1.237	1.882	0.063
$(0.317, 0.327)$	1.700	2.288	1.730	1.240	1.880	0.066
$(0.317, 0.328)$	1.726	2.180	1.734	1.237	1.878	0.108
$(0.318, 0.328)$	1.671	2.125	1.739	1.237	1.877	0.081
$(0.319, 0.328)$	1.682	2.198	1.726	1.234	1.876	0.065